UNIVERSITY OF SOUTHAMPTON

FACULTY OF NATURAL AND ENVIRONMENTAL SCIENCES

SCHOOL OF OCEAN AND EARTH SCIENCE

Volume [1] of [1]

FROUDE SUPERCRITICAL GEOPHYSICAL FLOWS: THEIR RELATED BEDFORMS AND FRONTAL STRUCTURE

by

Age Jan Vellinga

Thesis for the degree of Doctor of Philosophy

July 2018

UNIVERSITY OF SOUTHAMPTON

ABSTRACT

FACULTY OF NATURAL AND ENVIORNMENTAL SCIENCES

SCHOOL OF OCEAN AND EARTH SCIENCE

Thesis for the degree of Doctor of Philosophy

FROUDE SUPERCRITICAL GEOPHYSICAL FLOWS: THEIR RELATED BEDFORMS AND FRONTAL STRUCTURE

Age Jan Vellinga

Sediment transport around the globe is dominated by rivers and turbidity currents. While rivers shape the land, turbidity currents shape the ocean floor. These flows can pose hazards to infrastructure placed in their paths. The sedimentary deposits left behind by these flows are key to understanding how our planet evolved over geological timescales. This thesis aims to enhance the general understanding of these geophysical flows by tackling specific areas of flow dynamics and their deposits that have so far remained poorly understood.

Rivers transport most of their sediment in rare flooding events. A specific type of bedform can occur during these floods, called cyclic steps. Little is known about these cyclic steps as their occurrence is rare and observations during such powerful floods are difficult to make. Here, cyclic steps are reproduced in a numerical model to constrain bedform morphyodynamics. Additionally, the model is used to predict how the occurrence of cyclic steps can be deduced from studying the deposits that are left behind by floods. The numerical modelling shows that the relation between flow properties and the occurrence of erosion deviate from existing models. The deposits arising from cyclic steps depend on how fast sediment is deposited. Cyclic steps that deposit rapidly form a series of upstream-dipping laminations bound by erosion surfaces. Cyclic steps that deposit slowly, however, form amalgamated concave-up erosion surfaces that are infilled with laminations that dip upstream and downstream. These results now allow geologist to reconstruct river floods throughout geological time with more confidence.

In contrast to rivers, where cyclic steps are rare, similar bedforms are abundant in submarine channels, which are major conduits of sediment transport to the deep ocean. These bedforms are an important building block for submarine channels; just as dunes are for rivers. Unlike rivers, the formative controls on these bedforms in submarine channels are presently not well understood. Here I tested three hypotheses on the formation of the bedforms, again using a numerical model. (1) These bedforms only form under fast and thin flow, (2) the bedforms only form under stratified flow and (3) the bedforms only form under flows strong enough to erode sediment from the seafloor. The results of the study showed that (1) not all fast and thin flows create the bedforms, (2) only stratified flows, but not all, create the bedforms and (3) only flows that exceed a threshold of erosion created the bedforms. These results show that the bedforms form in submarine channels that fall within a "sweet spot" of particular grain-size and slope, and thus explains their abundance, but also their local absence.

Finally, this thesis presents some direct observations of turbidity currents on the seafloor. These observations confirm the importance of stratification already noticed in the previous numerical modelling work. The observations show that the fronts of stratified turbidity currents are wedge-shaped, and host the fastest and densest part of the flow. These observations contrast the bulbous and dilute front found in unstratified turbidity currents seen in most modelling studies. The frontal structure of stratified turbidity currents shows remarkable similarities to that of stratified pyroclastic density currents and powder-snow avalanches. A fast and dense front on turbidity currents poses substantially larger hazards for any submarine infrastructure such as pipelines and telecommunication cables.

Table of Contents

Table of Tables

Table of Figures

Chapter 1

Chapter 2

Chapter 3

Chapter 4

Accompanying Material

- USB flash-drive with:
    - PDF version of this thesis
    - Supplementary video material
        - Video 2.1: A video of the simulated cyclic steps from chapter 2. The colours represent the velocity magnitude of the water.
        - Video 2.2: A video of the internal architecture and dynamics of the cyclic steps simulated in chapter 2.
        - Video 3.1: A video of one of a simulated turbidity current from chapter 3 that did not make any bedforms.
        - Video 3.2: A zoomed-in video of one of a simulated turbidity current from chapter 3 that did not make any bedforms.
        - Video 3.3: A video of one of a simulated turbidity current from chapter 3 that made upstream-migrating bedforms.
        - Video 3.4: A zoomed-in video of one of a simulated turbidity current from chapter 3 that made upstream-migrating bedforms.
        - Video 4.1: A M3 video of a turbidity current observed in the Scheldt estuary, as described in chapter 4.

Academic Thesis: Declaration of Authorship

I, Age Jan Vellinga

Declare that this thesis and the work presented in it are my own and has been generated by me as the result of my own original research.

FROUDE SUPERCRITICAL GEOPHYSICAL FLOWS: THEIR RELATED BEDFORMS AND FRONTAL STRUCTURE

I confirm that:

1. This work was done wholly or mainly while in candidature for a research degree at this University;
2. Where any part of this thesis has previously been submitted for a degree or any other qualification at this University or any other institution, this has been clearly stated;
3. Where I have consulted the published work of others, this is always clearly attributed;
4. Where I have quoted from the work of others, the source is always given. With the exception of such quotations, this thesis is entirely my own work;
5. I have acknowledged all main sources of help;
6. Where the thesis is based on work done by myself jointly with others, I have made clear exactly what was done by others and what I have contributed myself;
7. Parts of this work have been published as: *Morphodynamics and depositional signature of low-aggradation cyclic steps: New insights from a depth-resolved numerical model* in the Journal *Sedimentology*
8.

Signed: .....

Date: .....

Acknowledgements

My thesis is an individual piece of work, however, I could not have done it alone.

Firstly, I would like to acknowledge the University of Southampton and ExxonMobil for making for funding my Ph.D. studies.

A big thank you is in place for my supervisory team for their help: Matthieu Cartigny, Mike Clare, Esther Sumner and Pete Talling. You have helped me a lot, and I had fun too. Matthieu and Mike deserve a special thank you, they supported and inspired me, taught me how to science, and helped grow as a person too. Thank you!

A thanks too to all other colleagues and co-authors. Joris Eggenhuisen and Ernst Hansen may not have been my official Ph.D.-supervisors, but have been of special importance to my career, thank you. I would like to thank all my friends in Southampton. I had a great time in Southampton because of you, and without the fun we have had, I would not have gotten this far. Gavin, Jamie, I could not have wished for better office mates. My friends in the Netherlands: though I may not have been there much, thank you for your friendship.

Amaya, mi guapissima. Thanks for your love and support.

Lastly, my family, and especially my parents, have supported me while making this work, and the many years leading up to it. Dankjewel.

Chapter 1: Introduction

Geophysical flows such as rivers, pyroclastic density currents, avalanches, turbidity currents, glaciers, and winds shape the Earth's surface. They generate morphological features that can range from centimetre-scale ripples to deep canyons that extend for hundreds of kilometres into the deep-sea. The two types of geophysical flows that feature in this work are rivers and turbidity currents.

1.1 Why study rivers and turbidity currents?

Rivers and turbidity currents are the two most important mechanisms to transport sediment around the globe (Talling et al., 2012). Rivers create morphological features as valleys, meanders, and bedforms (Fig. 1). Turbidity currents are subaqueous flows of sediment suspended in water that transport sediment from continental shelves to the deep ocean. Water with suspended sediment is denser than the ambient water, hence turbidity currents move downslope. Just as rivers shape the surface on land, turbidity currents sculpt the seascape on a range of scales, forming submarine canyons, meanders, and bedforms (Fig. 1) (Heezen et al., 1964; Damuth et al., 1983; Symons et al., 2016). Both rivers and turbidity currents thus shape the Earth's surface.

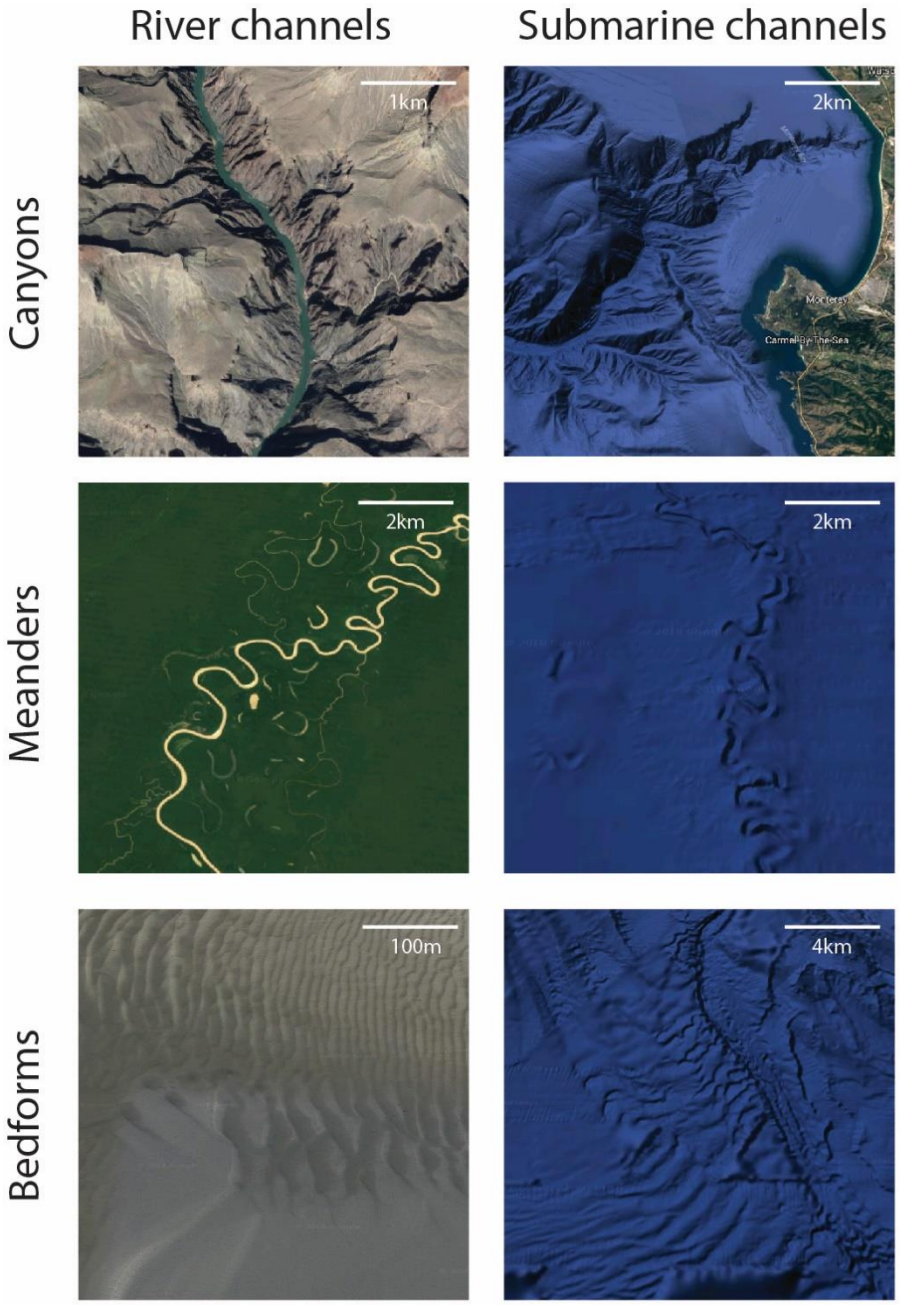

Figure 1: morphological comparison between river channels and submarine channels based on open-source images from Google Earth. Rivers: Grand Canyon, Arizona, USA (top), Purus River meanders, Brazil (middle), bedform in the Scheldt, the Netherlands. Submarine channels: Monterey submarine canyon (top), Amazon submarine fan meanders (middle), bedforms in the South China Sea (bottom).

The morphological behaviour of rivers has been of societal importance since the early days of civilisation. The effects of flooding and river avulsions have played a role in the evolution of early civilisations, such as in Mesopotamia and ancient Egypt, where avulsion areas and channel-belts provided fertile soil for agriculture (Hassan, 1997; Morozova, 2005). Nowadays river morphology not only influences agriculture but also navigation, industrial use and recreation, while understanding

river morphodynamics is key to flood management (Brierley and Fryirs, 2013). Thus, it is important to understand the processes that shape river morphology, and how to reconstruct these processes from the deposits that these rivers leave behind in the sedimentological record. Their deposits are often used as indicators of past climate, floods, and overall paleo environment; hence understanding the link between process and deposit is important.

The impact of subsea sediment movements by turbidity currents has only become obvious in modern times. On 18 November 1929, an earthquake triggered a large submarine landslide off the coast of Newfoundland (Nisbet and Piper, 1998). As the landslide mass mixed with the ambient seawater, it triggered a turbidity current that cut transatlantic telegraph cables between America and Europe (Heezen and Ewing, 1952). Subsea infrastructure has become more extensively laid and is of greater importance to society now. More than 95% of global telecommunications are now carried by subsea cables (Carter et al., 2009), and offshore energy production facilities and transport (both fossil and sustainable), are increasingly important (e.g. Barley, 1999; Pettingill and Weimer, 2002). As telecommunications and energy are both fundamental parts of our modern life, the hazard turbidity currents pose to critical subsea infrastructure is important to understand. Furthermore, the deposits associated with turbidity currents, turbidites, are amongst the largest sedimentary accumulations on Earth (Bouma, 1962), and form many of the important hydrocarbon reservoirs worldwide (Stow and Johansson, 2000). Robust characterisation of these deposits helps understanding paleo-environments and predicting reservoir location and quality.

1.2 Linking bedforms and deposits to flow processes

Bedforms are instabilities at the interface between an erodible bed and an overlying flow. Metre-scale bedforms are the building blocks of deposits associated with rivers and submarine channels (Best, 2005; Covault et al., 2016). While individual bedforms can form over a timescale of minutes and length scales metres, their accumulated deposits (which may span the entire length of a channel) can potentially provide long-term archives of flow behaviour over hundreds of kilometres and millions of years (Best, 2005; Parsons and Best, 2013).

A sedimentary deposit is often all that is left of a sedimentary process that occurred over the geological past. Hence interpretations of these processes are

depending on linking the deposit to their flow dynamics that formed them. However, our interpretation relies on understanding of the process forming those deposits.

> *"If the present is the key to the past, it is a key no better than our understanding of present geologic processes." (Harms and Fahnstock, 1960)*

There are four approaches to study sedimentary processes (Fig. 2): (1) direct observation, (2) use of conceptual models based on existing knowledge, (3) scaled-down laboratory experiments and (4) numerical modelling. Direct observations are preferable, though not all sedimentary processes are easily observed or measurable. Some geophysical flows occur at locations which are difficult to measure, or are destructive, such as deep-sea turbidity currents (e.g. Khripounoff et al., 2012; Lintern et al., 2016). To date, detailed and direct measurement of turbidity currents are only known from seven sites worldwide (Azpiroz et al., 2017). Although this number is slowly growing with the uptake of new technology, it pales in comparison to the millions of equivalent measurements available for rivers (Milliman and Syvitski, 1992). Thus, conceptual models (often based on deposits), scaled-down laboratory experiments and numerical models are valuable methods to fill the gaps in process understanding and help us determine whether findings from other geophysical flows are transferable to turbidity currents. In this thesis I consider aspects from each of these approaches to better understand the links between flows and deposits. First, new conceptual models of specific aspects of rivers and turbidity currents are constructed and compared to existing ones. Second, a three-dimensional numerical model is used to simulate both river flow and turbidity currents to quantify the link between flow properties and resultant deposits.

Third, modelling outputs are compared to laboratory-scale experiments to investigate their validity. Finally, analysis of new direct measurements turbidity current provides new insights into how these flows behave at field-scale.

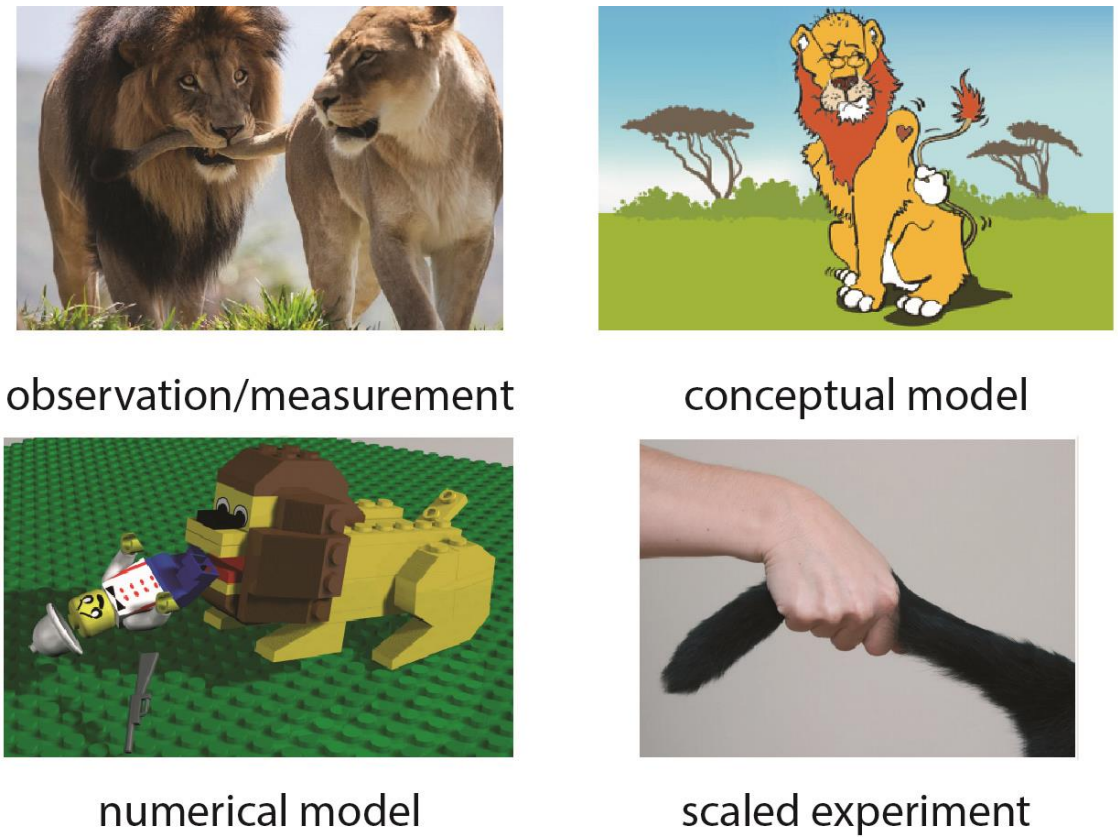

Figure 2: Four methods to interrogate reality when a lion's tail is twisted modified after Kleinhans et al., (2010). Firstly, top left, the direct measurements and observations of a lion's tail being twisted. Second, top right, the conceptual model, biased through the observers own frame of reference, note the human features of the lion. Third, bottom left, numerical modelling based on established laws, limited by the choices of laws, parameters and boundary conditions. Fourth, bottom right, twisting the tail of a scaled-down Lion, which may lead to scale problems.

1.3 Aim of this thesis

The overall aim of this thesis is characterising geophysical flows that create upstream-migrating bedforms. There are various kinds of upstream-migrating bedforms in many different type of flows; those created by rivers (e.g. Middleton, 1965; Nordin and Beverage, 1965), turbidity currents (e.g. Kostic et al., 2010; Paull et al., 2010; Symons et al., 2016), pyroclastic density currents (e.g. Cole, 1991; Moorhouse and White, 2016) and even by polar adiabatic winds on planet

Mars (Smith et al., 2013)! In contrast to the abundance of these bedforms over such a wide variety of settings, very little is known on the dynamics of these bedforms.

Upstream-migrating bedforms can be divided into symmetrical bedforms called antidunes and asymmetrical bedforms called cyclic steps (Cartigny et al., 2014). Most previous studies have focussed on the dynamics of antidunes in rivers (Kennedy, 1969; Alexander et al., 2001; Froude et al., 2017). The aim of chapter 2 is to determine the morphodynamics and depositional signature of cyclic steps in a fluvial setting.

Turbidity currents can also create upstream-migrating bedforms both within and outside submarine channels (e.g. Paull et al., 2010; Symons et al., 2016). Turbidity currents are difficult to observe directly and thus the formative controls on upstream migrating bedforms are more poorly understood than those in a fluvial setting. Chapter 3 aims to quantify the formative controls on dune-scale upstream-migrating bedforms created by turbidity currents in submarine channels.

Powder-snow avalanches and pyroclastic density currents are particulate gravity currents (their driving force being the particle suspended in the fluid) just as turbidity currents are. Powder-snow avalanches and pyroclastic density currents are in many ways similar to turbidity currents and field studies have shown these currents too display upstream-migrating bedforms of snow and ash (Cole, 1991; Moorhouse and White, 2016). Chapter 4 of this thesis aims to characterise the frontal structure of a turbidity current that created upstream-migrating bedforms, using new direct measurements, and compare the character to that of Powder-snow avalanches and pyroclastic density currents.

A more detailed introduction of the relevance of these research chapters is provided in the next section (1.4). The results are summarised and suggestions for future work are presented in Chapter 5.

1.4 Introduction of individual research topics

1.4.1 What is the morphodynamic and depositional signature of cyclic steps?

High-discharge events such as floods or glacial outwashes transport a significant portion of sediment in rivers (Nordin and Beverage, 1965). Most morphodynamic change occurs during these individual flow events, rather than during normal flow conditions (Kochel, 1988). These high-discharge events are prone to Froude-supercritical flow (e.g. Fielding, 2006; Lang and Winsemann, 2013). A flow is Froude-supercritical if surface waves are unable to propagate upstream, and inertial forces dominate over gravitational forces. The Froude number (*Fr*) (Reech, 1852; Froude, 1872) (Eqn. 1.1) describes the ratio of inertial to gravitational forces, where inertial force is represented by the flow velocity (*u*), and gravitational force represented by the product of the flow thickness (*h*) and the acceleration due to gravity (*g*). *Fr<1* means the flow is in the *subcritical* regime, and *Fr>1* means flow is in the *supercritical* regime.

$$Fr = \frac{u}{\sqrt{gh}} \qquad (1.1)$$

Several types of bedforms (antidunes, transitional bedforms and cyclic steps) may form under supercritical flows in open channels (e.g. Kennedy, 1969; Parker, 1996; Alexander, 2008; Cartigny et al., 2014). *Cyclic steps* form at the highest Froude numbers (Cartigny et al., 2014). Supercritical flow occurs on the steeper lee-side of cyclic steps, while subcritical flow occurs on the lower angle stoss side. The transition from supercritical to subcritical flow at the trough of the bedform is marked by a hydraulic jump (Fig. 3) (Parker, 1996). As a result of these contrasting flow regimes, the lee-side of the bedform is erosional, and the stoss-side is depositional, causing the bedform to migrate upstream. Overall sediment transport is, however, still directed downstream.

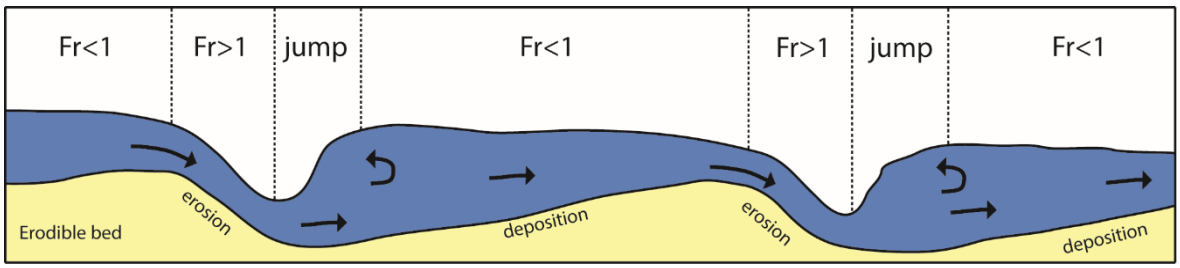

Figure 3: A schematic drawing of a cyclic step system. The stoss-side of the cyclic step is associated with a subcritical (Fr<1) and depositional flow. The lee-side of

cyclic step bedform is characterized by supercritical (Fr>1) and erosive flow. The transition between supercritical and subcritical flow is marked by a hydraulic jump.

Deposits related to cyclic steps are seldom observed. This could be because these deposits are often not preserved, or simply because their depositional signature is not well understood. Linking the morphodynamics of cyclic steps to the resulting sedimentary structure is thus crucial in being able to accurately interpret the deposit.

The research questions in this chapter are: *(1) how do cyclic steps work?* And *(2) what depositional signature is associated with cyclic steps?* Physical parameters, such as depth-varying sediment concentration, velocity and turbulence are difficult to quantify using laboratory models or using depth-averaging numerical models. These parameters are, however, crucial to linking flow dynamics to the sedimentary architecture and facies variation over time and space. Moreover, interpreting supercritical-flow processes from outcrops and cores is strongly dependent on distinguishing small scale facies characteristics. For these reasons a depth-resolved numerical model is employed to answer these two research questions.

1.4.2 What are the formative controls on dune-scale upstream-migrating bedforms in submarine channels?

Dune-scale upstream-migrating bedforms are abundant, yet not ubiquitous, in submarine channels (Symons et al., 2016). For example, in Monterey Canyon (offshore California) these bedforms are present at most, but not all locations (Paull et al., 2011). Dune-scale bedforms are well-studied and play an important role transporting sediment in rivers (Best, 2005). In contrast, the formative controls on dune-scale upstream-migrating bedforms in submarine channels are debated (Paull et al., 2010), though they may be of similar importance for sediment transport in submarine channels (Covault et al., 2017). A poor constraint on when and where these bedforms form also hinders confident interpretations of their associated deposits.

Turbidity currents are more prone to supercritical flow than rivers. As the density contrast between a turbidity current and the ambient water is small, which implies that the gravitational forces in the flow are often small relative to the inertial forces. The densimetric Froude number (Fr_d) (Komar, 1971) (Eqn. 1.2), is

used to compute Froude numbers in density currents, where ρ_{f1} and ρ_{f2} relate to the density of the ambient fluid and density current.

$$Fr_d = \frac{u}{\sqrt{\frac{\rho_{f2}-\rho_{f1}}{\rho_{f2}}gh}} \quad (1.2)$$

Three factors are suggested to play a role in the formation of dune-scale upstream-migrating bedforms by turbidity currents: Froude supercriticality (Hughes Clarke, 2016; Covault et al., 2017),density stratification (Postma and Cartigny, 2014; Hughes Clarke, 2016) and erosive capacity (Parker, 1996; Balmforth and Vakil, 2012). The importance of the three suggested formative controls is however unknown, as direct measurements of turbidity currents are sparse.

The research question in this chapter is: *What are the formative controls on upstream-migrating bedforms in submarine channels?* The question is answered by employing a depth-resolved numerical model (as in chapter 2). A numerical model is used as available direct measurement data cannot answer this question, and numerical model allows testing of several boundary conditions. The model is depth-resolved because flow stratification needs to be simulated.

1.4.3 What is the frontal structure of stratified turbidity currents compared to other particle-laden density currents?

Direct measurements of turbidity currents are sparse (Xu, 2011; Talling et al., 2015). These sparse measurements suggest that the front of turbidity currents is the most hazardous to subsea infrastructure as they host the highest velocities and densities (Symons et al., 2017). Quantification of hazard impact relies on appreciating the structure of a turbidity current (Bruschi et al., 2006a; Clare et al., 2015a); hence it is particularly important to understand to frontal character of turbidity currents.

Turbidity currents, powder-snow avalanches and pyroclastic density currents are all geophysical particulate density currents. Powder-snow avalanches and pyroclastic density currents are known to display two endmember flow modes: (1) well-mixed and fully turbulent flows and (2) stratified flows (Voellmy, 1955a; Simpson, 1982; Branney and Kokelaar, 2002). These two different flow modes are expressed in the frontal character of these flow, where dilute flows have a bulbous and dilute front, and stratified flows have a dense and thin front (e.g.

Sovilla et al., 2015; Breard et al., 2016). It is unclear whether turbidity currents exhibit these same two flow modes, as previous direct measurements (Xu et al., 2004; Khripounoff et al., 2012; Xu et al., 2012; Puig et al., 2014; Hughes Clarke, 2016; Azpiroz-Zabala et al., 2017; Symons et al., 2017) have struggled to make detailed measurements of the flow front and close to seafloor.

The research questions in chapter 4 are*: (1) what is the frontal character of stratified turbidity currents? (2) And how does this character compare to that of other particle-laden density currents?* Newly obtained high resolution direct measurement data are used to image the frontal shape, velocity structure and density structure of a stratified turbidity current.

Chapter 2: Morphodynamics and depositional signature of low-aggradation cyclic steps: New insights from a depth-resolved numerical model

This chapter is published in *Sedimentology* in 2017 under the same name, doi:10.1111/sed12391. It is co-authored by Dr Matthieu Cartigny, Dr Joris Eggenhuisen and Ernst Hansen. An edited version of the paper is presented in this thesis.

I did the numerical modelling, analysis of the modelling outcomes and wrote the manuscript. Matthieu Cartigny and Joris Eggenhuisen aided in discussing the results, and in reviewing of the manuscript. Ernst Hansen provided help on setting up the numerical model.

2.1 Abstract

Bedforms related to Froude-supercritical flow, such as cyclic steps, are increasingly frequently observed in contemporary fluvial and marine sedimentary systems. However, the number of observations of sedimentary structures formed by supercritical flow bedforms remains limited. The low number of observations might be caused by poor constrains on criteria to recognise these associated deposits. This study provides a detailed quantification on the mechanics of a fluvial cyclic step system, and their depositional signature. A computational fluid-dynamics model is employed to acquire a depth-resolved image of a cyclic step system. New insights into the mechanics of cyclic steps shows that: (1) the hydraulic jump is, in itself, erosional, (2) there are periods over which the flow is supercritical throughout and there is no hydraulic jump, which plays a significant role in the morphodynamic behaviour of cyclic steps, and (3) that the depositional signature of cyclic steps varies with rate of aggradation. Previous work has shown that strongly aggradational cyclic steps, where most of the deposited sediment is not reworked, create packages of backsets, bound upstream and downstream by erosive surfaces. Here the modelling work is focussed on less aggradational conditions and more transportational systems. The depositional signature in such systems is dominated by an amalgamation of concave-up erosional surfaces and

low-angle foresets and backsets creating lenticular bodies. The difference between highly aggradational cyclic steps and low aggradation steps can be visible in outcrop both by the amount of erosional surfaces, as well as the ratio of foreset to backset, with backsets being indicative of more aggradation.

2.2 Introduction

Large quantities of sediment are transported by high-discharge events, such as floods or jökulhlaup (Nordin and Beverage, 1965). Such events are prone to Froude-supercritical flow, where surface waves cannot migrate upstream as the flow velocity exceeds the wave-propagation velocity. Froude-supercritical unidirectional sediment-laden flow over an erodible sediment bed leads to the formation of bedforms such as antidunes (Kennedy, 1969; Alexander et al., 2001), and at higher Froude numbers cyclic steps (Winterwerp et al., 1992; Parker, 1996; Taki and Parker, 2005; Kostic et al., 2010; Cartigny et al., 2014). Transitional bedforms, such as unstable antidunes and chutes-and-pools, populate the bedform stability diagram at flow-intensities between antidunes and cyclic steps (Alexander et al., 2001; Cartigny et al., 2014; Kostic, 2014). Supercritical flow conditions in fluvial settings (which are open-channel flows) creating supercritical-flow bedforms, have been reported in mountain streams (Kostic et al., 2010), on glacial outwash planes (Lang and Winsemann, 2013) and on beaches and dredging disposal sites (Winterwerp et al., 1992). Froude-supercritical conditions are reached more quickly in sediment gravity flows, such as turbidity currents and pyroclastic flows, due to the small density contrast between the flow and the ambient fluid that reduces the wave-propagation velocity. The large number of observations of Froude-supercritical flow related bedforms on the seafloor, mainly found in submarine canyons and steep delta slopes, reaffirms the prevalence of Froude-supercritical flows in marine settings (Symons et al., 2016).

Developments in physical and numerical modelling of supercritical-flow bedforms, (Kennedy, 1969; Jorritsma, 1973; Foley, 1977; Winterwerp et al., 1992; Parker and Izumi, 2000; Alexander et al., 2001; Fagherazzi and Sun, 2003; Sun and Parker, 2005; Taki and Parker, 2005; Fildani et al., 2006; Kostic and Parker, 2006; Alexander, 2008; Sequeiros et al., 2009; Spinewine et al., 2009; Kostic et al., 2010 Paull et al., 2010; Cartigny et al., 2011; Kostic, 2011; Balmforth and Vakil, 2012; Cartigny et al., 2014), have sparked a large number of observations of supercritical-flow bedforms in modern systems (Fildani et al., 2006; Lamb et

al., 2008; Duarte et al., 2010; Jobe et al., 2011; Hughes Clarke et al., 2012; Babonneau et al., 2013; Maier et al., 2013; Covault et al., 2014; Fricke et al., 2015; Tubau et al., 2015; Zhong et al., 2015; Normandeau et al., 2016; Symons et al., 2016). Despite this common and well-documented occurrence of supercritical-flow bedforms, outcrop examples of deposits indicating these flow-conditions in a fluvial setting (Fielding, 2006; Duller et al., 2008; Fielding et al., 2009; Ghienne et al., 2010; Lang and Winsemann, 2013) or in a (deltaic-) marine setting (Postma et al., 2009; Postma et al., 2014; Ventra et al., 2015; Dietrich et al., 2016) are sparse. The recent flurry of recognition of supercritical bedforms in modern environments makes it implausible that sedimentary structures indicative of these bedforms should be rare in deposits formed in comparable ancient environments.

The sparsity of supercritical sedimentary structures is often attributed to poor preservation potential of supercritical-flow-regime deposits, due to reworking by subcritical flows in the waning stages of high-discharge events. Froude-supercritical flows also tend to form in parts of the sedimentary system that are net-erosive on a geological timescales, such as mountainous terrains (Middleton, 1965; Foley, 1977; Yagishita and Taira, 1989; Wynn and Stow, 2002; Fielding, 2006; Duller et al., 2008; Ponce and Carmona, 2011; Lang and Winsemann, 2013; Macdonald et al., 2013; Cartigny et al., 2014; Postma et al., 2014; Ventra et al., 2015). An alternative explanation for the sparse recognition of supercritical regime facies is that their depositional signature is poorly understood.

Transportational cyclic steps in open-channel flows, which are neither net-erosive nor net-depositional (Parker and Izumi, 2000), have been modelled experimentally in flume tanks (Taki and Parker, 2005; Cartigny et al., 2014), and modelled numerically using depth-averaged models (Fagherazzi and Sun, 2003). Cyclic steps in subaqueous settings have been modelled in flume experiments (Spinewine et al. 2009) and with depth-averaging numerical models (Fildani et al., 2006; Kostic and Parker, 2006; Kostic et al., 2010; Cartigny et al., 2011; Kostic, 2011; Covault et al., 2014; Kostic, 2014; Covault et al., 2017). These studies have provided valuable insight in the development and mechanics of cyclic steps, by exploring how average flow velocity, sediment concentration, and flow thickness vary over the length of the bedform wavelength (Fig. 1). These depth-averaged studies have also shown how the co-variation of these three average properties leads to upstream migrating cyclic steps, caused by erosion beneath the accelerating supercritical flow over the lee-side, and deposition beneath the

subcritical flow over the stoss-side. The transition between the supercritical flow regime and the subcritical flow regime is characterised by a hydraulic jump, where the flow abruptly expands and decelerates. Little is known about the vertical variation in flow velocity, sediment concentration, and turbulence, that occur over a cyclic step bedform, because this variation is hard to constrain with experimental measurements and averaged out in depth-averaged modelling studies. These parameters are, however, crucial to linking flow dynamics to the sedimentary architecture and facies variation over time and space. Moreover, interpreting supercritical-flow processes from outcrops and cores is strongly dependent on distinguishing small scale facies characteristics.

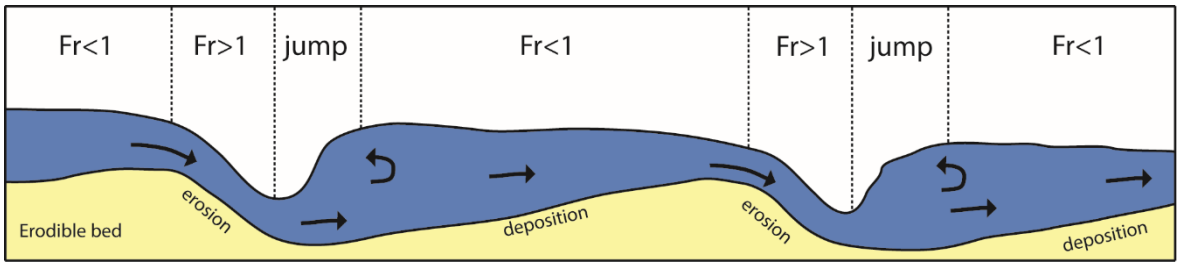

Figure 1: A schematic drawing of a cyclic step system. The stoss-side of the cyclic step is associated with a subcritical (Fr<1) and depositional flow. The lee-side of cyclic step bedform is characterized by supercritical (Fr>1) and erosive flow. The transition between supercritical and subcritical flow is marked by a hydraulic jump.

The aim of this study is two-fold: (1) quantifying flow properties in a depth-resolved manner to understand the mechanics of a fluvial cyclic step system, and (2) linking the flow dynamics of a transportational cyclic step system to the depositional signature to predict what type of deposits are expected to be associated with cyclic steps. (3) The new depositional model for transportational cyclic steps is then compared to a widely accepted depositional model of (aggradational) cyclic steps.

2.3 Methodology

Linking large-scale bedforms and associated facies to flow dynamics in a numerical model is possible if the depositional and erosive processes are fully resolved. Ideally such model would include a three-dimensional distribution of all fluid and grain velocities, sediment concentrations and grain sizes. Such a model would also take into account intergranular interactions between individual grains and have a two-way coupling, in which sediment is affected by fluid motion and vice-versa. Direct Numerical Simulations (DNS) are now capable of resolving all these processes to the individual grain scale (e.g. Cantero et al., 2008; Soldati and Marchioli, 2012; Kidanemariam and Uhlmann, 2014). However, DNS is presently only viable for a small number of grains, in a relatively small spatial domain, and at low Reynolds numbers, due to the high computational power required for DNS. Because of the computational limitation on DNS, it is not a feasible method to model cyclic steps in natural flows, which have high Reynolds numbers, a large number of grains, and are to be simulated over a longer time-scale.

Reynolds-Averaging Navier-Stokes (RANS)-models, like DNS models, employ the Navier-Stokes equations: the mass-conservation and momentum-conservation equations that describe the motion of fluids (Eq. 1.1-1.4 in appendix 2.1). Unlike DNS, RANS-models do not solve the Navier-Stokes equations to the smallest spatial and temporal scale at which eddies can occur, the Kolmogrov scale, but solve time-averaged equations and use a turbulence model to approximate the small-scale turbulence. By using a RANS-approach, the computational time can be greatly reduced. Vertical variation is however maintained, in contrast to previous depth-averaging models. In this study the RANS-model FLOW-3D® (FlowScience, Santa Fe, New Mexico) is used, in combination with a two-equation k-ε renormalisation group (RNG) turbulence model, applying the turbulent viscosity assumption, for details see appendix 2.1. Basani et al. (2014) and Ge et al. (2017) use the same model to simulate turbidity currents and can provide further detail.

2.3.1 Sediment transport models

Individual sediment transport models are used to compute bed-load transport and suspended-load transport. Grain-grain interactions are not incorporated into the suspension model, something which start to play a significant role at

sediment concentrations >9 vol. % (Bagnold, 1954). Neither does the model take into account any turbulence modification as a results of suspended sediment.

The onset of sediment movement depends on the shear stress exerted on the bed, which mobilises the sediment, and the submerged weight of the grains, resisting mobilisation. The bed shear stress is non-dimensionalised in the Shields parameter (θ), using sediment particle scales and fluid scales (Eq.2.1 in appendix 2.2). Sediment is transported if the local Shields parameter exceeds the critical shields parameter (θ_{cr}). The critical Shields parameter is described by the Shields-curve, which is approximated by an algebraic expression as formulated in Guo (2002; Eq. 2.2). The critical Shields parameter is corrected for slope effects (Eq. 2.4) as slopes in cyclic step systems can reach up to 15 degrees.

2.3.1.1 Bed-load transport

Bedload transport consists of the saltation and rolling of sediment along the bed, and is modelled using the empirical equation (Eq. 2.6, 2.7) of Meyer-Peter and Müller (1948). Meyer-Peter and Müller tested is constructed based on observation of grain-sizes down to 3mm. 350 μm sediment is used herein. The Van Rijn (1984) bed-load equation is tested down to 200 μm, and thus is more appropriate to grain sizes used herein. However, the Van Rijn equation was not availbe in the FLOW-3D® package used, and we therefore had to use the Meyer-Peter and Muller equation. Given that suspended load transport dominates over bed-load by an order of magnitude, we agrue that the choice of bedload equation will not have made a substantial impact on the overall outcome of the study. The use of the specific bed-load transport equation will thus only have minor effecrs on the outcomes of this study.

2.3.1.2 Suspended-load transport

Three aspects of suspended load transport are simulated: (1) sediment entrainment into suspension, (2) sediment settling out of suspension, these two opposing processes occur simultaneously, and (3) advection and turbulent diffusion of sediment.

A sediment-entrainment flux is expressed as a lift velocity (Eq. 2.11), which is the flux divided by the computational cell area (Mastbergen and Van Den Berg, 2003). Similarly, the settling mass-flux of sediment is calculated using equation 2.12 (Soulsby, 1997). The suspended sediment concentration at a given location is computed by solving a transport equation (Eq. 2.13).

2.3.2 Simulation setup

To validate the model, the simulations are compared to an experimental study on fluvial cyclic steps (Cartigny et al., 2014). Their flume setup in the EUROTANK flume laboratory is here reproduced numerically. The focus is on two experimental runs (9 and 15) which produced a stable train of cyclic steps.

Table 1: Details on the generated mesh of the simulated domain

Direction	Size	Number of cells	Cell size (min-max)
x	12m	360	3cm
y	0.15m	3	5cm
z	1m	38	1.8cm-8.5cm

The experimental flume is modelled using a meshed volume (Fig. 2) of 12m by 0.15m by 1m, in the x, y and z-directions (table 1). The width in the flow-normal y-direction has been downsized to save computational time. Boundary conditions consist of: an inflow condition, with a specified discharge, at the x=0m, an outflow at x=12m, a no-slip wall condition on the Y_{min} and Y_{max} boundaries, the sides of the flume tank, and a wall on the Z_{min} boundary, the flume tank bottom.

FLOW-3D automatically computes the maximum possible numerical time-step within stability limits and given minimum and maximum time-step. See stability considerations and pressure stability equations in FLOW-3D manual (Flow Science, 2014) The minimum time-step is set at 10^{-6} second. The average time-step in the simulations was $2.86 * 10^{-3}$ second.

Table 2: Details on parameterisation of the simulations

[a] Based on Mastbergen & Van Den Berg, 2003

[b] Meyer-Peter and Muller relation, value based on Wong & Parker, (2006)

[c] based on FLOW-3D release notes and manual (Flow Science, 2014)

Simulation	Specific discharge (m^2/s)	sediment concentration at inlet (vol %)	Entrainment coefficient[a]	Bed-load coefficient[b]	Drag coefficient	Angle of repose (deg)	Packing fraction	Initial bed inclinatio (deg)	Turbulent length scale (m)
1	0.77	5.6	0.018	4[b]	1	32	0.64	0.5	0.01[c]
2	0.93	5.6	0.018	4[b]	1	32	0.64	0.5	0.01[c]

A planar sediment bed of 350μm diameter grains (medium sand) was placed on the bottom of the modelled flume tank with a slope of 0.5 degrees. Near the outflow boundary a non-erodible wedge is introduced to mimic a standing body of water located at the flume expansion tank, which prevents excessive erosion. The initially smooth sediment bed interacts dynamically to the flow conditions by erosion and deposition. The EUROTANK is a recirculating flume and the current numerical setup accounts for this recirculating nature by having an inflow boundary conditions with a constant (and unlimited) supply of sediment of 5.6% of the mixture by volume.

Numerical simulation 1 reproduced run 9 performed in the laboratory, with a specific discharge of 0.077m²/s and grain size of 350μm. Simulation 2 reproduced run 15, with a specific discharge of 0.093m^2/s, and grain size of 350μm (table 2 for details).

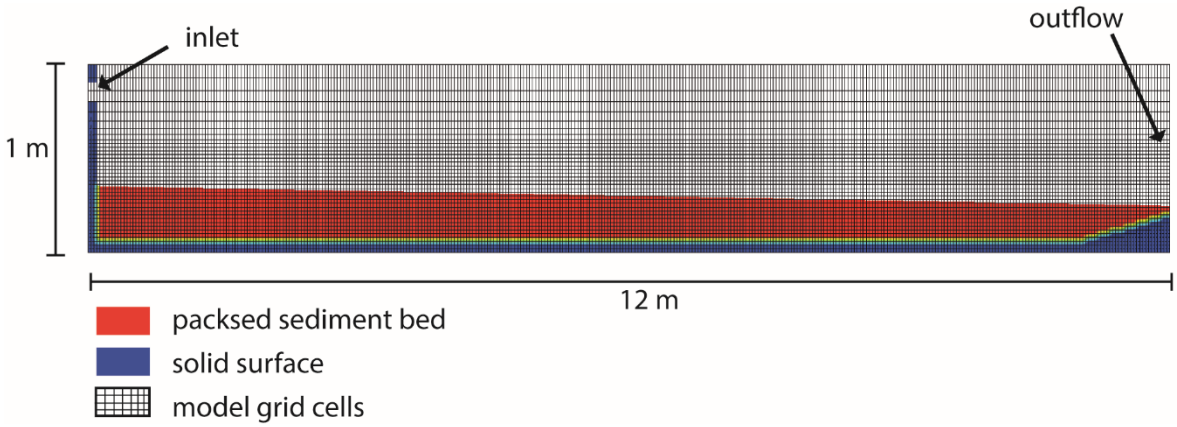

Figure 2: The model setup as used for the simulations, flow over the bed is from left to right. The experimental setup used in Cartigny et al. (2014) has a similar geometry. The packed sediment bed is indicated in red, non-erodible components are indicated in blue.

2.3.3 Validation of the model

The evolution of bed and water surface elevations display qualitative and quantitative agreement between physical and numerical simulation (Table 3 and Fig. 3). A series of cyclic steps formed spontaneously from the initially smooth bed. Erosion and deposition in the model is validated by comparing the rates at which the cyclic steps migrate. The period of bedform migration is 109 seconds in the numerical model (numerical simulation 1), and 85 seconds in the experimental results. Cartigny et al. (2014) suggest the period of migration of cyclic steps in the simulations was generally between 80-120 seconds, a range consistent with the numerical results. Unfortunately only time-series data from the laboratory experiment is available. A geometrical analysis beyond comparing the numerically generated deposit to photographs of the laboratory result was not possible.

Table 3: Comparison Froude numbers and migration period of experimental and numerical results.

Simulation / Experiment	Fr_{50}	Fr_{90}	Period migration (s)
Experimental Run 9	1.15	2.07	85
Simulation 1	1.46 (+21%)	2.25 (+9%)	109 (+30%)
Experimental Run 15	1.31	2.06	n/a
Simulation 2	1.39 (+6%)	2.21 (+7%)	118

As flow over a cyclic step is variable by nature, a comparison is made between both the median and 90th percentile of the Froude number from the Froude number time-series. Froude numbers of the numerical simulations appear to be in close correspondence to the experimental models (Fig. 3), the Froude numbers are generally <10% higher, there is however a 21% increase in median Froude number in simulation 1. Based on the similarity in migration period and Froude number variation the numerical model is assumed to give a valid representation of the cyclic step process.

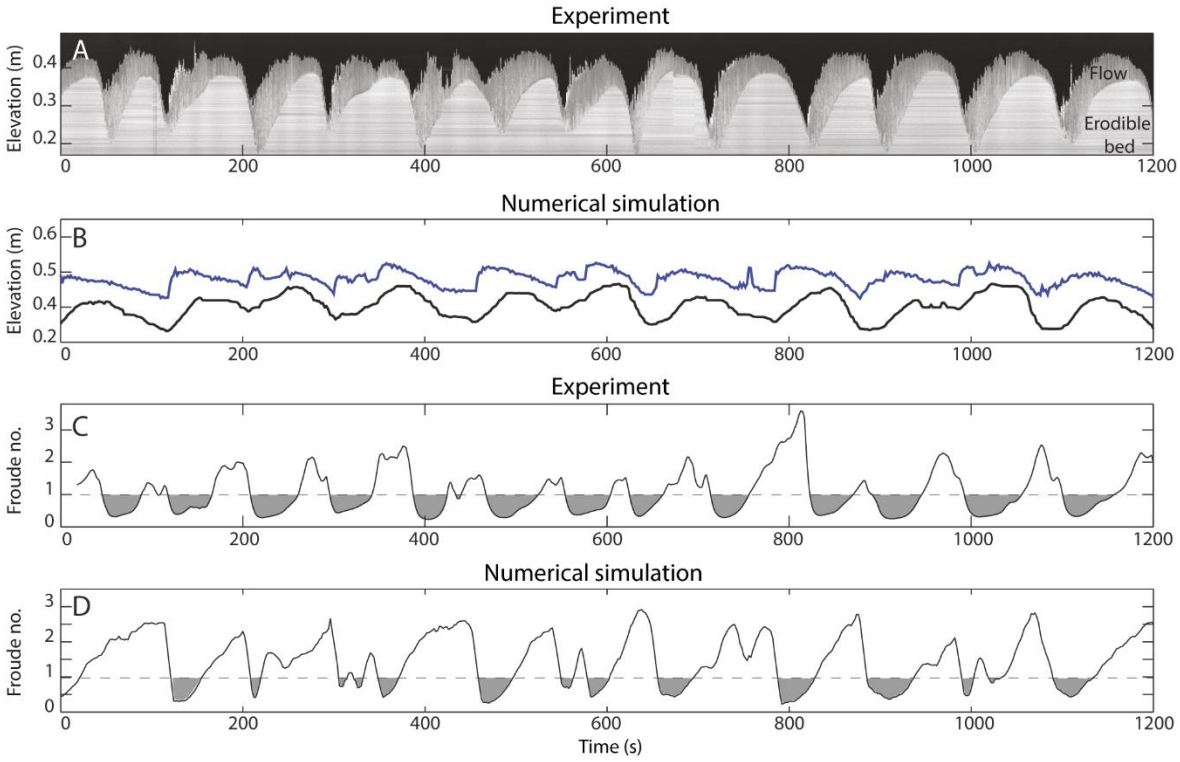

Figure 3: Time series comparison between the experimental results of Cartigny et al. (2013), run 9, and numerical simulation 1 of this study. The point of reference is a stationary location in the flume, as the sediment waves migrate a time-series is created. A: The bed-surface and free-surface elevation time-series in the laboratory experiment. B: The bed-surface and free-surface elevation in the numerical simulation. C: The Froude numbers of the experimental observations D: The Froude numbers of the numerical simulation in this study.

2.4 Flow characteristics

The interactions between the flow dynamics and the bedforms morphology in simulation 2 are here described in detail. The focus is on simulation 2, as the data in Table 3 show simulation 2 is the closest match to the physical observations. Supplementary video 2.1 shows the flow character and the interaction with the bed, and visually complements the sections on *Flow characteristics* and *Morphodynamics*.

2.4.1 General character

2.4.1.1 Observation

The simulated flow creates cyclic steps that are typically 1.5-2m in wavelength and 10-15cm in amplitude, and are associated with flows of 5-15cm thick (e.g.

Fig. 4). The flow character shows that a hydraulic jump is located in or around the trough of the bedform, separating a supercritical flow on the lee side of the bedform from a subcritical flow over the stoss side (Fig. 4). In the simulations it is observed that the hydraulic jump is present 89% of the time, which is here referred to as state 1. Flow is supercritical from crest-to-crest during the remaining 11% of the time (state 2). When present, the hydraulic jump is located upstream of the trough centre 50% of the time, at the trough centre 35% of the time, and downstream of the trough centre 15% of the time. The hydraulic jump is associated with coherent flow structures, such as stationary eddies, rollers, where the water "rolls" around and changes direction (Fig. 1). These rollers are associated with the hydraulic jump, and typically (80% of the time) located in the upper half of the flow. The remaining 20% of the time a roller forms in the lower half of the flow. The area in which rollers form is <50cm long, starting at the initiation of the hydraulic jump, with the rollers themselves being 10-20cm long and less than 10cm high. A transition from subcritical flow to supercritical flow is present close the crest of the bedform on the stoss side of the cyclic step. The average Froude number at the crest of the bedform in the simulation was 1.22 (+/- 0.15), based on an analysis of 29 individual cyclic steps.

2.4.1.2 Interpretation

The character of the flow over a cyclic step generally corresponds with that of conceptual models based on laboratory experiments and field observations (Fig. 1; Winterwerp et al., 1992; Parker, 1996; Taki and Parker, 2005; Cartigny et al., 2014). The transition from the subcritical flow regime to supercritical flow regime, at a Froude-number of unity, is commonly presumed to be at the crest of a cyclic step (Winterwerp et al., 1992; Parker, 1996; Taki and Parker, 2005; Cartigny et al., 2014). The observations in simulations herein are however more in line with classical hydraulic work which shows that the Froude number at the crest of a curvilinear convex feature is expected to occur at Fr=1.19 (Rouse, 1936).

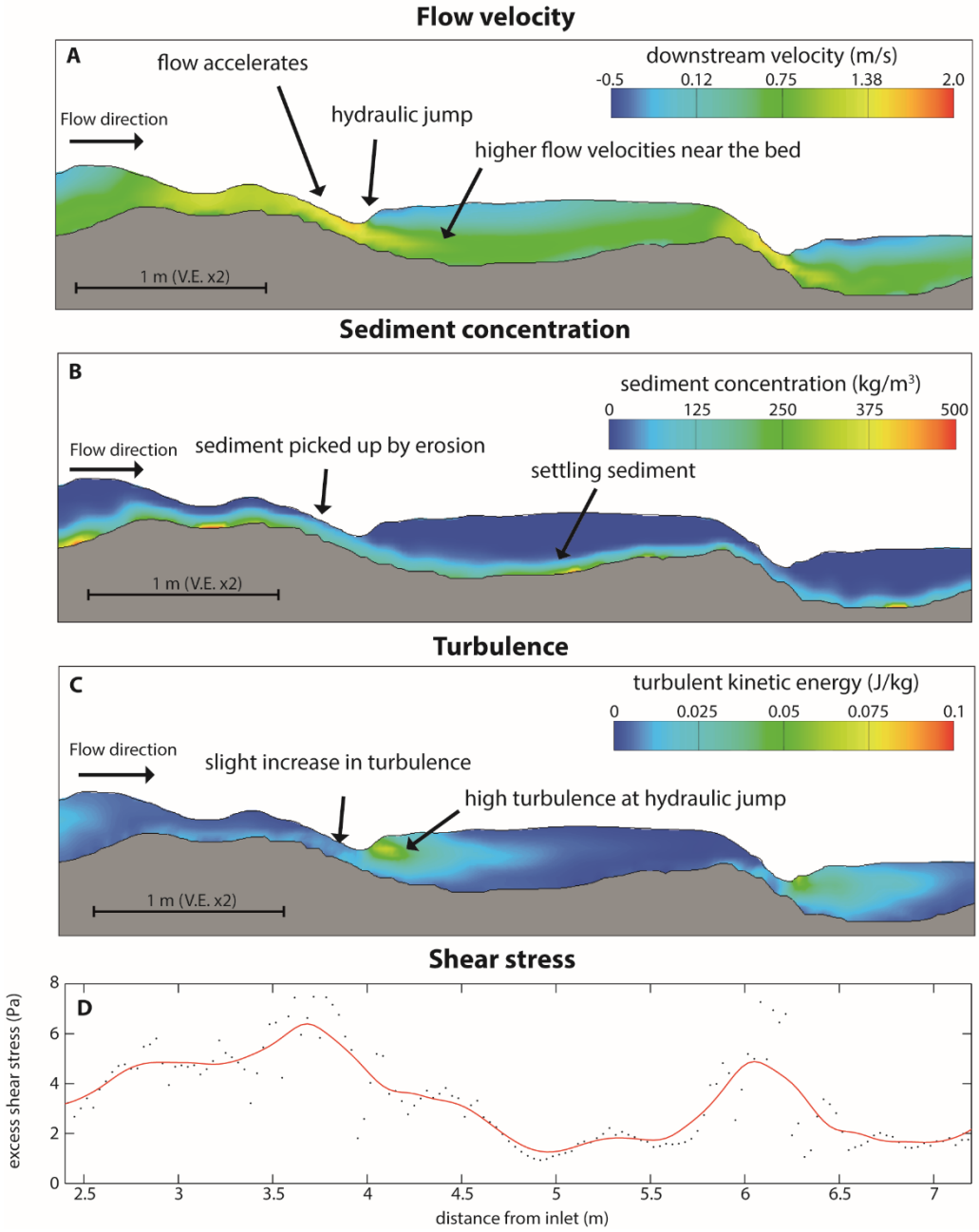

Figure 4: Snapshots of the flow conditions in a cyclic step system, please note 2x vertical exaggeration in the figures. A: The downstream-velocity field over a cyclic step. B: The sediment concentration over a cyclic step. C: The turbulent kinetic energy over a cyclic step. D: the excess shear stresses over a cyclic step in Pa (black dots), fitted with a 5 pt. moving average curve in red.

2.4.2 Velocity field

2.4.2.1 Observation

The flow accelerates over the bedform from just after the hydraulic jump up to the next hydraulic jump. In the supercritical part of the velocities of 2 m/s are reached on the lee side of the bedform, and the velocity maximum is located near the free-surface. Within the region of the hydraulic jump a specific flow pattern develops; a high velocity layer located near the bed, and a roller, associated with negative downstream flow velocities, is located on top of this layer (Fig. 4A and Fig. 5B1). In the subcritical part of the flow the flow velocities on the stoss side range from 0.5-1 m/s.

2.4.2.2 Interpretation

The supercritical flow over the lee side of the bedform has a convex-downstream velocity profile with a large velocity gradient, creating significant shear on the sediment bed (Fig. 5B4 and 5B5). In the region of the hydraulic jump the velocity profile is convex-downstream at the lowest section of the flow, and curved convex-upstream at the top section of the flow (Fig. 5B1), this flow structure is related to the rollers that develop in the hydraulic jump. The velocity profile downstream of the hydraulic jump (Fig. 5B2 and Fig. 5B3) is not typical for open-channel flow as it inherits the unusual velocity profile caused by the hydraulic jump.

2.4.3 Sediment concentration

2.4.3.1 Observation

The average sediment concentration in the flow is 5.6% by volume. A clear increase in sediment concentration over the supercritical lee side of the cyclic steps is not observed (Fig. 4B and Fig. 5C). At the region of the hydraulic jump, there is a clear difference in sediment concentration between the fast-flowing near bed layer, with concentrations between 5-10%, and the upper part of the flow, where sediment concentrations within the roller are less than 1% (Fig. 5C1 and 5C2). In the subcritical part of the flow the near-bed sediment concentrations range from 5-10% by volume. Sediment concentrations decrease towards the free

surface, where they reach near-zero values (Fig. 4B).

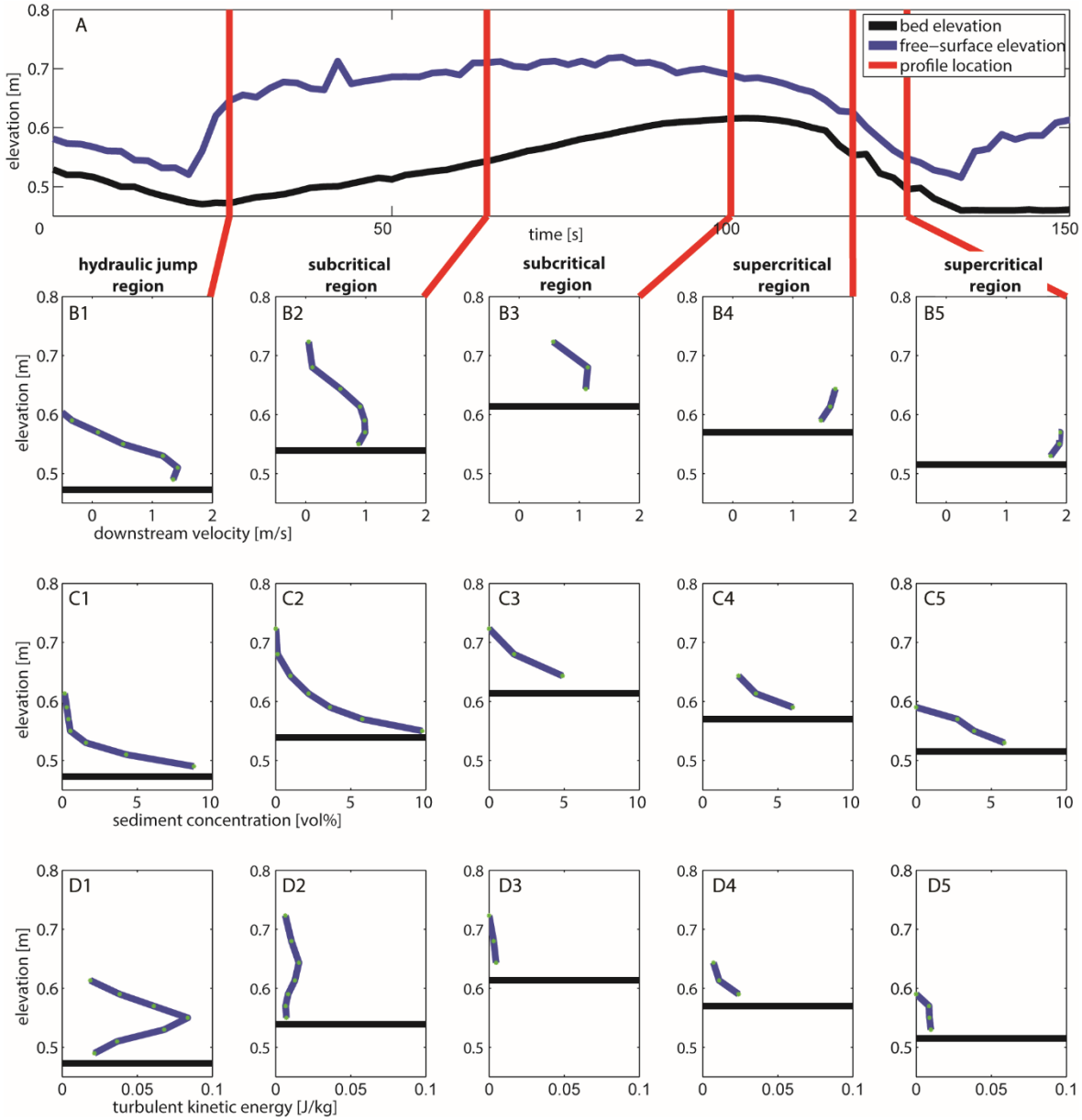

Figure 5: Profiles through the flow, one cyclic step wavelength (A), based on time-series data, showing downstream velocity (B), sediment concentration in (C) and turbulent kinetic energy (D).

2.4.3.2 Interpretation

The lack of increase in sediment concentration over the lee side of the cyclic steps is counterintuitive, as one might think that entrainment of sediment into the flow increases the sediment concentration. However, the sediment discharge is the product of the sediment concentration and flow velocity. And while depth-average sediment concentration only increases from 7 to 9%, the sediment discharge doubles over the lee side (Fig. 6F). This doubling shows that an increasing velocity forms the dominant control on the sediment discharge and

explains the counterintuitive sediment concentration trend. There is in an increase in stratification in the subcritical part of the flow, the sediment settles, causing higher sediment concentrations near the bed (Fig. 4B and Fig. 5C2 and 5C3).

2.4.4 Turbulence

2.4.4.1 Observation

Turbulent kinetic energy (TKE), the mean kinetic energy per unit-mass associated with turbulent eddies, is of the order of 0.01-0.03 J/kg in the supercritical part of the flow, with peak values near the bed where shear is highest (Fig. 5 D4 and D5). These TKE levels are equivalent to 8-14 cm/s of turbulent velocity fluctuations assuming isotropic turbulence. TKE is three to ten times higher (0.1 J/kg) in the region of the hydraulic jump (Fig. 4C and Fig. 5 D1). The subcritical region has the lowest turbulent kinetic energy, generally less than 0.01 J/kg.

2.4.4.2 Interpretation

Turbulence is generated in flow regions where shear within the flow is high (i.e. the velocity gradient), such is the case at a hydraulic jump. Turbulence is the mechanism through which sediment is suspended and dispersed in the flow. Hence, in regions of high turbulence sediment not prone to settle, despite having relatively high sediment concentrations. The combination of high turbulent energy, inhibiting settling, and a relatively high shear on the bed at the hydraulic jump is a likely cause for entrainment to outpace settling, causing the hydraulic jump region itself to be erosive.

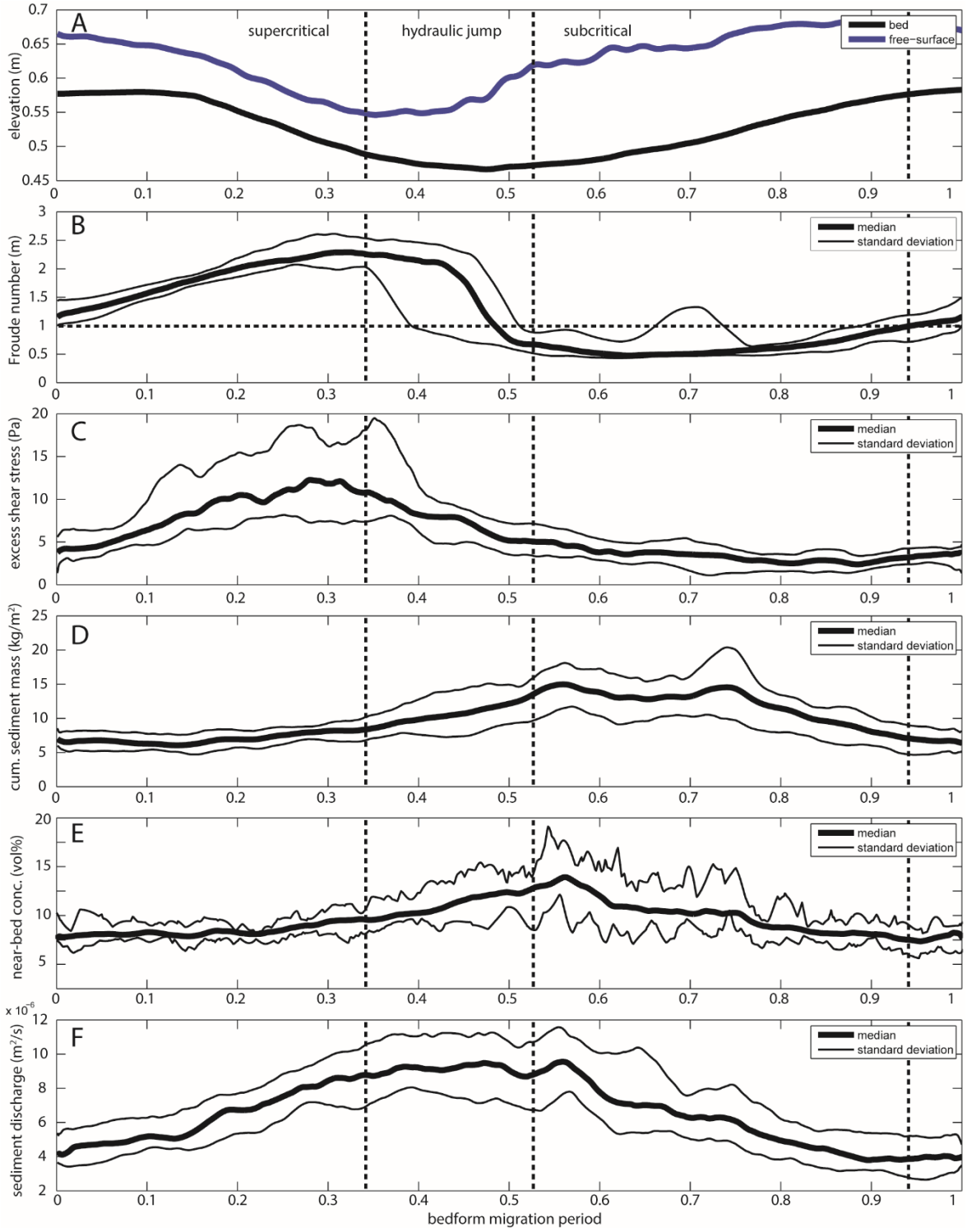

Figure 6: Six time-series plots of different physical properties over a cyclic step during one migration period. The properties are median or average properties based on 12 individual cyclic steps. One full migration period is displayed on the x-axis (0-1). The graphs display; A: average bed elevation and free-surface elevation. B: median Froude number. C: median shear stress D: median depth-integrated (cumulative) sediment mass. E: median near-bed sediment concentration, where near-bed is defined as the 2 computational cells closest to the bed. F: median downstream sediment flux (sediment discharge).

2.5 Morphodynamics

Relating the flow dynamics to bed surface evolution is crucial to understand how cyclic steps maintain their morphodynamic equilibrium. Described here are two states observed in a cyclic step system between which the system alternates (Fig. 7). *State 1* (89% of the time): there is a hydraulic jump present in the trough of the bedform, the flow is supercritical at the lee side of the cyclic step, and subcritical at the stoss side of the cyclic step. *State 2* (11% of the time): the flow is supercritical over the whole bedform and a hydraulic jump is absent, the flow over the stoss side of the bedform decelerates and thickens, but not enough to form a hydraulic jump. In state 2 the flow is still erosive over the lee side of the bedform, and depositional over the stoss side. The topographic difference between the trough of the bedform and the crest is lower in state 2 than in state 1. Supplementary videos 2.1 and 2.2 help to visualise and understand of the morphodynamics more clearly.

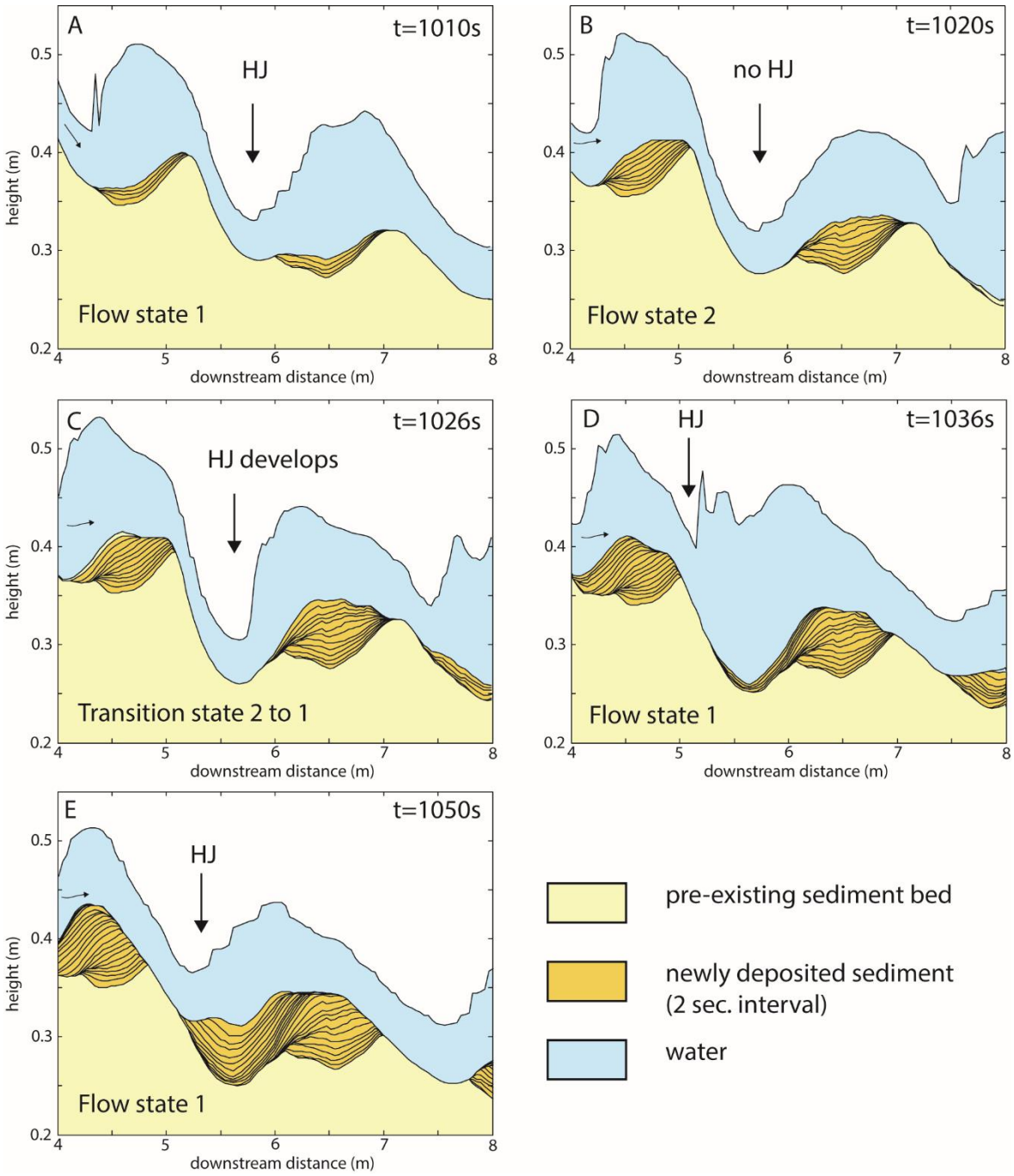

Figure 7: Five panels showing the flow behaviour during different stages of the cyclic step system, also shown are the associated newly formed deposits. The lines in the newly formed deposit are 2-second timelines.

2.5.1 Flow state 1

2.5.1.1 Observation

Supercritical flow is limited to the crest and lee side of the cyclic step in flow state 1. The excess shear stress, the shear stress that exceeds critical shear stress for movement on the bed (here 0.25Pa), increases from 5 Pa at the crest of the bedform, to 13 Pa just before the hydraulic jump (Fig. 6C). An excess shear stress larger than 0 does not mean there is overall erosion, but simply that there is some sediment entrainment. It is the local balance between the sediment entrainment flux, which increases with shear stress, and the settling flux, which determines whether there is net erosion or net deposition.

The start of the hydraulic jump is typically located at the downstream end of the lee side and is associated with the transition from the lee side to the stoss side. The hydraulic jump is mildly erosive, illustrated by its location on the lee side (Fig. 6A). The excess shear stress decreases gradually from about 13 Pa to 5 Pa within the region of a hydraulic jump (Fig. 6C and Fig. 4D).

After the flow has decelerated at the hydraulic jump, the flow slowly thins and accelerates again, while depositing sediment at the stoss side. The shear stress in the subcritical part of the flow is 4-5Pa (Fig. 6C). Both the increase in bed-height and the decrease in sediment discharge (Fig. 6A and 6F) illustrate that the Froude-subcritical region is depositional.

In state 1, more sediment is deposited nearer the trough of the bedform than at its crest, causing the topography to decrease (Fig. 7D and 7E). As the topography decreases, the hydraulic jump is washed out and disappears.

2.5.1.2 Interpretation

In state 1 the continuous acceleration of the supercritical flow over the lee side of the bedform leads to increased bed shear stress. Upstream of the crest of the bedform (0.95-1 on Fig. 6), shear stresses on the bed are low enough to allow the settling of sediment to outpace entrainment of sediment. Downstream of the crest of the bedform shear stress continuously increases, resulting in the sediment-entrainment flux to exceed the settling flux, making the flow erosive, as indicated by an increase in sediment discharge (Fig. 6F). The morphological effect of the supercritical flow is a curve at the crest of the bedform towards a linear lee side of the bedform.

At the hydraulic jump erosion is caused by high shear stresses and increased turbulence. High shear stress is explained by relatively high velocities near the bed in the hydraulic jump region (Fig. 4A and Fig. 5 A1). Increased turbulence in this region, caused by coherent flow structures, allows sediment to remain in suspension and inhibits settling. The amount of sediment stored in the water column increases over the hydraulic jump region (Fig. 6D). As a result the morphological effect of the hydraulic jump is a transition from a steep and strongly erosive lee side, through a concave trough, and to a depositional upstream dipping stoss side.

In the subcritical flow region the sediment entrainment flux is smaller than that of sediment settling flux, as low bed shear stresses limit the entrainment. The low turbulence levels in the subcritical region causes the sediment picked up on the lee side to settle. Sediment grains collect at the base of the flow before settling (Fig. 6E), thereby causing flow stratification as a result of limited mixing. The morphological response to this depositional subcritical flow region is an increase in bed-elevation over the stoss side, with more sediment being deposited close to the trough than near the crest, effectively decreasing the topography between crest and trough, setting up the system to change to flows 2.

2.5.2 Flow state 2

2.5.2.1 Observation

In state 2, supercritical flow prevails over the entire bedform. Even though the flow thickens over the stoss side of the bedform towards the crest, the flow remains supercritical. The thicker supercritical flow on the stoss side is still depositional with excess shear stresses ranging from 5-7 Pa.

More sediment is deposited at the crest than in the trough in flow state 2, thereby increasing the topography (Fig. 7B). Such increased topography caused by deepening of the trough and deposition on the crest triggers the formation of a new hydraulic jump (Fig. 7B and 7C).

2.5.2.2 Interpretation

In state 2 the lee side of the cyclic step remains erosive. Notwithstanding the supercritical flow conditions, the stoss side of the bedform is still depositional as the settling flux exceeds the sediment entrainment flux.

The morphological behaviour in state 2 is not unlike that of antidunes, because more sediment is deposited near the crest than at the trough the topography of the bedform to increases. When comparing the flow parameters with the bedform geometry through empirical equations of Kennedy (1960), and Alexander et al. (2011), it is clear that the bedforms are, however, not antidunes. An increase in topography in flow state 2 sets up the system to create a new hydraulic jump and return to flow state 1. The hydraulic jump forms at the crest of the bedforms and migrates towards the trough. This alteration between two flow states, with depositional patterns that inherently require an alteration from one state to another, is also described in a carbonate ramp setting which is interpreted to have backset beds formed by cyclic steps (Slootman et al. 2015). The cycle alternating between flow states 1 and 2 appears to be an autogenous interplay between bed topography and the flow, and is inherent to the depositional pattern of the two flow states.

2.6 Depositional signature

Sedimentary structures can be indicative of palaeo-flow conditions and therefor provide an aide to reconstruct the palaeo-environment. Hence it is important to understand the formative processes of bedforms and their associated sedimentary structures. Here the modelling results are used to directly link the flow-process to the depositional product. The cyclic step simulations provide flow conditions at the moment of deposition for each subgridded sediment parcel at every time step, and hence the model not only builds up a series of sedimentary structures, but is also able to link the individual parts of these sedimentary structures with their flow conditions during deposition.

2.6.1 Architecture

The architecture of the deposit associated with a cyclic step system is dependent on the rate of aggradation. The traditional depositional model of aggradational cyclic steps is here thus compared with the new transportational model.

In an aggradational system the architecture consists of upstream-dipping laminations (< 10°), called backsets, which form on the depositional stoss side of the bedform (Fig. 9A) (Kostic and Parker, 2006; Spinewine et al., 2009; Yokokawa et al., 2009; Lang and Winsemann, 2013). The backsets onlap onto a composite erosional surface at their upstream side, which forms the lower set-boundary. The

backsets are truncated at their downstream side by a similar erosive surface, forming the upper set-boundary.

The simulations in this study are not aggradational but transportational, this is reflected by a different depositional architecture (Fig. 9B). The resulting depositional architecture is an amalgamation of concave-up erosion surfaces and small portions of preserved low-angle backsets and foresets creating mostly concave-up lenticular bodies (Fig. 9B).

The development of the architecture of transportational cyclic steps in Fig. 9B is seen in Fig. 8A-E. A deep trough that formed during washout of the hydraulic jump is filled by sediment (Fig. 8B). The sediment laps onto the erosion surface as a foreset with a downstream transitions into a backset (<5°). This creates a concave-up deposit (Fig. 8B). A large portion of the deposited backsets is eroded by the upslope migration of the successive bedform (Fig. 8A-E). The deposits shown in Fig. 8B are mostly reworked in Fig. 8C, and only the deepest trough infill near the initial onlap is preserved. These deepest trough deposits form below the hydraulic jump. If the flow is supercritical throughout (state 2), steeper backsets and more tabular backsets are formed (Fig. 8D). These steeper, tabular backsets (<10°) are less likely to be preserved as they form near the crest, which is more prone to erosion. During the transition from state 2 (supercritical throughout), to state 1 (with hydraulic jump), erosion can occur on the stoss side, leading to upstream truncation of the laminations.

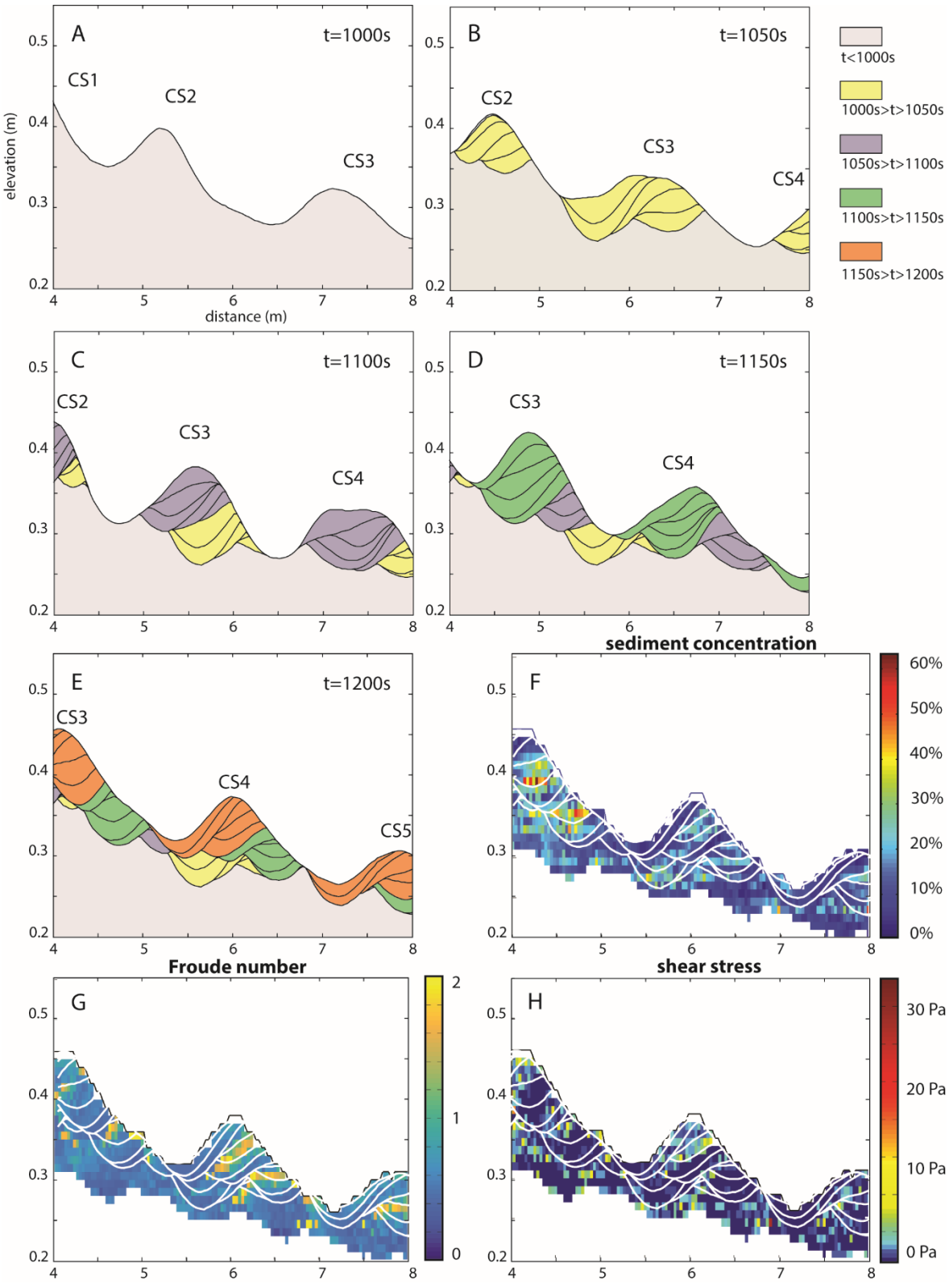

Figure 8: Panels A-E show the development of the depositional architecture of a transportational cyclic step system at 50 second time intervals, with 10 second 10 time-lines within these intervals. Panels F-H display near-bed sediment concentration, Froude number, and shear stress at the moment a sediment parcel got deposited.

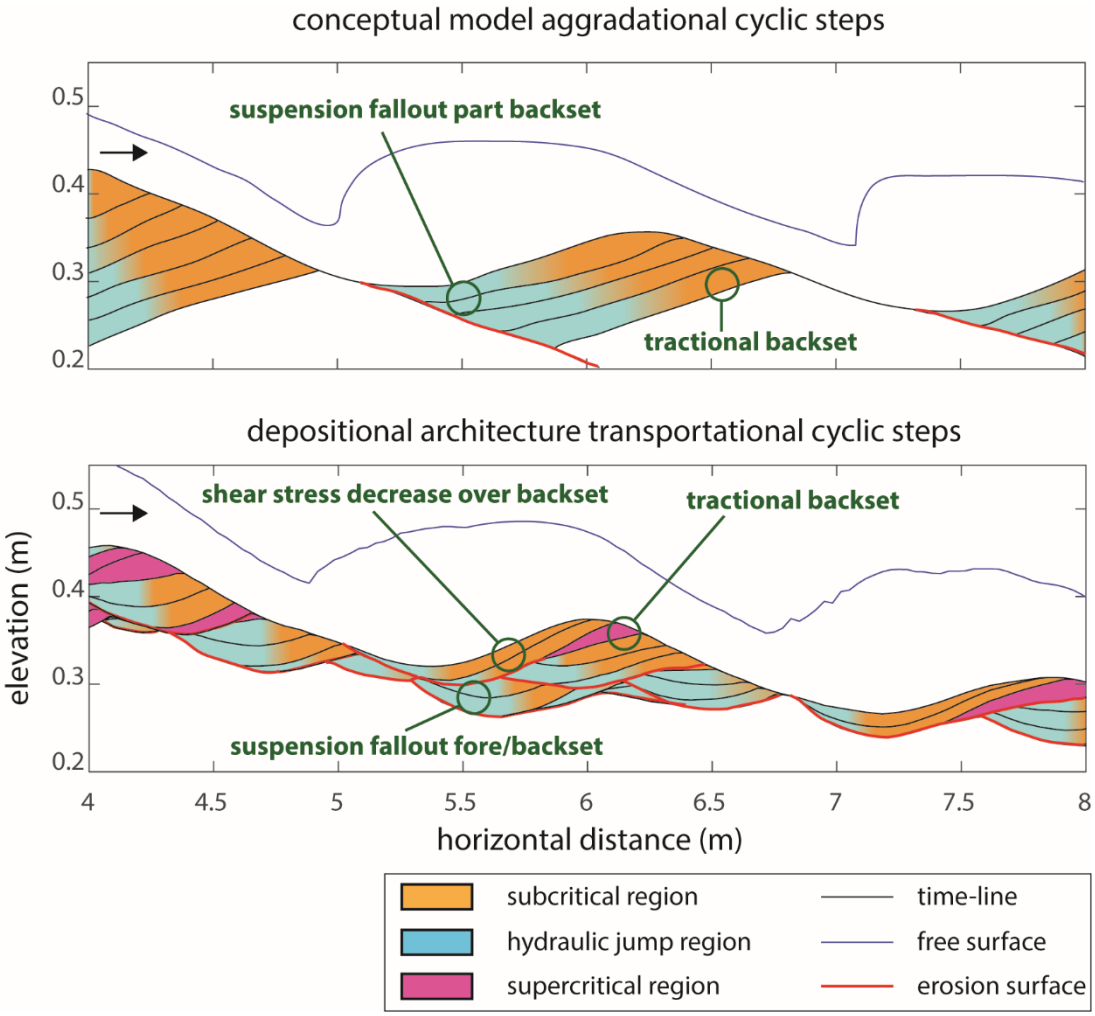

Figure 9: Depositional architectures of aggradational cyclic steps, a generally accepted model (9A) and more transportational cyclic steps (9B). The figure also shows the inferred flow regime at which the deposits got formed. Please note that the black lines are time-lines, and not necessarily laminations due to grain-size breaks.

2.7 Sediment concentration

The sediment concentration at the moment of deposition over a cyclic step (Fig. 8F) is generally lower than 9% by volume. Deposits that form under subcritical flow form at lower near-bed sediment concentration (~5%) than the deposits formed under supercritical flow (~8%) (Fig. 8F). The flow is generally dilute (<9 vol. %) in all regions (Fig. 5C), implying turbulence is the dominant grain support mechanism (Bagnold, 1954).

2.7.1 Sediment concentration

The sediment concentration at the moment of deposition over a cyclic step (Fig. 8F) is generally lower than 9% by volume. Deposits that form under subcritical flow form at lower near-bed sediment concentration (~5%) than the deposits formed under supercritical flow (~8%) (Fig. 8F). The flow is generally dilute (<9 vol. %) in all regions (Fig. 5C), implying turbulence is the dominant grain support mechanism (Bagnold, 1954).

2.7.2 Flow regime

Even though a cyclic step is characterised by supercritical flow over the lee side, the deposits are predominantly formed in the subcritical flow regime (Fig. 8G). Traces of bedforms associated with the subcritical flow regime, such as current ripples, superimposed on the larger scale bedform could therefore be formed as a consequence. Bedform stability diagrams indicate that flow over proximal backset deposits are within the ripple regime (Van den Berg and Van Gelder, 1993). Ripples have been associated with subcritical flow after a hydraulic jump in the distal part of hydraulic jump bars (Macdonald et al., 2013). Given the high settling rate following the hydraulic jump such current ripples could initially be climbing. Ripples are, however, not simulated in the numerical model due to a lack of resolution. Deposition during supercritical flow conditions (state 2) also result in a backset (Fig. 8G). Backsets deposited during supercritical flow onlap further downstream than those formed at subcritical conditions and are steeper.

2.7.3 Shear stress

Cyclic step deposits show alternation in bed shear stress over time and space (Fig. 8H). Variability in shear stress over time would lead to a variation in grains-size from one backset stratum to another, creating lamination, and thereby delineating individual backset strata. In general shear stresses at the moment of deposition decrease from trough to crest (Fig. 9B). Deposits that form directly after the rapid erosion, have lowest shear stresses as a roller forms below the main flow (20% of the time), see Fig. 9B. In absence of a hydraulic jump, shear stresses over the stoss side are relatively high and there is increased traction on the bed where the deposits form (Fig 9B).

The simulations in this study show a decrease in shear stress over the stoss side of the bedform (Fig. 6C). The decrease of flow *competence* (i.e. shear stress to

pick up sediment) to carry sediment would thus lead to a downstream fining, as is generally expected from a decrease in shear stress. Submarine cyclic steps are also suggested to be downstream fining, but not because of decrease in shear stress, as shear stress is suggested to increase over the stoss side (Postma & Cartigny, 2014). The downstream fining, as described by Postma & Cartigny (2014), would be caused by a decrease in *capacity* (i.e. turbulence to keep sediment in suspension) of the flow to carry sediment; coarser sediment falls out of suspensions more quickly leading to fining downstream. Both the capacity and competence argument can be used to explain downstream fining (Hiscott, 1994a). Open-channel-flows and turbidity currents both can create cyclic steps, but are in many ways different, in velocity-profile and concentration profile to start with, and in shear stress pattern as a consequence. Both a decrease in flow *capacity* and a decrease in flow *competence* can produce downstream fining, and it is well possible that the two mechanisms play different roles in marine and fluvial systems, but ultimately lead to a similar result.

2.8 Consequences for outcrop studies

Recognition of cyclic step deposits in outcrop is strongly dependent on the preservation potential of the deposits, and whether cyclic step systems are aggradational or transportational (Fig. 9). Deposits associated with strongly aggradational cyclic steps have a significantly different depositional signature than deposits resulting from transportational cyclic steps.

A highly aggradational cyclic step system in outcrop may resemble the deposit such as seen in Fig. 9A, which represents an idealised deposit. There is a clear sequence of backsets that are separated by a set boundary at the upstream side and at the downstream side. Postma and Cartigny, (2014) suggest that the backsets display a downstream fining caused by hindered settling at the hydraulic jump and in increase in shear stress over the stoss side. Downstream fining within sets results in a normal grading in the vertical due to progressively upstream emplacement of the backsets. Such depositional signatures of aggradational cyclic step systems are, however, uncommon in fluvial outcrops, where clear sequences of continuously stacked backsets are absent due to a lack accommodation space. In marine and deltaic settings accommodations space is more readily available, and the character described above is observed in outcrop Recognition of cyclic step deposits in outcrop is strongly dependent on the preservation potential of the deposits, and whether cyclic step systems are

aggradational or transportational (Fig. 9). Deposits associated with strongly aggradational cyclic steps have a different depositional signature than deposits resulting from transportational cyclic steps.

A highly aggradational cyclic step system in outcrop may resemble the deposit such as seen in Fig. 9A, which represents an idealised deposit. There is a clear sequence of backsets that are separated by set boundaries at the upstream side and at the downstream side. Downstream fining within sets results in a normal grading in the vertical due to progressively upstream emplacement of the backsets. Such depositional signatures of aggradational cyclic step systems are, however, uncommon in fluvial outcrops, where clear sequences of continuously stacked backsets are absent due to a lack accommodation space. In marine and deltaic settings accommodation space is more readily available, and the character described above is observed in outcrop (Ventra et al., 2015; Dietrich et al., 2016) and in shallow seismic imagery (Migeon et al., 2000; Migeon et al., 2001; Normark et al., 2002; Fildani et al., 2006; Migeon et al., 2006; Flood et al., 2009; Gilbert and Crookshanks, 2009; Heinio and Davies, 2009; Zhong et al., 2015).

Cyclic steps that are transportational have a different depositional signature (Fig. 9B) than aggradational ones. The overall depositional signature is an amalgamation of lenticular bodies bound by erosion surfaces. Similar to the backsets formed in an aggradational setting, backsets formed in a transportational setting are downstream fining. The deposited backsets are reworked for a large part; on the downstream part by upstream migrating erosion, and on the upstream part when the hydraulic jump gets washed out. At the washout stage of a hydraulic jump the trough migrates upstream rapidly and erodes underlying sediments creating a deep new trough. Sediments deposited in this trough create a concave-up lens, with the best preservation potential of the flow as the trough cut deep into the substrate, out of reach of subsequent erosion. The concave-up bodies formed at low shear stress conditions, may be associated with suspension fallout due to a decrease in flow capacity. Backsets that form when the flow is supercritical throughout (state 2) are steepest, as they enhance the existing topography. These backsets also form under relatively high shear stress where there is traction on the bed, grain sizes in these backsets are likely to be larger than average as fines will not be able to settle at these conditions (decrease in flow competence). These transportational cyclic step

deposits resemble those observed in small-scale laboratory experiments (Yokokawa et al., 2009).

When comparing the simulated depositional signature to signature in the geological record, it is important to appreciate differences of scale. Cyclic step facies have been interpreted in outcrops of deltaic settings (Dietrich et al., 2016) and glacial flood outbursts (Duller et al., 2008; Lang and Winsemann, 2013). In these settings concave-up troughs are filled with diffusely laminated backsets. The troughs are typically several metres long and the backsets within them vary in steepness between 5-20° (Lang and Winseman, 2013; Duller et al., 2008; Dietrich et al., 2016). In the numerical results show a very similar architecture, but on a smaller scale. Both in this study and in outcrop distinct concave-up troughs are filled by diffusely laminated foresets and backsets that dip 5° to 15° (Fig. 9B). Erosion surfaces in the simulations dip in the order of 5° to 15° (Fig. 9B), their abundance and the size of the preserved backsets is dependent on the rate of aggradation. The faint stratification described in Duller et al. (2008) and Lang and Winseman (2013), is likely due to a change in shear stress on the bed related to the stages in which the flow is supercritical throughout. Dietrich et al. (2016) show a series of upstream dipping backsets that are indicative of more aggradational cyclic steps, as these backsets are not crosscut by an erosive surface but rather a more continuous stack of backsets such as seen in Fig. 9A. More aggradation yields fewer erosional surfaces as well as more preservation of backsets relative to foresets.

It is important to keep in mind that this numerical method does not mimic all processes that do occur in a natural setting. The model does not take into account high-density flows (sediment concentrations >9%). At these higher concentrations grain-to-grain interactions start to play an important role and turbulence may be dampened. In this study only a medium sand is taken into account, finer sediment and certainly muds behave differently from sands as cohesive /electrostatic effects start to play an important role in their dynamics (Baas and Best, 2008).

2.9 Conclusions

The depth-resolved numerical model allows a unique insight into the mechanics of a cyclic step system, and the modelling results can be used to link the mechanics to the depositional signature.

The simulated cyclic steps generally adhere to existing conceptual models, with Froude-supercritical flow over the lee side and Froude-subcritical flow over the stoss side of the bedform. The hydraulic jump affects a large flow region and is often itself erosive. A hydraulic jump is not always present, and the flow occasionally is only supercritical, but still deposits at the stoss side. In absence of a hydraulic jump the bedform amplitude is enhanced and leads to the formation of a new hydraulic jump.

The depositional signature of a cyclic step system is dependent on the rate of aggradation. In the case of high aggradation rate, a package of backsets, bound upstream and downstream by erosive surfaces, can be found. In more transportational systems, the deposited backsets will be reworked to a large degree. The depositional signature of cyclic steps is dominated by an amalgamation of concave-up erosional surfaces and low-angle foresets and backsets creating lenticular bodies. This depositional signature is determined to a large extent by the transient nature of the hydraulic jump as it migrates upstream and downstream with respect to the trough location, and is occasionally washed out entirely. Similar geometries are visible over a range of scales in outcrop studies. Variation in shear stress at the moment of deposition, likely related to presence or absence of a hydraulic jump, results in more pronounced backsets of a distinct grain-size.

2.10 Acknowledgements

ExxonMobil, the National Oceanography Centre, Utrecht University and Complex Flow Design AS are acknowledged for funding this research. Riccardo Basani and Romain Rouzairol are thanked for their help and advice during the modelling phase of this study. Arnoud Slootman is acknowledged for fruitful discussions on the subject of cyclic step morphodynamics. Aaron Fricke, Pierre Dietrich, Svetlana Kostic and Jorg Lang are thanked for their valuable reviews that helped improve the paper significantly.

Chapter 3: Formative controls on dune-scale upstream-migrating bedforms in submarine channels

This chapter is submitted to the journal *Geology* under the same name. It is co-authored by Dr Matthieu Cartigny, Dr Michael Clare, and Dr Joris Eggenhuisen.

I did the numerical modelling, analysed the data, and wrote the manuscript. Matthieu Cartigny provided help in discussing the results, Michael Clare helped with the statistical analysis. All co-authors helped in reviewing and improving the manuscript. The format of a geology paper is short, there is supplementary material in appendix 3.

3.1 Abstract

Dune-scale upstream-migrating bedforms are abundant in submarine channels worldwide. Such bedforms are an important building block for these major conduits of sediment transport to the deep ocean; as dunes are for rivers. Unlike rivers, the formative controls on upstream-migrating bedforms in submarine channels are presently not well understood. It is thus unclear why such bedforms are not ubiquitous, and locally disappear along stretches of channels. We test hypotheses for the formation of upstream-migrating bedforms for the first time using a depth-resolved turbidity current model. In contrast to previous studies, we show that Froude-supercriticality is not sufficient to create upstream-migrating bedforms. We find that an additional Shields and Richardson parameter thresholds must be exceeded. These formative controls explain why slope and grain-size are the key physical controls on the occurrence of upstream-migrating bedforms.

3.2 Introduction

Turbidity currents, which flush submarine canyons, parallel rivers in their capacity to transport sediment around our planet (Talling et al., 2012). Sediment transport in rivers is dominated by downstream-migration of dunes (Best, 2005), whereas submarine channels are dominated by upstream-migrating dune-scale bedforms with a crescent-shape planform (Symons et al., 2016). River dunes are linked to

formative processes following decades of monitoring and research, thus enabling flow reconstructions from their deposits (Best, 2005). In contrast, the formative controls on dune-scale upstream-migrating bedforms in submarine channels are debated (Paull et al., 2010), which hinders confident interpretations of the flow dynamics in submarine channels and their resulting deposits. Three criteria have been proposed for the formation of dune-scale upstream-migrating bedforms (UMBs): 1) Froude-supercritical flow (Cartigny et al., 2011; Kostic, 2011; Ohata et al., 2017); 2) density-stratification within the flow (Postma and Cartigny, 2014; Hughes Clarke, 2016); and 3) a measure of sediment transport (Parker and Izumi, 2000; Balmforth and Vakil, 2012; Ohata et al., 2017). These criteria are mainly based on open-channel (i.e. river) observations, even though turbidity currents have a different velocity and density structure to rivers (e.g. Altinakar et al., 1996). We now briefly discuss these criteria and their application to turbidity currents.

3.2.1 Froude criticality

UMBs form at supercritical Froude numbers (Fr>1; Alexander et al., 2001; Cartigny et al., 2014) in open channels. Supercritical flow is also thought to be important for UMBs created by turbidity currents (Covault et al., 2016). While new field-scale monitoring (Hughes Clarke, 2016; Hage et al., 2018) has directly linked upstream-migration of crescent-shaped bedforms to turbidity currents that undergo a series of hydraulic jumps ('cyclic steps' *sensu* Parker, (1996)), the lack of sediment concentration measurements inhibits the quantification of densimetric Froude number. Therefore the specific role of Froude supercriticality is unclear in the formation of UMBs.

3.2.2 Density stratification

Conceptual models suggest that dune-scale UMBs are related to turbidity currents that are internally stratified (Postma and Cartigny, 2014). This hypothesis is supported by acoustic imaging of a highly attenuated (denser) basal layers of turbidity currents that caused upstream bedform migration (Hughes Clarke, 2016). The role of flow stratification on upstream-bedform migration in submarine channels does, however, remain uncertain as no direct measurements within such dense basal layers exist.

3.2.3 Transport regime

UMBs associated with cyclic steps vary from net-erosional (Fildani et al., 2006; Izumi et al., 2017) to net-depositional (Kostic and Parker, 2006). Modelling studies have shown that erosion plays a key role in establishing an upstream migrating train of cyclic steps, even in net-depositional settings (Parker and Izumi, 2000; Balmforth and Vakil, 2012). This points to the importance of spatial variations in sediment transport regimes. The sediment transport regime is determined by the Shields parameter. The relation between the Shields parameter and UMBs has so far only been discussed for open-channel flows (Ohata et al., 2017).

3.2.4 Aims

Here, we systematically investigate the formative controls on dune-scale upstream-migrating bedforms in submarine channels, to explain both their widespread occurrence and their localised absence. We use a depth-resolved numerical model that simulates vertical stratification, internal flow instabilities and basal erosion (Basani et al., 2014). For the first time we aim to quantify the role of the three hypothesised criteria for the inception of UMBs in submarine channels: (1) Froude supercriticality, characterised by the densimetric Froude number (Fr'); (2) internal density-stratification, characterised by gradient the Richardson number (Ri_{gr}); and (3) the sediment transport regime defined by the Shields number (Θ).

3.3 Methodology

We use a computational fluid-dynamics model (FLOW-3D®) that uses a Reynolds-Averaging Navier-Stokes approach and accounts for both erosion and deposition. This model has previously been used to simulate both turbidity currents (Basani et al., 2014; Ge et al., 2017) and cyclic step instabilities in open-channel flows (Vellinga et al., 2018). The model assumes: bedload transport following Meyer-Peter and Müller, 1948; suspended load transport with reference to bulk flow advection; no grain-to-grain interactions; turbulence-induced sediment diffusion; no turbulent modification by sediment; sediment entrainment according to Mastbergen and Van Den Berg, 2003; and hindered sediment settling (see full model description in Basani et al., 2014).

Boundary conditions were based on the Squamish submarine delta, where direct monitoring has linked turbidity currents to upstream-migration of bedforms (Hughes Clarke, 2016) (appendix 3.1). In each run, a two hour-long turbidity current was simulated over an inclined erodible bed with a metre-scale random rugosity. The model space was 20 m vertical x 200 m horizontal (Fig. 1), with a grid resolution of 0.1 m vertical x 0.4 m horizontal. One boundary condition variable was systematically adjusted in each of the 23 runs within the following ranges: incoming flow velocity (1.5-4.5 m/s); initial sediment concentration (2.8-5.6 vol. %); incoming flow thickness (0.5-2 m); and initial slope (2.7-6.1°), d_{50}=150μm (appendix 3.2).

Each of the three hypothesised controlling criteria were quantified from the model outputs (appendix 3.3 for equations). Depth- and time-averaged bulk densimetric *Froude numbers* were calculated using the integral relation of Ellison and Turner, (1959). We present median Froude number (Fr_{50}, Fr_{90}) sensu Cartigny et al., (2014). The *Gradient Richardson number* (Ri_{gr}) was used to define stratification. Stratification is defined by a Ri_{gr}>0.25 at any height in the flow profile (Howard, 1961; Miles, 1961; Armenio and Sarkar, 2002; appendix 3.4). The *Shields parameter* is used to characterise the transport regime of the sediment in the flow and on the bed. We present data for the 90th percentile of the Shields parameter (Θ_{90}) to represent peak shear stresses for each model run.

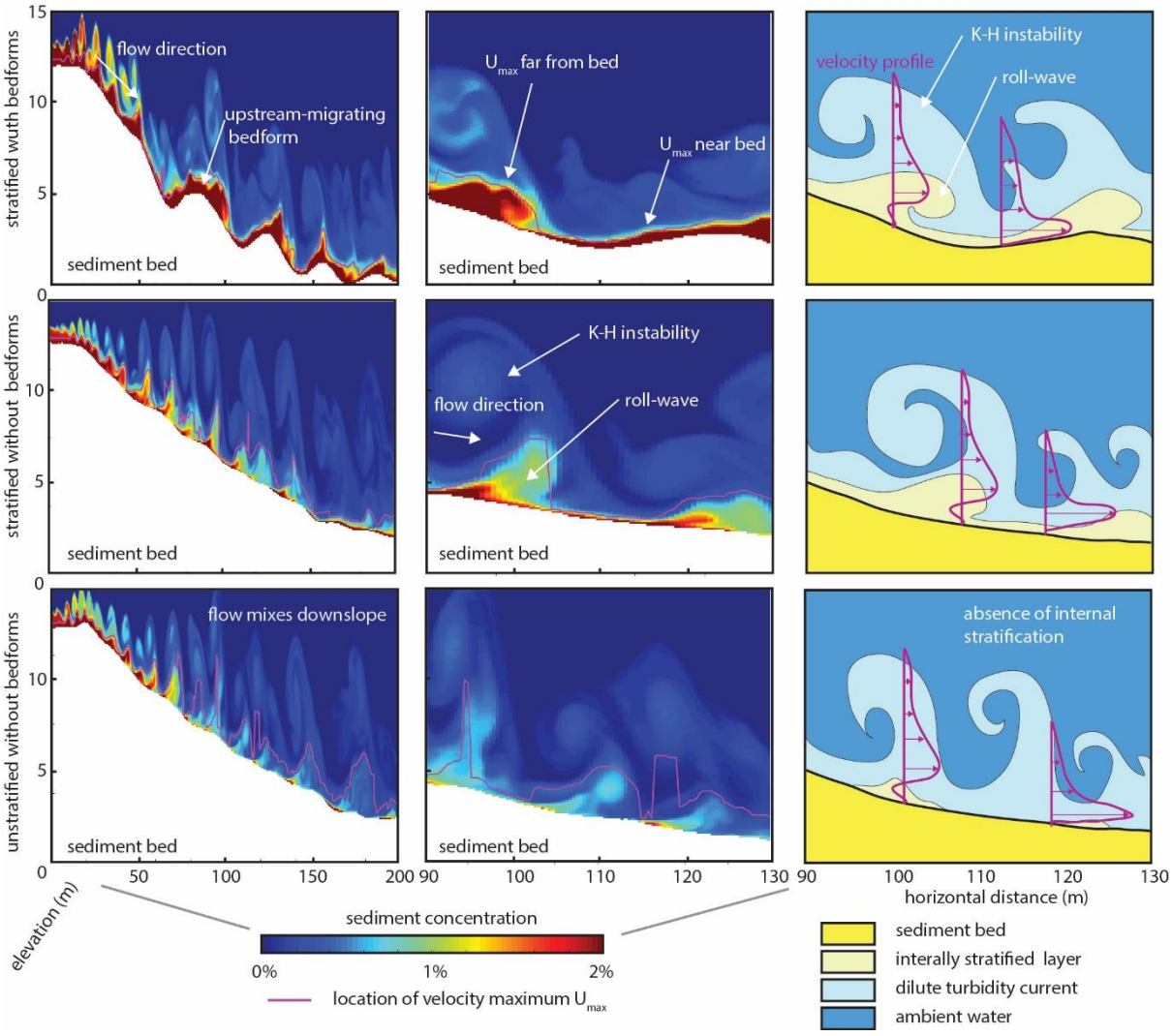

Figure 1: Model outputs of three different types of simulated turbidity currents. Stratified flows that create upstream-migrating bedforms (top panels), stratified flows that did not create bedforms (middle panels), and unstratified flows that did not create bedforms (bottom panels).

3.4 Results

The upstream-migrating bedforms emerged in only 10 of the 23 runs (see representative videos in the supplementary material). If UMB did form, then the bedforms had a similar wavelength (10s of metres) and wave height (up to few metres) to dune-scale UBMs at Squamish and in many other submarine settings (Symons et al., 2016). We now explore each of the hypothesised criteria, to understand how they relate to flows that did (N=10), or did not (N=13) create UBMs.

3.4.1 Froude supercriticality

All but one turbidity current were Froude supercritical (Fr_{50}=0.86-1.7, Fr_{90}=1.6-2.8; appendix 3.2), also those that did not form UMBs. Therefore, Froude-supercriticality does not necessarily give rise to those bedforms. There is no relation between Fr_{50} or Fr_{90} and the formation of UMBs (Figure 2A&B).

3.4.2 Stratification

UMBs were not observed in unstratified flows (N=4; Fig. 2B and C). Only 10 of the 19 stratified flows produced UMBs (Fig. 2B and C). Therefore, internal stratification seems required to generate UMB, but on their own Froude-supercritical internal-stratified flows do not always generate the bedforms.

3.4.3 Transport regime

The 10 Froude-supercritical internal-stratified flows that created upstream migrating bedforms consistently exerted high peak shear stresses on the bed (θ_{90}>2; Fig. 2A and C). We thus conclude that only Froude-supercritical and internal-stratified flows associated with high bed shear stresses form dune-scale upstream-migrating bedforms.

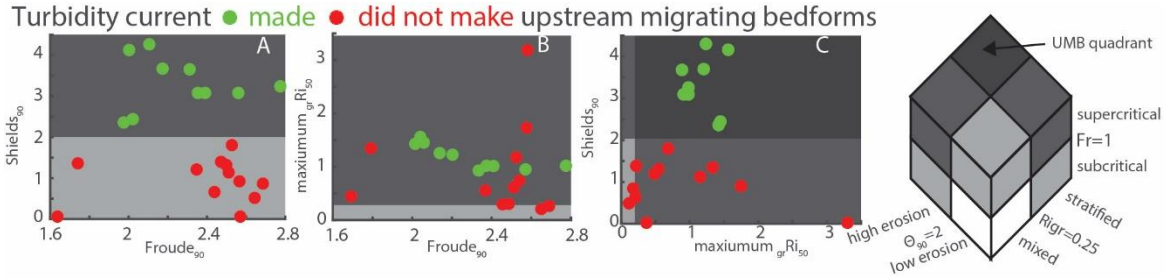

Figure 2: Diagrams presenting which flows created dune-scale upslope-migrating bedforms and which did not. A: plotted in Shields number versus Froude number diagram B: plotted in Froude number versus gradient Richardson number diagram. C: plotted in Shields number versus gradient Richardson number diagram. D: 3D diagram using Shields, Froude and gradient Richardson numbers.

3.5 Discussion

3.5.1 Not all Froude supercritical flows create upstream-migrating bedforms

All but one simulated turbidity currents were Froude supercritical. It is questionable, however, whether bulk Froude numbers are a useful descriptor for internally stratified turbidity currents. Stratified layers within a flow can have individual Froude numbers, for example the top layer of the flow might be in a supercritical regime, while the denser basal layer might be in a subcritical flow state (Dorrell et al., 2016). As it is the basal layer that shapes the bed, characterising the flow by a bulk Froude number might not provide constrains on this bedform-generating layer.

3.5.2 Flow stratification is essential for upstream-migration of dune-scale bedforms

Previous depth-averaged modelling of turbidity currents has implicated the ratio of sediment fall-velocity to initial flow conditions (concentration, velocity, and thickness), slope, and bed shear stress as the formative controls on UMBs (e.g. Kostic, 2011; Covault et al., 2016). Given their depth-averaged nature, such studies were unable to include the effects of stratification. With a depth-resolved model, we show that only internally stratified turbidity currents created dune-scale UMBs, and that an erosion threshold (θ_{90}>2) must also be overcome. This observation matches and quantifies both the conceptual model of Postma & Cartigny (2014) and direct monitoring of field-scale turbidity currents by Hughes Clarke (2016).

3.5.3 Erosion and the role of flow instabilities

A closer look at the erosional threshold reveals that erosion is strongly linked to flow instabilities occurring in the basal flow layer. The basal layer of the stratified currents is not constant in thickness, instead the basal layer is characterised by downstream migrating pulses that strongly resemble breaking waves (Fig. 1). Such instabilities are typical at stratification-interfaces of turbidity currents in both the laboratory (Cartigny et al., 2013) and the ocean (Sumner and Paull, 2014), and have previously been linked to bedform formation (Tilston et al., 2015). These instabilities could be formed by two processes. First, the instability

could be triggered by downward propagation of the Kelvin-Helmholtz instability in a lower layer: "bottom billows" (Negretti et al., 2017). Second, the instability represents the formation of roll-waves on the interface. Such roll-waves are a downstream-propagating instability found in Froude-supercritical flows, similar to a bore (Cornish, 1934; Balmforth and Mandre, 2004). This instability curls in the opposite (downstream) sense to the Kelvin-Helmholtz instability, which more closely resembles the flow pattern observed in the results (Fig. 1), thus we favour the roll-wave interpretation. The roll-waves have a profound effect on the velocity and density structure of turbidity currents. This instability is associated with a thickening of the denser basal-layer during the breaking wave phase of the roll waves, and thinning between in waves (Fig. 1), which is similar to laboratory observations (Cartigny et al., 2013). There is a significant relationship between shear stress and the height of the velocity maximum (appendix 3.5). Shear stresses are low beneath the breaking role waves when the velocity maximum is far from the bed, hence the flow would be more depositional. Shear stresses exceeds the threshold when the flow thins between the waves, because the velocity maximum is then closer to the bed. Such "bursts and sweeps" of erosion and deposition have been inferred from turbidite deposits (Chough and Hesse, 1980) and experimental studies (e.g. Sumner et al., 2008; Cartigny et al., 2013). It is this "burst" between passing roll waves that trigger the θ_{90} threshold and thus form an essential role in the formation of upstream-migrating bedforms. At high Froude numbers, however, the breaking roll-waves become so strong that their induced mixing reduces the internal-stratification needed for the bedforms. This might explain the surprising absence of the bedforms at higher Froude number flows.

3.5.4 Where is the "sweet-spot" for upstream-migrating bedforms in turbidity currents?

Finally, we return to the three hypothesized controlling parameters (Froude number, gradient Richardson number and Shields parameter) and relate them to measurable parameters in submarine systems: slope and grain-size. Minimum slope thresholds have been inferred for the formation of UMBs in natural systems (McCave, 2017), which relate to the minimum slope angle required for Froude-supercritical flow (Komar, 1971; Hand, 1974). We confirm here the existence of an additional maximum slope threshold (Kostic, 2011; Zhong et al., 2015), beyond which dune-scale bedforms will not migrate upstream, even under Froude supercritical conditions. This upper-threshold explains the lack of UMBs in steep

submarine gullies, compared to lower-angle submarine channels (e.g. Micallef and Mountjoy, 2011). If slopes are too low, or sediment is too coarse, the peak-Shields threshold (θ_{90}) will not be met, even if a turbidity current is stratified; hence UMBs do not form. However, if slopes are too steep, or sediment is too fine, high velocity gradients promote mixing, thus inhibiting stratification and restricting the formation of UMBs. We show here that there is a "sweet-spot" for the formation of UMBs in submarine channels, requiring a combination of previously hypothesized variables (Fig. 2). The combination of suitably steep slopes and grain-sizes is typically found in proximal and axial submarine systems, thus explaining the worldwide abundance of dune-scale UMBs in those natural submarine channels. However, typical down-channel decreases in grain size and slope are likely to explain the lack of dune-scale UMBs in the deep-sea (Symons et al., 2016).

3.6 Acknowledgements

This research was supported by ExxonMobil, National Oceanography Centre, NWO grant 864.13.006, and NERC grant NE/L009358/1.

Chapter 4: Frontal character of stratified turbidity currents with a denser basal layer

This chapter is co-authored by Dr Matthieu Cartigny, Dr Michael Clare, Dr Daniel Parsons, Dr Steve Simmons, Dr Dick Mastbergen, Dr Geeralt van den Ham, Dr Andre Koelewijn, Marco de Kleine, Prof Peter Talling, Dr Jim McElwaine, Jamie Hizzett, Sophie Hage and Maria Azpiroz.

I did the analysis of the bathymetry, ADCP and M3 data, and wrote the manuscript. Dr Matthieu Cartigny, Dr Michael Clare and Prof Peter Talling helped with discussing the results and reviewing the manuscript. Dr Dick Mastbergen provided the grain-size analysis. Sophie Hage, Dr Steve Simmons, and Maria Azpiroz helped constructing the acoustic inversion of the ADCP data. All co-authors but Sophie Hage, Peter Talling, Jim McElwaine and Steve Simmons were present at and helped during the experiment. Only co-authors Matthieu Cartigny, Michael Clare and Peter Talling had the chance to review the text in this chapter.

4.1 Abstract

Turbidity currents are subaqueous particle-laden density currents, and play a significant role in transporting sediment from continental shelves to the deep sea. Turbidity currents are powerful, and can be destructive to subsea infrastructure. The frontal part of turbidity currents is most destructive as it travels at the highest velocity. The anatomy of this frontal part of the turbidity current is still poorly understood due to a lack of high-resolution direct measurements. Here we present the first direct measurements of the frontal part of a turbidity current at an unprecedented spatial and temporal resolution. The observed turbidity current is, however, stratified and has a wedge-shaped front that hosts the fastest and densest part of the flow. This contrasts with the boubous and slow fronts observed in laboratory experiments of (unstratified) turbidity currents which have informed conceptual models. The observations are integrated with previous measurements to produce a conceptual model of the frontal structure of stratified turbidity currents. . Additionally, we compare this new conceptual model with the existing models of stratified powder-snow avalanches and stratified pyroclastic density currents. The frontal character of all these flows are similar in shape, velocity and density structure, even though powder-snow avalanches and pyroclastic density currents have much higher

absolute flow velocities and density contrasts. The similarities in structure between the three types of particulate density currents results from similar U_s/U^*-ratios.

4.2 Introduction

Turbidity currents pose a hazard to the ever expanding network of seafloor infrastructure that currently underpins telecommunication and energy supply. For example, the 1929 Grand Banks earthquake triggered a submarine landslide that transformed into a powerful seabed-hugging density flow (a turbidity current), carrying 200 km^3 of sediment, and traveling at up to 19m/s (Heezen and Ewing, 1952; Nisbet and Piper, 1998). This turbidity current broke over 20 seafloor telegraph cables that connected North America and Europe. Telecommunications cables now play a far more important role in our daily lives than in the 1920s. These cable networks now carry over 95% of global data traffic, which is the backbone of the internet, cloud data storage, and financial transactions (Carter et al., 2009). The search for oil and gas, and offshore renewable energy, has also led to an increase in valuable and strategic infrastructure on the seabed. Damage to this seabed infrastructure has serious economic and environmental impact (Barley, 1999; Carter et al., 2009). It is therefore important to understand the impact of turbidity currents on seafloor infrastructure, to mitigate risks (Bruschi et al., 2006b; Clare et al., 2015b). Despite the importance of quantification of the impacts of turbidity currents, measurements are sparse, as turbidity currents are notoriously difficult to monitor directly (Talling et al., 2012).

The few direct measurements available suggest that the front of the turbidity current is the most powerful, as it is the fastest and densest part of the flow (Xu et al., 2004; Khripounoff et al., 2012; Xu et al., 2012; Hughes Clarke, 2016; Azpiroz-Zabala et al., 2017). These first measurement also suggest that the front of turbidity currents is relatively thin compared to the trailing flow (Puig et al., 2014; Azpiroz-Zabala et al., 2017; Symons et al., 2017). Previous measurements have, however, not been able to measure velocities or sediment concentrations in the basal few metres of the flow, where the velocities and sediment concentrations are expected to reach their maximum values. Though limited in detail, the frontal structure of these turbidity currents resembles that of other stratified density currents such as powder-snow avalanches and pyroclastic density currents. Such similarity points to the importance of flow stratification on the frontal structure of these particulate density flows.

Both powder-snow avalanches and pyroclastic density currents display two end-member flow modes: (1) a homogenous, dilute and turbulent current with a bulbous and dilute front (Fig. 1A and C) (e.g. Voellmy, 1955; Simpson, 1987; Branney and Kokelaar, 2002; Kohler et al., 2014), and (2) a current that is internally stratified with a dense and wedge-shaped front (e.g. Simpson, 1987; Branney and Kokelaar, 2002; Sovilla et al., 2015; Breard et al., 2016) (Fig. 1B and D). Geologists have long inferred that turbidity currents could also be internally stratified (Kuenen and Migliorini, 1950; Dzulynski and Sanders, 1962; Kneller and Branney, 1995; Haughton et al., 2009). Denser basal layers in stratified turbidity currents have recently also been directly observed (Sumner and Paull, 2014; Hughes Clarke, 2016). However, the implications of stratification on the frontal structure the turbidity currents remains poorly constrained as the fastest and densest part of the basal layer has not previously been monitored.

In this contribution, we seek to directly measure the frontal structure of stratified turbidity currents, and then compare them to the structure of other particle-laden stratified density currents. We first analyse the frontal structure of a man-made turbidity current created by the discharge of dredged sediments in the Western Scheldt. The measurements from this flow are made by high-frequency (1200 kHz) current profilers and enable us for the first time to observe the basal and frontal part flow in detail. The observations show the shape, velocity and density structure of the turbidity current front. We then compare these observations with those previously presented in literature to produce a new conceptual model for the frontal structure of a stratified turbidity current. Finally, we compare the structure of these turbidity currents to that of snow avalanches and pyroclastic flows and derive generalised models for different density flow structures.

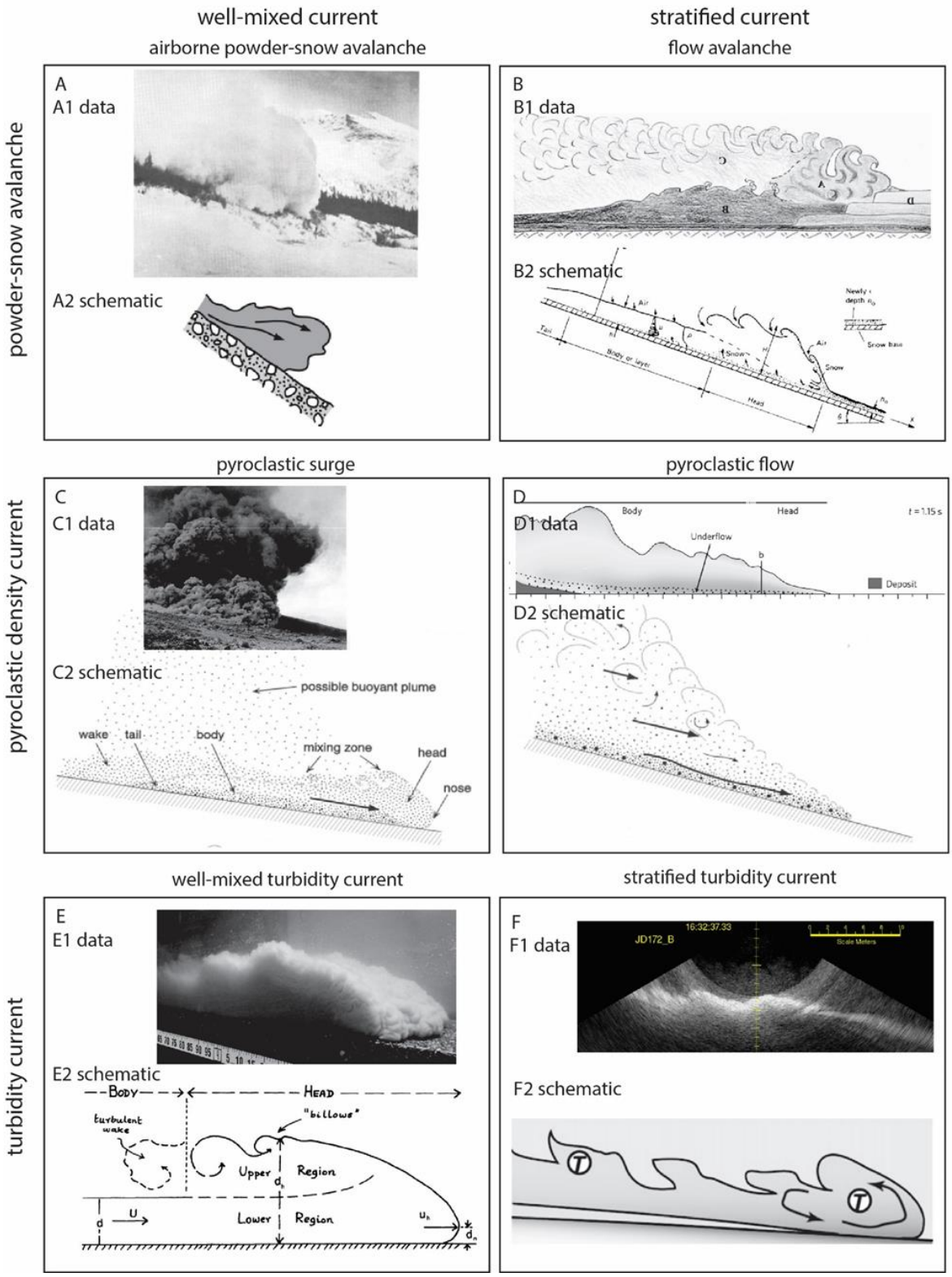
well-mixed current
airborne powder-snow avalanche
stratified current
flow avalanche
powder-snow avalanche
A
A1 data
A2 schematic
B
B1 data
B2 schematic
pyroclastic surge
pyroclastic flow
pyroclastic density current
C
C1 data
C2 schematic
possible buoyant plume
wake
tail
body
mixing zone
head
nose
D
D1 data
Body
Head
Underflow
Deposit
D2 schematic
well-mixed turbidity current
stratified turbidity current
turbidity current
E
E1 data
E2 schematic
BODY
HEAD
turbulent wake
"billows"
Upper
Region
Lower
Region
F
F1 data
JD172_B
F2 schematic

Figure 1: An array of available conceptual models and schematics on the characteristics of different types of particle-laden density currents. Left column shows dilute, homogenously mixed and fully turbulent currents. Right column shows currents that have internal density-stratification. Three different particle-laden density currents (powder-snow avalanches, pyroclastic density currents, and turbidity currents) are each divided into two end-members: (1) a dilute current and (2) a current with a denser basal layer. A1: photograph image of powder snow avalanche with thick front (Hopfinger, 1983), A2: conceptual image of a powder-snow avalanche (Hübl et al., 2002), B1: drawing a powder-snow avalanche with a dense basal layer based on RADAR data (Sovilla et al., 2015), B2: conceptual image of a flow avalanche (Simpson, 1999), C1: photograph of pyroclastic surge at St. Augustine Volcano (Maurice and Katia Kraft), C2: conceptual image of a pyroclastic surge (Branney and Kokelaar, 2002), D1: sketch of a stratified pyroclastic density current based on a laboratory experiment (Breard et al., 2016) D2 conceptual image of a pyroclastic flow (Branney and Kokelaar, 2002),E1: photo of a laboratory experiment of a dilute well-mixed turbidity current (Maurice Garcia). E2: conceptual image of turbidity current based on dilute lab experiment (Middleton, 1993), F1: direct observation of a stratified turbidity current at Squamish Delta (Hughes Clarke, 2016), F2 conceptual image of a high-density turbidity current, with denser basal layer, T is where the flow is turbulent (Haughton et al., 2009).

4.3 Methods

This study uses direct monitoring data of a man-made turbidity current of high spatial and temporal resolution. The turbidity current was generated by a dredger discharging sediment on a subaqueous slope. The dredger used here was part of an experiment to trigger a flow slide (Mastbergen et al., 2016). The turbidity current was monitored from a ship equipped with two different acoustic imaging instruments: (1) a 1200 kHz Acoustic Doppler current profiles (ADCP), and (2) a 500 kHz multibeam multimode sonar (M3). The experiment took place in the Western Scheldt Estuary, at the southern margin of a sandy shoal *de Plaat van Walsoorden* (Fig. 2), in The Netherlands, on 1 and 2 October 2014.

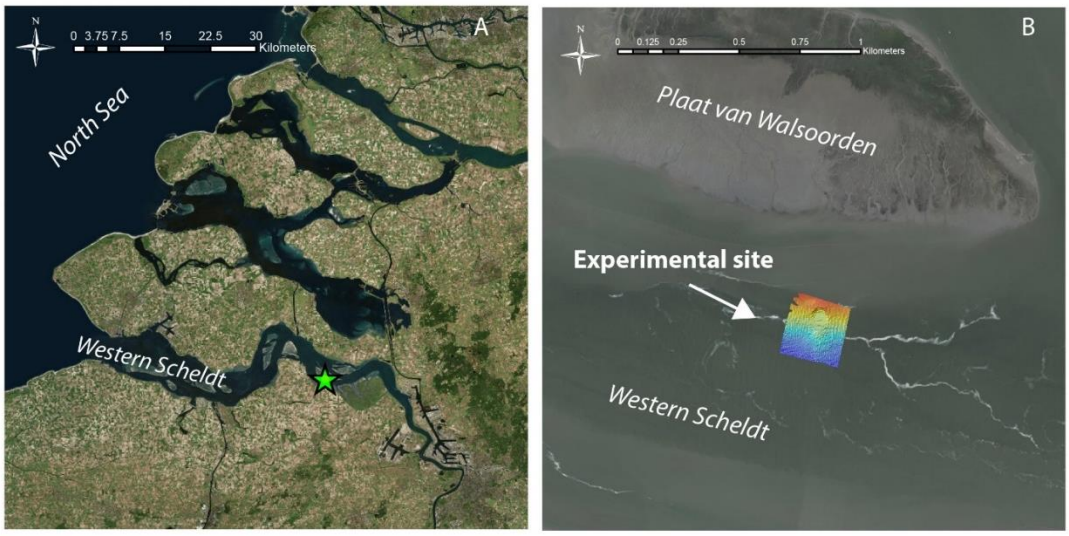

Figure 2: An overview of the location of the study area, in the Western Scheldt Estuary, at the southern margin of the Plaat van Walsoorden

4.3.1 Experimental setup

The dredger *Zeeland* discharged 325m³ of sediment through its bottom doors and thus created a turbidity current flowing downslope (Fig. 3, detailed map in Appendix 4.1). Monitoring ship *Geosurveyor XI (GEOXI)*, equipped with acoustic monitoring instruments, was located 50m south of *Zeeland*, in the path of the turbidity current (Fig. 3). The *Geosurveyor XI* (GEO XI) drifted north at 15cm/s while monitoring the turbidity current, and drifted over the lee-side of a bedform during this period. Analysis of geomorphological features in the study area, and a timetable of all bathymetric surveys and events is presented in appendix 4.

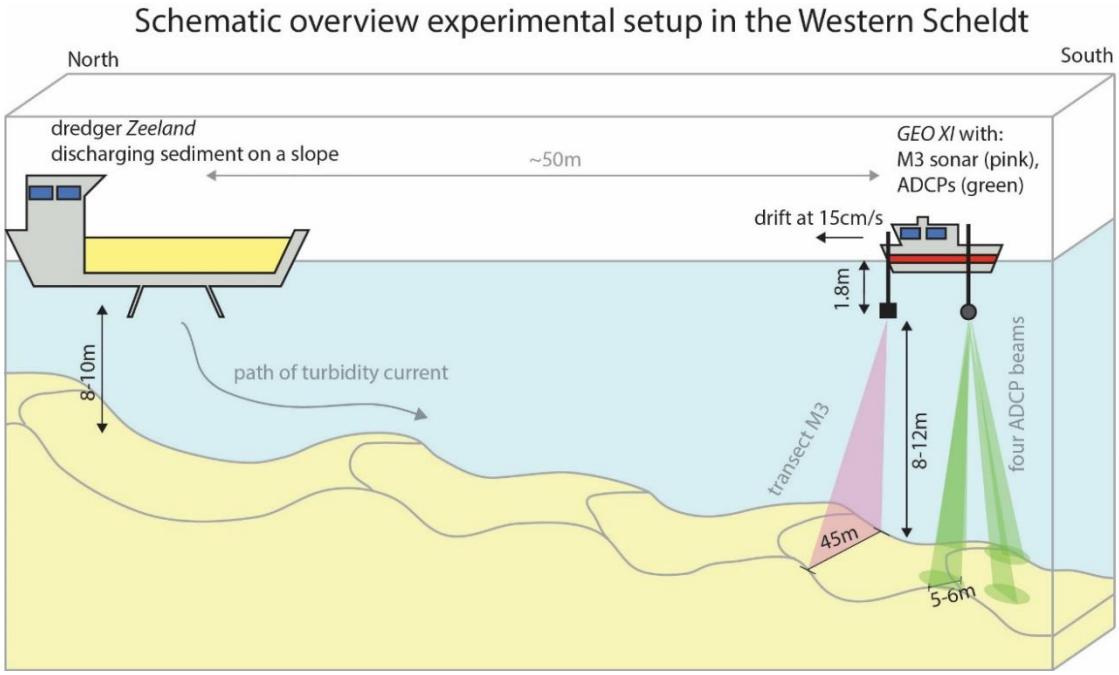

Figure 3: An overview of the experimental setup during the experiment. Dredger Zeeland is located upslope of the GEOXI when it releases sediment to create a turbidity current. The Geosurveyor XI (GEOXI) is equipped with several acoustic devices and monitors the turbidity current passing under the boat. A detailed plan view image is found in appendix 4.1

4.3.2 Acoustic imaging instruments

Flow measurements of the turbidity current were acquired using the following two instruments.

4.3.2.1 Acoustic Doppler Current Profiler (ADCP)

A 1200 kHz ADCP was attached to the *GEO XI* (table 1) by a pole, and is located 1.8m below the water surface. The ADCP's four beams each image a conical volume of the watercolumn, which is partitioned into vertical "bins" of 25cm (Fig. 3). These 25cm bins are of the same resolution as the data used in Hughes Clarke (2016), but of higher resolution than the often 100cm bins resulting from 300 kHz ADCPs often used for flow monitoring (e.g. Khripounoff et al., 2012; Azpiroz-Zabala et al., 2017). The ADCP provides a time-series of measurements every 3s, similar again to Hughes Clarke (2016) and Azpiroz-Zabala et al., (2017), but very different to the 1200s in Khripounoff et al., (2012). The ADCP used has a side-lobe interference distance of approximately 1m, which means data from the bottom metre could be unreliable. Velocity error analysis of this bottom 1m,

however, does not suggest the data is less valid than the data above the bottom 1m and thus is presented here, as for example also in Hughes Clarke (2016).

The ADCP measurements are used to reconstruct the velocity structure of the front of the turbidity current. The ADCP measures flow velocities in three principal directions: north, east and up, for all 25cm bins. A velocity vector is then calculated in the mean flow direction, which is also corrected for tidal currents (appendix 4.6).

This study also analyses the sediment distribution structure in the turbidity current using the acoustic impulse that is reflected back (backscatter). The backscatter intensity is a function of both the amount of sediment in the water column, and the grain-size of that sediment. Here we assume a set grainsize throughout the flow and link all backscatter variation directly to variations in sediment concentration using the *implicit iterative inversion method* (appendix 4.7). This method assumes that: (1) All acoustic energy reflected by a sediment grain is not attenuated by sediment on its way back from the reflection to the transceiver and (2) grain size does not vary within the flow, as in previous work (Azpiroz-Zabala et al., 2017; Simmons et al., 2017). The first assumption is reasonable for dilute flows but becomes more tenuous at higher sediment concentrations (near the bed). The second assumption is reasonable as the sediment in the estuary is characterised by a narrow grain grain-size distribution (d_{90}/d_{10}=1.6; Mastbergen, 2015). Additionally, the calculated sediment concentration are linearly proportional to an instrument-specific constant (k_t).Unfortunately, the instrument-specific constant (k_t) is unknown for our ADCP. Therefore only a relative sediment concentration is constructed, with ρ =1 being highest concentrations measured in the flow and ρ =0 being a sediment concentration of 0.

4.3.2.2 Multibeam Multimode Sonar (M3)

GEO XI was equipped with a M3 sonar (table 1), which was also mounted to a pole attached to the ship. The M3 creates backscatter images of the shape of the flow, every second. These M3 differs from the ADCP image as it has a series of 256 beams spread over a line source. These beams measure the backscatter over a sheet with a field of view that is 120˚ wide, 3˚ thick over a range of 25m. M3 images thus capture the evolution of the two-dimensional shape of the front of the turbidity current over time. Additionally, we have constructed a M3 time-

series by extracting the centre beam from each consecutive image. These time series can then be directly compared to the ADCP time series.

Table 1: Instrument specification of the instruments used in this study.

Instrument Name	Vessel	Configuration	Frequency	Spatial Resolution	Temporal Resolution	Field of view
Teledyne Acoustic Doppler Current Profiler (ADCP)	Geosurveyor XI	10m above the bed, Downward-looking profile	1224 kHz	Vertical: 25cm	3s	20˚
Kongsberg Multibeam MultiMode (M3) sonar	Geosurveyor XI	10m above the bed, Downward-looking transect	500 KHz	Vertical: 6cm	1s	3˚ x 120˚

4.4 Results

The aim of this study is to characterise the shape, velocity and density structure of the front of a stratified turbidity current. Measurements from the ADCP and M3 multibeam sonars are now presented individually. Finally, the two datasets are integrated to construct a detailed picture of the frontal structure of the stratified turbidity current.

4.4.1 Acoustic Doppler Current Profiler measurements

The distribution of the sediment concentrations resulting from the acoustic inversion are shown in Figure 4A. Relative sediment concentrations are the sediment concentration as a fraction of the highest measured sediment concentration in the turbidity current. Highest relative sediment concentrations (ρ=1) are found at basal part of the front of the turbidity current (Fig. 4A). A denser layer (ρ>0.8) is present at the near the bed, during the first 150s of the flow. Stratification is most pronounced in the frontal 25 seconds and then becomes more gradual during the later parts of the current, as indicated by a higher sediment concentration gradient in the front of the turbidity current (Fig. 5). The turbidity current thickens to <4 m during the first 50s, after which the

flow has a near constant thickness. The relative sediment concentrations decreases towards the top of the flow, and also towards the tail of the flow. The turbidity current appears to thin in the last 50s of its duration.

The overall velocity structure of the turbidity current as observed by the ADCP can be seen in Figure 4B-C. The turbidity current lasted approximately 200s. The maximum observed flow velocity is 1.2 m/s and occurred in the front of the turbidity current (Fig. 4B), near the bed (bottom 25cm). The average velocity in the turbidity current is 0.5 m/s. The water column just in front and on top of the flow is characterised by upward-directed velocities of 0.1 m/s. These upward velocities are followed by downward directed vertical velocities of an equal magnitude indicating the presence of large rolling vortices (Fig. 4C).

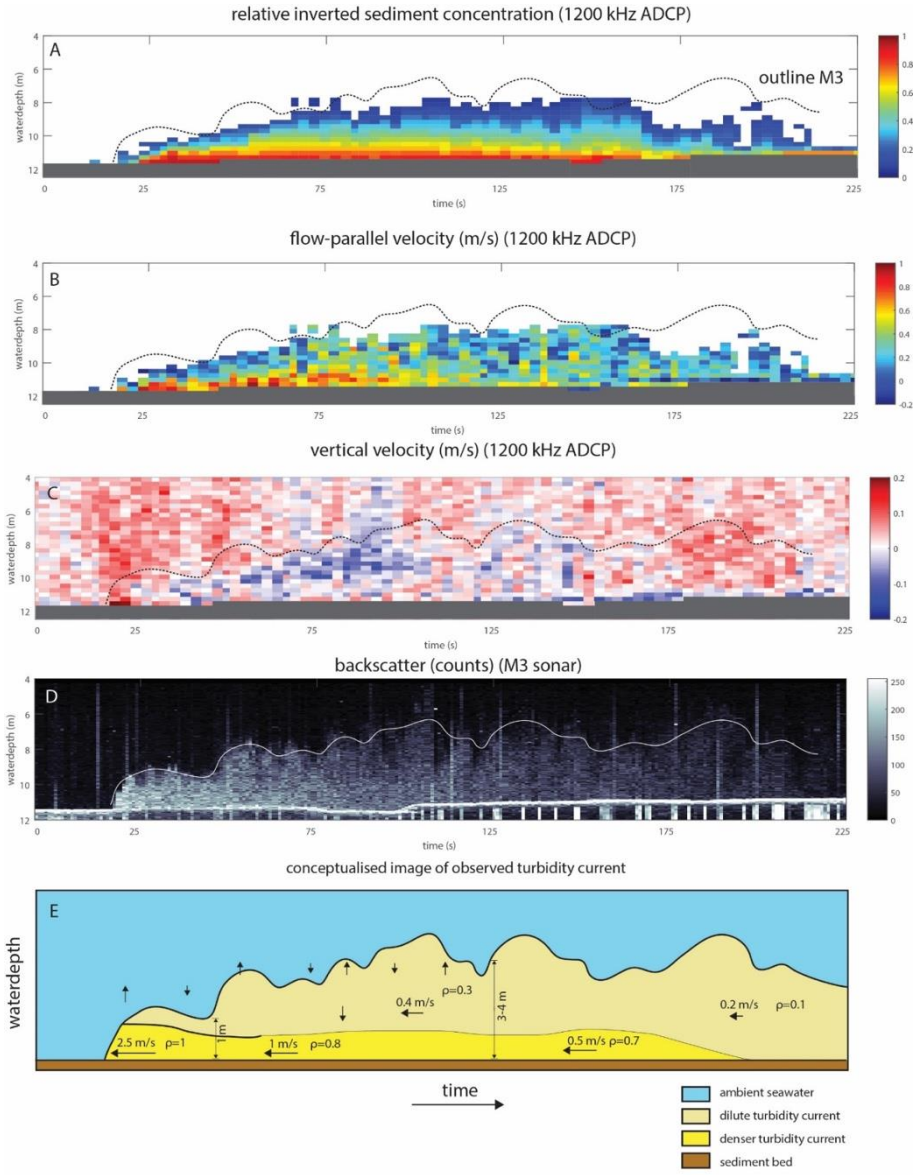

Figure 4: Time-series of measurements in the turbidity current. A: Acoustic inversion of the relative sediment concentration (1 is highest concentration

observed in the flow and 0 is no sediment). B: The flow-parallel velocity. C: Vertical velocity in the water column, where positive (red) is up and negative is down (blue) D: Time-series of backscatter through the middle beam of the M3 transect, the acoustic beam goes over a bedform at 75-125s. E: A schematic interpretation of the character of the turbidity current as observed in panels A-D.

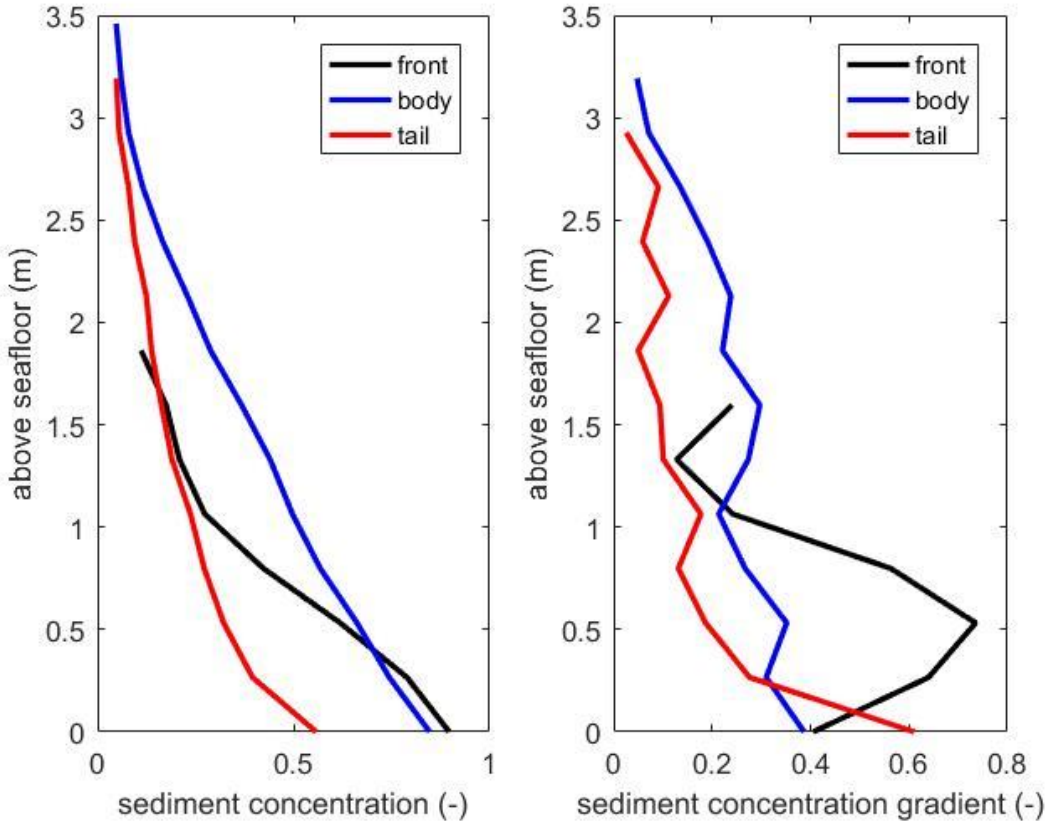

Figure 5: sediment concentration and sediment concentration gradients at the front (first 25s), body (second 75s) and tail (last 50s) of the observed turbidity current.

4.4.2 Multibeam multimode sonar (M3)

The backscatter intensity time series of the M3 shows that the front of the turbidity currents is relatively thin compared to the body (Fig. 4D). The front has highest sediment concentrations, as backscatter intensity is higher (assuming uniform grain-size distribution). The sediment concentration in the turbidity current is at its highest in a near-bed layer. The sediment concentration decreases gradually over time, until it reaches background backscatter levels (after 200s in Fig. 4D). Finally, we compare the time series measurements with the instantaneous transect images (Fig. 5). The M3 transect image shows that the turbidity current has a more wedge-shaped front than outline produced in the

time series. Kelvin-Helmholtz (K-H) instabilities are visible on the top of the current (Fig. 6). The consecutive transect images enable us to measure a front velocity of 2.5 m/s, which is doubles the highest velocity seen in the ADCP time series.

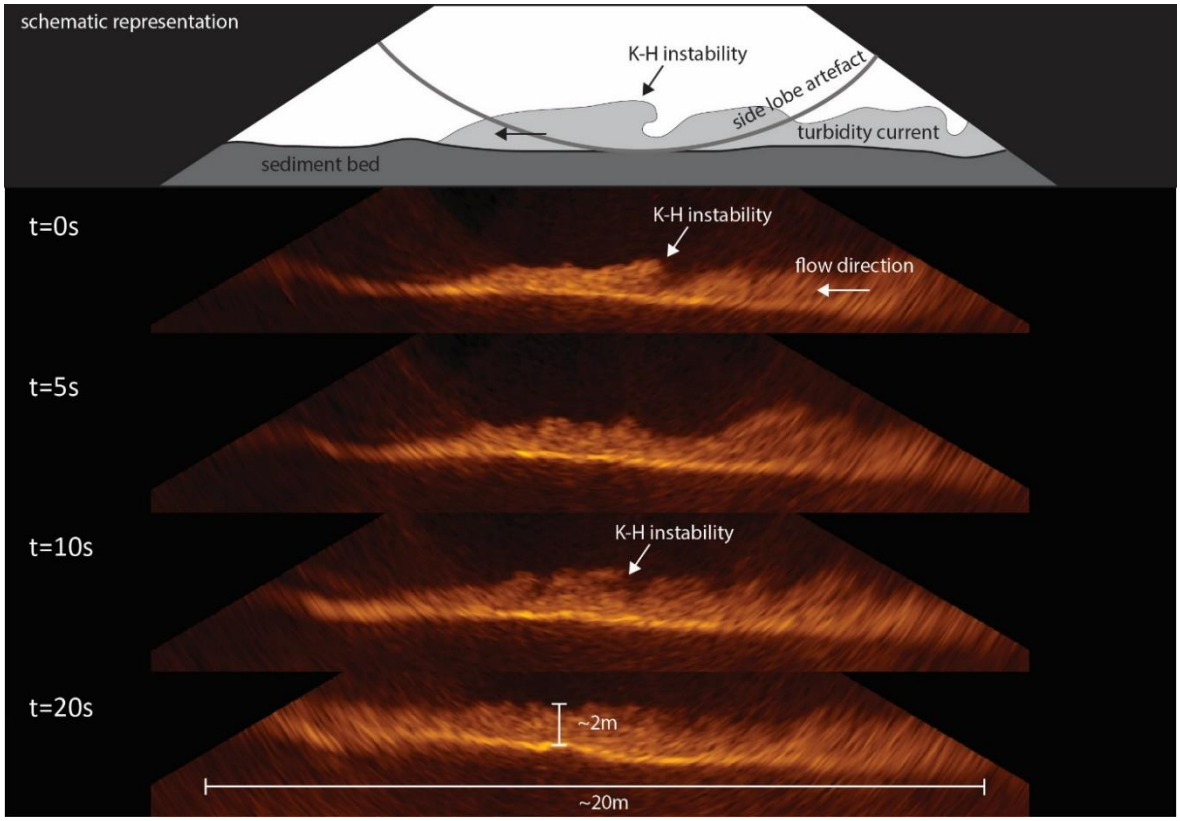

Figure 6: Four snapshot flow-transect images taken at 5s interval, and a schematic representation of the turbidity current as observed through the 500 kHz Multimode-multibeam sonar (M3). The images are downward looking transects of the turbidity current that flows from right to left. K-H (Kelvin Helmholtz) instabilities are visible at the top of the turbidity current.

In short, the structure of this stratified turbidity current can be summarised as (Fig. 4E):

- The front of the turbidity current is wedge-shaped (Fig. 6).
- The front of the turbidity current is the fastest-moving part of the flow (Fig. 4B).
- The front of the turbidity current is the densest part of the flow (Fig. 4A).
- The front of the turbidity current is most strongly stratified; it has a denser basal layer overlain by a more dilute area (Fig. 4A, 5). Further back, the stratification becomes less pronounced.
- Kelvin-Helmholtz instabilities are present at the top of the turbidity current (Fig. 6).

4.5 Discussion

A comprehensive new conceptual model of the frontal structure of a stratified turbidity current is presented based on data presented here and previously published data. This new conceptual model is then compared with models of the other density currents with a denser basal layer such as powder-snow avalanches and pyroclastic density currents.

4.5.1 Frontal structure of stratified turbidity currents – a conceptual model

A new conceptual model of a stratified turbidity current is constructed based on the direct measurement of this study and of other direct monitoring studies (Fig. 7). The new model is characterised by a wedge-shaped front of the turbidity current (Puig et al., 2014; Sumner and Paull, 2014; Azpiroz-Zabala et al., 2017; Symons et al., 2017; Fig. 5 this study). The front is the fastest (Xu et al., 2004; Khripounoff et al., 2012; Xu et al., 2012; Hughes Clarke, 2016; Azpiroz-Zabala et al., 2017; Symons et al., 2017; Fig. 4 this study) and densest (Symons et al., 2017; Fig. 4 this study) part of the current, and displaces ambient water upwards (Fig. 4 this study). The current is stratified (Sumner and Paull, 2014; Hughes Clarke, 2016; Azpiroz-Zabala et al., 2017; Symons et al., 2017; Fig. 4, 5 and 6 this study): a denser layer is overlain by a more dilute layer, there may be (roll-waves) instabilities on the interface between those two layers(Sumner and Paull, 2014; Hughes Clarke, 2016). Kelvin-Helmholtz-instabilities are present on at the top of the flow(Hughes Clarke, 2016; Fig. 6 this study).

The directly measured turbidity currents used to construct the conceptual model are different in scale, they range from turbidity current of many tens of metres thick and lasting for days (Azpiroz-Zabala et al., 2017) to turbidity currents that are a few metres thick and last several minutes (this study; Hughes Clarke, 2016), and anything in between. Despite the differences of scale the observations are surprisingly coherent, and thus lead to a comprehensive model that appear applicable over a wide range of settings.

The new model of stratified turbidity currents (Fig. 7) differs from the previous models available in the literature (e.g. Fig. 1F2).). These literature models are

strongly based on experimental studies where the flow front is bulbous and dilute (e.g. Postma et al., 1988; Shanmugam, 2000; Haughton et al., 2009). Rather, direct observations show the front of stratified turbidity current is wedge-shaped and the densest part of the flow (Fig. 6, 7, 8F), similar to that of stratified powder-snow avalanches and pyroclastic density currents (Fig. 8B and D). The front of the stratified turbidity currents is the fastest and densest part of the flow (Xu et al., 2004; Khripounoff et al., 2012; Xu et al., 2012; Hughes Clarke, 2016; Azpiroz-Zabala et al., 2017; Symons et al., 2017), and also the densest. The front of the current also clearly displaces ambient water upwards as observed by the vertical velocity measurements in this study. Kelvin-Helmholtz instabilities are clearly present on the top-interface of the turbidity current, but internal instabilities are also observed in Sumner and Paull (2014) and Hughes Clarke (2016) studies.

The new model implies that the shape of the turbidity current front is directly linked to flow stratification. A wedge-shaped front infers a stratified dense turbidity current, and a bulbous-shaped front infers a homogenously mixed turbidity current. Furthermore, from an applied geohazard risk point of view, the front of a stratified turbidity current poses the largest hazard. It has the highest flow velocities and densities, and will therefore generate the highest impact forces on infrastructure. The front of the turbidity current is, however, relatively short lived (minute in small systems, such as Squamish, to hours in larger systems, such as Monterey Canyon or Congo Canyon).

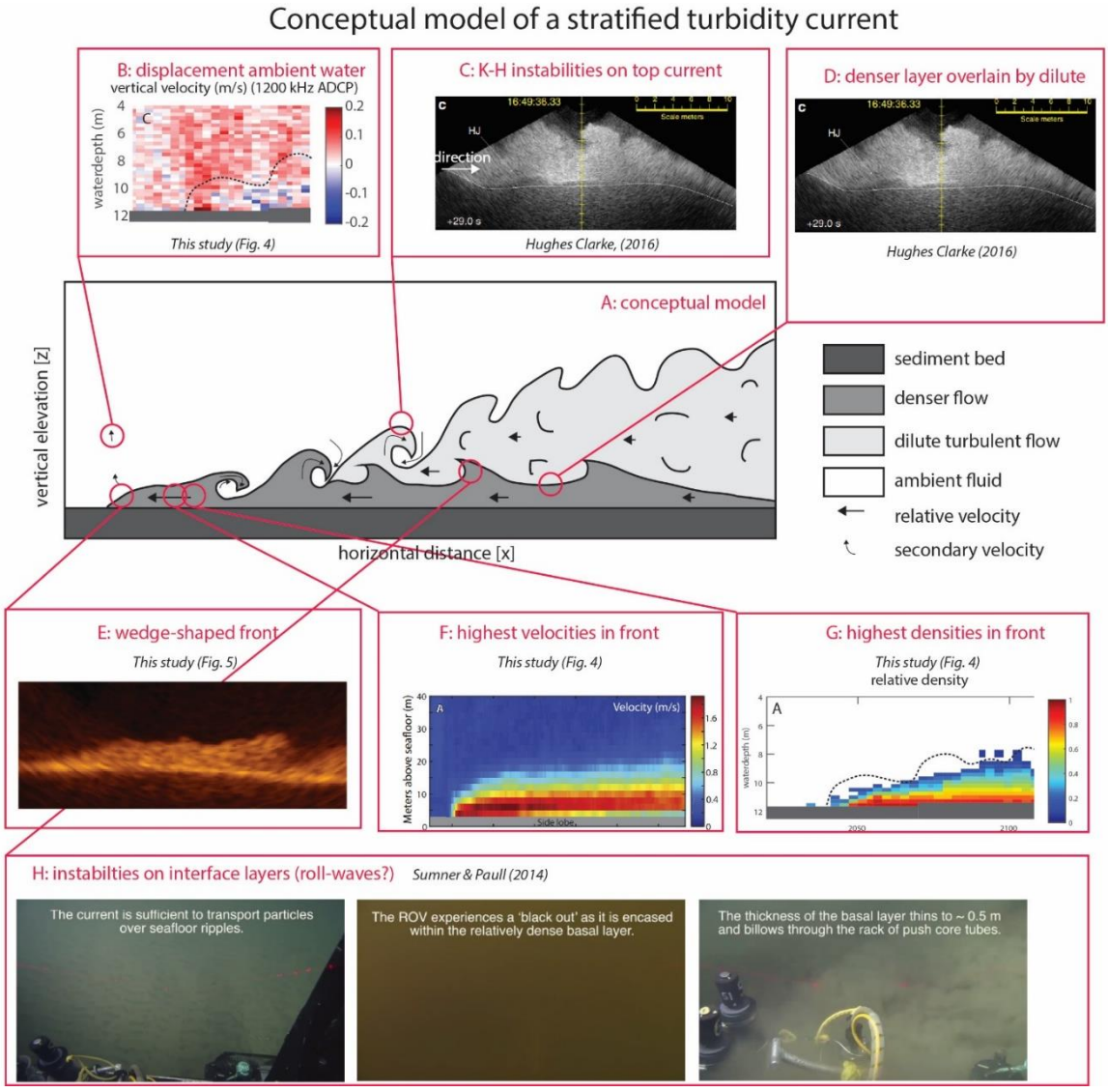

Figure 7: Conceptual model of a turbidity current with a denser basal layer. The model is based on the direct measurement of the turbidity current in this study and direct observations of turbidity currents described in literature.

4.5.2 Comparing stratified turbidity currents with other stratified particle-laden density currents

Comparing stratified turbidity currents with stratified powder-snow avalanches and stratified pyroclastic density currents is reasonable as all three flows belong to the family of particle-laden density currents. Non-stratified and dilute turbidity currents behave in many ways similar to dilute (airborne) powder-snow avalanches (e.g. Simpson, 1982; Meiburg et al., 2012) and (dilute) pyroclastic surges (e.g. Simpson, 1982) (Fig. 1A,C and E). The perceived difference flow structure of stratified turbidity currents relative to stratified powder-snow

avalanches stratified pyroclastic density currents is thus peculiar (Fig. 1B, D and E).

Table 2: An overview of the key similarities and differences of the front of three different types of density currents with a denser basal layer. Superscripts refer to: 1 (Simpson, 1999), 2 (Sovilla et al., 2015), 3 (Branney and Kokelaar, 2002), 4 (This study), 5 (Puig et al., 2014), 6 (Sumner and Paull, 2014), 7 (Azpiroz-Zabala et al., 2017), 8 (Symons et al., 2017),9 (Breard et al., 2016), 10 (Hughes Clarke, 2016), 11 (Khripounoff et al., 2012), 12 (Xu et al., 2004), 13 (Xu et al., 2012), 14 (Kohler et al., 2018), 15 (Cartigny et al., 2013), 16 (Turnbull and McElwaine, 2007), 17 (Issler, 2003), 18 (Dade and Huppert, 1996), 19 (Xu et al., 2014). 20 (Issler, 1998). 21 assumes quartz grains of range 100μm-2500μm in air 22 assumes quartz grains of range 100μm-2500μm in water. 23. Assuming shear velocity is proportional to typical mean flow velocity (5-10%).

	Stratified powder-snow avalanche (flow avalanche)	**Stratified pyroclastic density current (pyroclastic flow)**	**Stratified turbidity current**
Front shape	Wedge-shape[1,2]	Wedge-shape[3]	Wedge-shape[4,5,6,7,8]
Peak velocities	At front[2]	At front[9]	At front[4,8,10,11,12,13]
Peak densities	Just behind front[2]	At front[3]	At front[4]
Instabilities	K-H instabilities, roll-waves[2,14]	More billowing appearance / lofting[3]	K-H instabilities[4,6,10] and roll-waves[6,15]?
Absolute velocity	10-100 m/s[16]	10-200 m/s[3]	< 1-7 m/s[4,6,8,10,11,12,13]
Current density contrast $\rho_{current}$ / $\rho_{ambient}$	20-50[17]	5-50[9,18]	1.0004-1.1[6,10,19]
Current density difference $\rho_{current}$ - $\rho_{ambient}$	20-50kg/m^3	5-50 kg/m^3	0.4-100kg/m^3
Settling velocity (u_s)	0.5-2 m/s[20]	0.05-1.8m/s[21]	0.001-0.2 m/s[22]
Shear velocity estimate (U*)	0.5-10 m/s[23]	0.5-20m/s[23]	0.05-0.7m/s[23]
U_s/U*	0.05-4 , mean: 0.2	0.0025-3.6: mean 0.1	0.0014-40 mean: 0.3
Other	"Erupting" front[2]	Buoyant hot gasses[3], intermediate layer[9]	

Table 2 compares the direct observations of stratified turbidity currents with observation of powder-snow avalanches and pyroclastic currents. The shape of the front, density structure and velocity structure are similar in the three density currents (table 2; Fig. 8 B, D and E). This similarity suggests that the three stratified flows are controlled by similar flow processes. Granular flow is present at the base of flow avalanches (Gauer et al., 2008; Louge et al., 2011; Kohler et al., 2018), and at the base of pyroclastic flows (Branney and Kokelaar, 2002; Breard et al., 2016). It could therefore be inferred that granular flow processes

also play a key role at the base of stratified turbidity currents. Additionally, granular flow has previously been proposed to play a role in stratified turbidity currents (e.g. Lowe, 1982; Kneller and Branney, 1995; Meiburg et al., 2012). (e.g. Lowe, 1982; Kneller and Branney, 1995; Meiburg et al., 2012). The overall anatomy of a stratified turbidity current is still poorly constrained by both experimental or numerical studies due to scaling issues and a lack of understanding how denser basal layers interact with dilute layers, respectively (Cartigny et al., 2013).

The observations shows that the denser basal layer in stratified turbidity currents is faster than the overlying cloud. The basal layer is thus not driven by the overlaying cloud. This is an important distinction as this makes these basal layers different from previously proposed *traction carpets* (e.g. Lowe, 1982; Hiscott, 1994; Sohn and Hiscott, 1995), but and more like a modified grain-flow (Lowe, 1976; Cartigny et al., 2013).

They key difference between the three particulate densities currents is the absolute velocity (Table 2). The velocity is related to the different fluids; water for turbidity currents and air for powder-snow avalanches and pyroclastic density currents. The differences in ambient fluid control the density contrast as well as the density difference. The current *density contrast* ($\rho_{current} / \rho_{ambient}$) in subaerial flows such as pyroclastic density current or powder-snow avalanche is much more than that in subaqueous flows such as turbidity current (Table 2). In contrast, the current *density difference* ($\rho_{current} - \rho_{ambient}$) is similar between all three density currents. The similarity in driving forces between the different flows implies that the difference in resisting (drag) force is the main control on the large difference in flow velocities (Table 2).

All three density currents display stratified and mixed modes, despite the difference in absolute flow velocity. Particulate density flows are unstratified if the particle settling velocity (U_s) is low relative to how fast particles to mix due to turbulence, for which U*, the shear velocity, is a proxy. Particles in powder-snow avalanches and pyroclastic density currents settle ~10 times faster than the sediment in a turbidity currents (Table 2), because of the low viscosity of air relative to water. Yet, all three currents have similar U_s/U^* ratios (Table 2). The similar ratios are produced due to the much higher velocities and shear velocities in pyroclastic density currents and power-snow avalanches. All three types of currents can thus potentially be stratified depending on local conditions, despite their differences in absolute flow velocity and particle fall velocity.

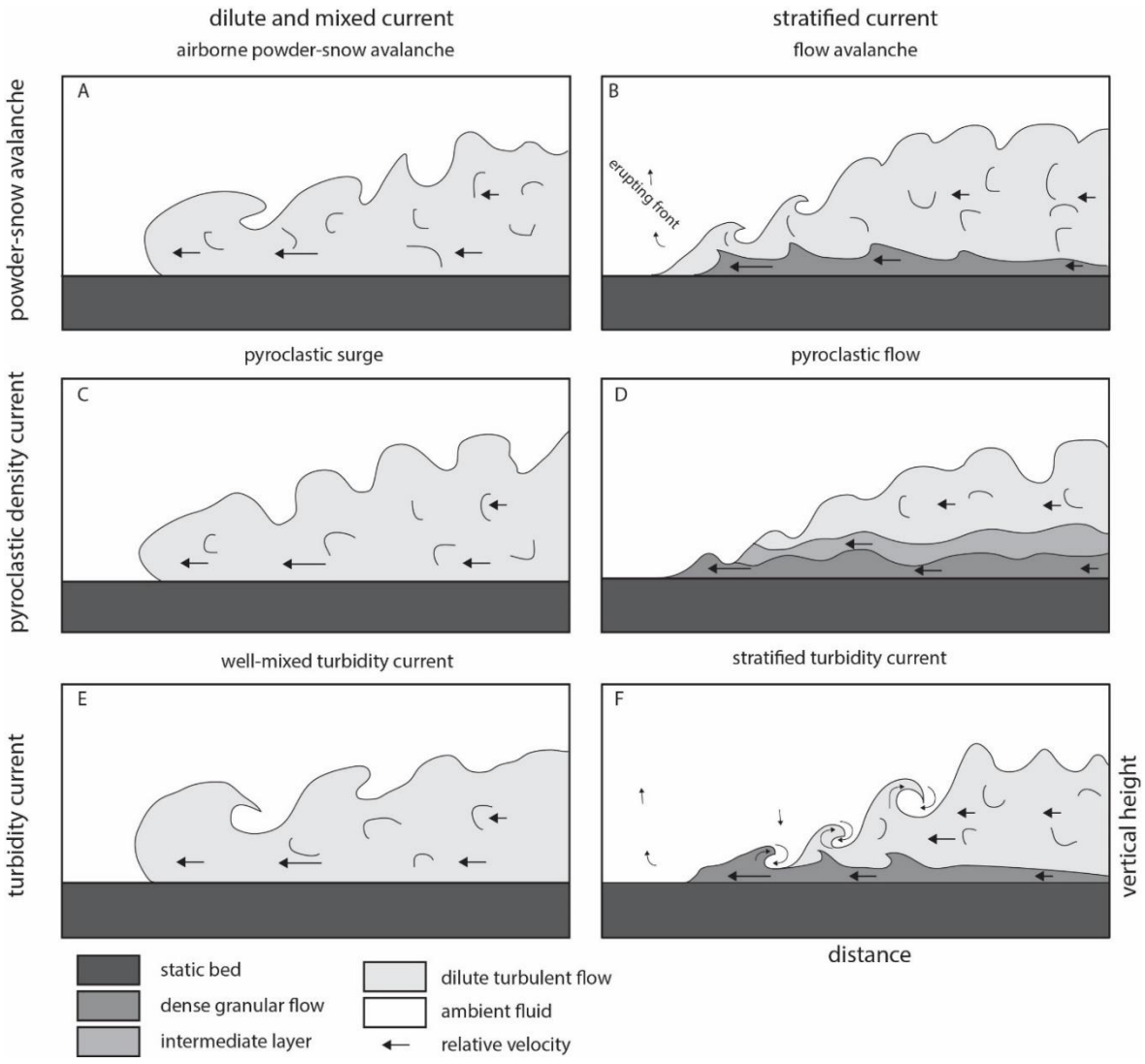

Figure 8: schematic conceptual models of different particle-laden density currents. The three groups of density currents are divided into two flow regimes well-mixed (first column) and stratified (second column). A: airborne powder-snow avalanche, based on (Voellmy, 1955a; Simpson, 1999). B: a flow (denser) avalanche, based on (Hopfinger, 1983; Simpson, 1999; Gauer et al., 2008; Sovilla et al., 2015). C: a pyroclastic surge, based on (Wohletz and Sheridan, 1979; Branney and Kokelaar, 2002). D: a pyroclastic flow based on (Branney and Kokelaar, 2002; Breard et al., 2016). E: A dilute turbidity current based on (Allen, 1985; Middleton, 1993). F: the new conceptual model of the front of a stratified turbidity current (taken from Fig. 6)

4.6 Conclusions

Turbidity currents are powerful and can be destructive to seafloor infrastructure (Carter et al., 2009) and the devices monitoring them directly (Paull et al., 2010; Lintern et al., 2016). Though the front of the turbidity current has most impact, it is poorly understood due to limited resolution in previous direct monitoring studies. This study firstly aimed to characterise the front of stratified turbidity currents. Secondly, the frontal character is compared with that of stratified powder-snow avalanches and pyroclastic density currents. The front of stratified turbidity currents differs in structure from that of a homogenous dilute turbidity current (two end members), just as homogeneous and stratified powder-snow avalanches and pyroclastic density currents display a different frontal character. The front of stratified turbidity currents is wedge-shaped, is the fastest part of the flow, and the densest part of the flow. The frontal structure of a stratified turbidity current is similar to stratified powder-snow avalanches and pyroclastic density currents. The similarities in frontal structure point to the importance of granular flow processes at the base of stratified turbidity currents. Absolute velocities of turbidity currents are an order of magnitude lower than those of powder-snow avalanches and pyroclastic density currents, as a turbidity current experiences more resisting (drag) forces. Particle settling velocities are also 10 times lower in turbidity currents, giving all three flows a similar U_s/U^* ratio. The similar U_s/U^* means all three particulate density currents can be stratified or unstratified depending on local conditions.

4.7 Acknowledgements

The field monitoring of the turbidity current in this study was part of a flow-slide experiment (*Validatie-experiment zettingsvloeiing)* organised by Stichting IJkdijk (now FloodControl IJkdijk) and Deltares, it was funded by the Ministry of Economic Affairs of the Netherlands, STOWA and Rijkswaterstaat. Furthermore, the University of Southampton and ExxonMobil contributed funded the lead author. The crews of *Zeeland, Geosurveyor XI, Geosurveyor IV and Enschede* have worked around the clock to make this study possible, and are greatly acknowledged for their efforts.

Chapter 5: Conclusion and future work

5.1 Conclusions

The overall aim of my thesis is to characterise geophysical flows that create upstream-migrating bedforms. Upstream-migrating bedforms form in a large range of settings on earth (and on other planets). The different chapters relate to upstream-migrating bedforms formed in different settings. In chapter two I explain the mechanics of cyclic steps in a fluvial setting, and their deposits. In chapter three I determine the formative controls on dune-scale upstream-migrating bedforms formed by turbidity currents in submarine channels. In chapter four I continue the focus on a turbidity current that formed upstream-migrating bedforms. I characterise the frontal character of this turbidity current and compare it to that of powder-snow avalanches and pyroclastic density currents, which are also known to be able to form upstream-migrating bedforms.

There is not one simple condition that characterises the geophysical flows that form upstream-migrating bedforms the specific characters of the flows are described in the paragraphs below. However, common elements to the geophysical flows that create upstream-migrating bedforms are: (1) these flows are in a Froude supercritical flow regime, (2) shear stresses on the bed are high suspended sediment transport is abundant, and (3) in the case of particulate density currents the flows often display a form of internal density stratification.

5.1.1 Mechanics and depositional character of cyclic steps

In chapter two I posed two questions: *(1) what are the mechanics of fluvial cyclic steps?* And (*2) what is the corresponding depositional signature of these cyclic steps?* A depth-resolved numerical model is used to answer these questions.

The mechanics of the simulated fluvial cyclic steps generally conform to existing conceptual models; there is supercritical flow over the lee side of the bedform and subcritical flow over the stoss side of the bedform. The simulations have, however, also led to new observations. For example, the modelling showed that the hydraulic jump itself is erosional. This contrasts previous models that link the abrupt decrease in velocity associated with a hydraulic jump to deposition.

Furthermore, the modelling shows that the hydraulic jump is only present 90% of the time, the remaining 10% the flow is supercritical throughout. When the flow is supercritical throughout the amplitude of the cyclic steps increase. This increase in amplitude then leads to the formation of a new hydraulic jump.

The results also show that the depositional signature of cyclic steps changes with the rate of aggradation. At high rates of aggradation a series of upstream dipping backsets form, bound upstream and downstream by an erosion surface. At low rates of aggradation, cyclic steps result in an amalgamation of concave-up erosion surfaces. Upstream and downstream-dipping laminations form lenticular bodies directly overlying the erosion surfaces. Additionally, the depositional signature is strongly controlled by the transient behaviour of the hydraulic jumps. The absence of a hydraulic jump creates the deepest troughs. The deposits in the deepest troughs are all that is preserved of these bedforms at low rates of aggradation. Furthermore, the presence of a hydraulic jump causes shear stress variations result in laminations of distinct grain-size.

5.1.2 Formative controls on dune-scale upstream-migrating bedforms in submarine channels

In chapter three I posed the question*: what are the formative controls on dune-scale upstream-migrating bedforms in submarine channels?* There were three hypothesised formative controls that may play a role: Froude supercriticality, density stratification and erosive capacity of the turbidity current. I tested the effect of these factors in a series of numerical simulations, and quantified the three factors with three dimensionless numbers: Froude number, gradient Richardson number and Shields number. The modelling shows that all three factor play a role in the formation of dune-scale upstream migrating bedforms.

All turbidity currents that generated upstream-migrating bedforms were supercritical, though not all supercritical turbidity currents create upstream-migrating bedforms. Only stratified turbidity currents created upstream-migrating bedforms, though again not all of them did. Finally, a peak Shields threshold is required for a stratified supercritical turbidity current to produce upstream-migrating bedforms. The modelling indicated that the peak Shield threshold was reached due to variations in discharge and velocity structure in the bottom of the flow. The discharge variations are linked to instabilities within stratified flows, and can be either roll-waves or downward propagations of Kelvin-Helmholtz instabilities. The three formative controls can be related back to parameters

readily available in modern submarine systems: slope and grain-size. With a slope too steep, or with sediment too fine, the turbidity current mixes well and does not become stratified, this prevents the formation of upstream-migrating bedforms. On slopes too gentle, or with sediment too coarse, the local peak Shields number does not exceed the threshold value and upstream-migrating bedforms do not form. There is thus a "sweet spot" at which dune-scale upstream-migrating bedforms are formed. It explains the common occurrence of dune-scale upstream-migrating bedforms but also their local absence.

5.1.3 The frontal character of turbidity currents with a denser layer in relation to other density currents

In chapter four of my thesis I ask the questions*: (1) what is the frontal character of stratified turbidity currents?* and *(2) how does the frontal character compare to that of other stratified particle-laden density currents?* Here I used direct measurements of a turbidity current to answers these questions.

The direct measurements revealed that a stratified turbidity current has a different frontal character than the typical frontal structure of a homogeneously mixed turbidity current. Where an unstratified and dilute turbidity current has a bulge-shaped front, the stratified turbidity currents have a wedge-shaped front. This front hosts the fastest velocities and is associated with the highest sediment concentrations. Just behind the wedge-shaped front the stratified turbidity current split into a denser basal flow layer that is overlain by a more dilute layer. The dilute layer is characterised by Kelvin-Helmholtz instabilities that mix ambient fluid into the flow. Additional instabilities are seen to form in between the basal dense layer and the dilute top layer. These instabilities are tentatively interpreted as roll waves due to their characteristics downstream migration and breaking-wave-like appearance.

A turbidity current is a particle-laden density current, similar to a pyroclastic density current or powder-snow avalanche. The direct observations of the stratified turbidity current show that its structure is similar to that of a pyroclastic density current of a powder-snow avalanche. In general, the main difference between subaqueous flows (e.g. turbidity currents) and subaerial flows (e.g. powder-snow avalanches and pyroclastic density currents) is their front velocity. Subaerial flows have frontal velocities that are an order of magnitude larger than those of subaqueous flows. This velocity difference is likely caused by a difference in density of the ambient fluid (air versus water). The similarity in

frontal character point to the importance of grain-to-grain interactions at the base of a turbidity current, similar to the grain-to-grain interactions that are known to occur at the base of pyroclastic currents and powder-snow avalanches.

5.2 Future work

Based on the three research chapters in this thesis I will now highlight three areas of future research.

5.2.1 Numerically generated deposits

In chapter 2 I have numerically created bedforms. It is thus possible to do the same thing for different flow conditions, and in different settings. The method allows linking flow dynamics to morphology and depositional product. Forward numerical modelling can help confident interpretation of paleo-environment from deposits. Furthermore, forward modelling techniques, may, in the future be implemented in petroleum exploration and reservoir modelling (Pyrcz et al., 2014; Vellinga et al., 2016). A practical application could, for instance, be the use of forward modelling to construct bespoke training images to specific settings for geostatistical modelling. In order to make forward modelling on a metre-scale the modelling would have to become truly three-dimensional. A question related to chapter 2 that interests me is: what does the deposit of a (fluvial) cyclic step look like in three dimensions?

5.2.2 Numerical modelling of turbidity currents and deposits

In chapter 3 I numerically simulated turbidity currents. There are still limitations to the forward modelling approach, especially in relation to turbidity currents: one can only numerically model processes that are understood. For example: it is not yet clear how high-density turbidity currents work, is there a traction carpet at the base, or is there a grain-flow, what are the mechanism to keep sediment in suspension, and what do the concentration, velocity and turbulence profile look like near the base of the flow? (Hiscott, 1994b; Sohn and Hiscott, 1995; Fick et al., 2015) The effect of sediment concentration and clay content on rheology and turbulence is not fully understood (Baas et al., 2016), and what implications does this have for *hybrid flows* (Haughton et al., 2009), and then, how are these flows coupled. To confidently model high-density flows and cohesive flows, such questions the above questions need to be answered.

More specific scientific questions related to turbidity currents I am interested in are:

- What is the depositional signature of dune-scale upstream-migrating bedforms formed by turbidity currents?
- But also, how do other morphologies and deposits that are formed by turbidity currents relate to flow characteristics? Can channel inception, levee formation and lobe thickness be predicted based on flow character? And inversely, can these depositional features be related to specific flow characteristics?

5.2.3 How is sediment transported at the base of a turbidity current?

In chapter 4 of my thesis I raise the question whether similarities in flow morphology of turbidity currents compared other particle-laden density currents are caused by similarities in process. I inferred the similarity in the mechanism of suspension of stratified particulate density currents (turbidity current, powder-snow avalanches and pyroclastic density currents) on the basis of frontal shape. The inference I made essentially relates back to how sediment is transported at the base of turbidity currents, which is still poorly understood. Detailed measurements near the base of turbidity current, at higher spatiotemporal resolution than the data I had would be needed to answer how sediment is transported at the base of turbidity currents. Important parameters to measure would be for example sediment concentration and rheology.

Appendices

A.1 – Introduction to appendices

The numbering of the appendices conforms to the sequence of the chapter to which the appendices relate: A.2 relates to the first chapter that requires an appendix: chapter 2, A.3 relates to chapter 3, and A.4 to chapter 4.

A.1.1 Glossary

Aggradation: vertical build-up of a sedimentary sequence (i.e. more sediment is deposited than eroded)

Antidune: a type of bedform formed under supercritical flow. Antidunes are formed by a flow with a train of free-surface waves. The free-surface waves distribute sediment in a dune-like pattern. Antidunes typically move upstream but can move downstream too.

Capacity (of a flow): refers to the capacity of that flow to keep sediment in suspension trough turbulence.

Competency (of a flow): refers to the competency of a flow to entrain (pick up) sediment from the bed trough shear stress exerted on the bed.

Cyclic step: a type of bedform formed under Froude supercritical flow conditions. A cyclic step is formed by a flow that has a series of upstream migrating hydraulic jumps. The lee side of the bedform is overlain by supercritical flow and erosive, the stoss side is overlain by subcritical flow and depositional. The bedform migrates upstream, however, sediment moves downstream.

Hindered settling: As sediment settles downwards a similar volume of water is displaced upwards, the upwards movement of this water hinders the downwards motion of settling sediment and is called hindered settling.

Jökulhlaup: (literally "glacial run") is a type of glacial outburst flood

PDC: pyroclastic density current

PSA: Powder-snow avalanche

Roller: A type of coherent flow structure on a mesoscopic to macroscopic scale. The water “rolls” around (i.e. changes direction 180 degrees and back).

Sediment discharge: The amount of sediment discharged (in a channel) either as mass or volume per time unit.

Sediment entrainment flux: The volume of sediment entrained (i.e. going from the bed into the flow) in a certain area over a certain time. [m/s]

Sediment entrainment mass-flux: The mass of sediment entrained (i.e. going from the bed into the flow) in a certain area over a certain time. [$kg/m^2/s$]

Sediment settling mass-flux: The volume of sediment settling (i.e. going from the flow to the bed) in a certain area over a certain time. [m/s]

Sediment settling mass-flux: The mass of sediment settling (i.e. going from the flow to the bed) in a certain area over a certain time. [$kg/m^2/s$]

Specific discharge: The discharge (through a channel) divided by the width of the channel [m2/s]

Subcritical flow: A flow in which the flow velocity is smaller than the surface wave propagation velocity. Gravitational forces dominate over inertial forces. The Froude number is smaller than unity.

Supercritical flow: A flow in which the flow velocity is large than the surface wave propagation velocity. Inertial forces dominate over gravitational forces. The Froude number is larger than unity.

TKE: Turbulent kinetic energy (TKE) the mean kinetic energy per unit mass associated with eddies in turbulent flow. Physically, the turbulence kinetic energy is characterised by measured root-mean-square velocity fluctuations.

Transportational (bedform): the vertical height of a sedimentary sequence is constant over time (i.e. the same amount of sediment is deposited than is eroded)

UMB: Upstream-migrating bedform

A.2

A.2.1 Governing equations of Reynold-Averaging Navier-Stokes and Turbulence models

Navier-Stokes Equations:

Mass balance equation:

$$\frac{\partial \rho}{\partial t} + \frac{\partial}{dx}(\rho u) + \frac{\partial}{dy}(\rho v) + \frac{\partial}{dz}(\rho w) = 0 \quad (1.1)$$

Momentum Balance equations:

$$\frac{\partial u}{\partial t} + u\frac{\partial u}{\partial x} + v\frac{\partial u}{\partial y} + w\frac{\partial u}{\partial x} = -\frac{1}{\rho}\frac{\partial p}{\partial x} + G_x + f_x \quad (1.2)$$

$$\frac{\partial v}{\partial t} + u\frac{\partial v}{\partial x} + v\frac{\partial v}{\partial y} + w\frac{\partial v}{\partial x} = -\frac{1}{\rho}\frac{\partial p}{\partial y} + G_y + f_y \quad (1.3)$$

$$\frac{\partial w}{\partial t} + u\frac{\partial w}{\partial x} + v\frac{\partial w}{\partial y} + w\frac{\partial w}{\partial x} = -\frac{1}{\rho}\frac{\partial p}{\partial z} + G_z + f_z \quad (1.4)$$

Equations related to the turbulence model:

One equation definition of turbulent kinetic ($k_{T,}$ *or TKE*) energy as rum of root-mean-square of velocity fluctuation:

$$k_t = \frac{1}{2}(\overline{u'^2} + \overline{v'^2} + \overline{w'^2}) \quad (1.5)$$

Transport equation for turbulent kinetic energy (TKE):

$$\frac{\partial k_T}{\partial t} + \left(u\frac{\partial k_T}{\partial x} + v\frac{\partial k_T}{\partial y} + w\frac{\partial k_T}{\partial z}\right) = P_T + D_K - \varepsilon_T \quad (1.5)$$

where P_T is the turbulent kinetic energy production term, D_K is the turbulent kinetic energy diffusion term, ε_T refers to turbulent dissipation.

Transport equation for turbulent dissipation:

$$\frac{\partial \varepsilon_T}{\partial t} + \left(u\frac{\partial \varepsilon_T}{\partial x} + v\frac{\partial \varepsilon_T}{\partial y} + w\frac{\partial \varepsilon_T}{\partial z}\right) = \frac{C_{\varepsilon 1}\,\varepsilon_T}{k_T}P_T + D_\varepsilon - C_{\varepsilon 2}\frac{\varepsilon_T^2}{k_T} \quad (1.6)$$

where D_ε refers to the diffusion of dissipation of turbulence $C_{\varepsilon 1,\varepsilon 2}$ is a dimensionless parameter.

Dynamic viscosity (the viscosity to approximate the effects of turbulence) is calculated with turbulent kinetic energy and the turbulent dissipation:

$$\mu = \rho(\nu_m + \nu_t) \quad (1.7)$$

where:

$$\nu_T = 0.085 \frac{k_T^2}{\varepsilon_T} \quad (1.8)$$

Further details on the k-epsilon RNG turbulence model van be found in (Basani et al., 2014) and the FLOW-3D documentation release 11.0.0 (Flow Science, 2014)

A.2.2 Equations governing sediment transport

Shields numbers:

The Shields parameter is a dimensionless form of bed shear stress defined as:

$$\theta_n = \frac{\tau}{g d_n(\rho_n - \rho_f)} \quad (2.1)$$

where g is gravity in absolute value, ρ_f is the fluid density, ρ_n is the mass density of sediment grains, and d_n is grain diameter. The subscript n represents the n-th sediment species.

The critical Shields parameter $\theta_{cr,n}$ is used to define the critical bed shear stress $\tau_{cr,n}$, at which sediment movement begins for both entrainment and bedload transport:

$$\theta_{cr,n} = \frac{\tau_{cr,n}}{g d_n(\rho_n - \rho_f)} \quad (2.2)$$

The base value of $\theta_{cr,n}$ is for a flat and horizontal bed of identically-sized grains. It can be either specified by users (0.05 by default) or determined from the Soulsby-Whitehouse equation (Soulsby and Whitehouse, 1997):

$$\theta_{cr,n} = \frac{0.3}{1+1.2d_{*,n}} + 0.055\left(1 - e^{-0.02 d_{*,n}}\right) \quad (2.3)$$

where $d_{*,n}$ is the dimensionless grain size given by:

$$d_{*,n} = d_n \left[\frac{g(s_n - 1)}{\nu_f}\right]^3 \quad (2.4)$$

Here $s_n = \rho_n / \rho_f$, and ν_f is the kinematic viscosity of fluid. Note the Soulsby-Whitehouse equation in equation (2.3) has replaced the Shields-Rouse equation used in the old model due to its wider range of validity (Soulsby, 1997).

At a sloping bed interface, the gravity applies a tangential component of force to make the packed bed more or less stable depending on the flow direction. As a

result, the critical shear stress increases if the fluid flow goes up the slope and decreases if the flow goes down. It is an option to users that $\theta_{cr,n}$ can be modified for the sloping bed effect following Soulsby (1997):

$$\theta'_{cr} = \theta_{cr} \frac{\cos(\psi)\sin(\chi)+\sqrt{\cos^2(\chi)\tan^2(\omega)-\sin^2(\psi)\sin^2(\chi)}}{\tan(\varphi)} \quad (2.5)$$

Bed load transport:

The dimensionless form of the bedload transport rate for species *n* is defined as

$$\Phi_n = \frac{q_{b,n}}{\left[g(s_n-1){d_n}^3\right]^{\frac{1}{2}}} \quad (2.6)$$

where $q_{b,n}$ is the volumetric bedload transport rate per unit bed width (in units of volume per width per time). Φ_n is calculated using the Meyer-Peter and Muller equation (1948),

$$\Phi_n = B_n\left(\theta_n - \theta_{cr,n}\right)^{1.5} c_{b,n} \quad (2.7)$$

where B_n is the bedload coefficient. It is generally 5.0 to 5.7 for low transport, around 8.0 for intermediate transport, and up to 13.0 for very high transport (for example, sand in sheet flow under waves and currents). A value of 8.0 is used in this study, which is the most commonly used value in the literature (Gladstone et al., 1998). $c_{b,n}$ is the volume fraction of species *n* in the bed material,

$$c_{b,n} = \frac{\text{net volume of species } n}{\text{net volume of all species}} \quad (2.8)$$

Note $c_{b,n}$ does not exist in the original Meyer-Peter and Muller equation. It is added in equation (2.7) to account for the effect of multiple species.

The relationship in Van Rijn (1984) is to estimate the bedload layer thickness h_n,:

$$h_n = 0.3 d_n d_{*,n}^{0.7} \left(\frac{\theta_n}{\theta_{cr,n}} - 1\right)^{0.5} \quad (2.9)$$

The bedload velocity $\boldsymbol{u}_{b,n}$ is calculated by

$$\boldsymbol{u}_{b,n} = \frac{\boldsymbol{q}_{b,n}}{h_n c_{b,n} f_b} \quad (2.10)$$

where f_b is the total packing fraction of sediments. Both $\boldsymbol{u}_{b,n}$ and $\boldsymbol{q}_{b,n}$ are in direction of the fluid flow adjacent to the bed interface.

Suspended load transport:

Appendix A.2

In this model, entrainment and deposition are treated as two opposing micro-processes that take place at the same time. They are combined to determine the net rate of exchange between the packed bed and the suspended sediments in the flow. For entrainment, the velocity at which the grains leave the packed bed is the lifting velocity and is calculated based on Winterwerp et al. (1992) and Mastbergen and Van Den Berg, (2003),

$$\boldsymbol{u_{lift}} = \alpha_i n_s d_*^{0.3} (\theta_i - \theta_{cr})^{1.5} \sqrt{\frac{\|g\| d (\rho_s - \rho_f)}{\rho_f}} \tag{2.11}$$

where α_i is the entrainment coefficient of species *n* (default value is 0.018), and $\boldsymbol{n}_s$ is the outward normal vector of the packed bed surface. In deposition, the settling velocity of Soulsby (1997) is used:

$$\boldsymbol{u_{settle}} = \frac{\boldsymbol{g}}{g}\left[(10.36^2 + 1.049 d_*^3)^{1/2} - 10.36\right]\frac{\nu_f}{d} \tag{2.12}$$

where $\boldsymbol{g}$ is the gravity acceleration. $\boldsymbol{u}_{settle,n}$ is assumed in the same direction of $\boldsymbol{g}$.

For each species, the suspended sediment concentration is calculated by solving its own transport equation:

$$\frac{\partial C_{s,n}}{\partial t} + \nabla \cdot \left(C_{s,n} \boldsymbol{u}_{s,n}\right) = \nabla \cdot \nabla \left(D C_{s,n}\right) \tag{2.13}$$

Here $C_{s,n}$ is the suspended sediment mass concentration, which is defined as the sediment mass per volume of fluid-sediment mixture; *D* is the diffusivity; $\boldsymbol{u}_{s,n}$ is the grain velocity of species *n*. It is noted that each sediment species in suspension moves at its own velocity that is different from those of fluid and other species. This is because grains with different mass density and sizes have different inertia and receive different drag force.

Correspondingly, the suspended sediment volume concentration $c_{s,n}$ is defined as the suspended sediment species *n* volume per volume of fluid-sediment mixture. It is related to $C_{s,n}$ by:

$$c_{s,n} = \frac{C_{s,n}}{\rho_n} \tag{2.14}$$

The mass density of the fluid-sediment mixture is calculated using:

$$\bar{\rho} = \sum_{m=1}^{N} c_{s,m}\, \rho_{s,m} + \left(1 - c_{s,tot}\right) \rho_f \tag{2.15}$$

where *N* is the total number of species, and $c_{s,tot}$ is the total suspended sediment volume concentration,

To solve equation (18) for $C_{s,n}$, $\boldsymbol{u}_{s,n}$ must be calculated first. It is assumed that: (1) the grains in suspension do not have strong interactions with each other; (2) the velocity difference between the suspended sediments and the fluid-sediment mixture is mainly the settling velocity of grains, $\boldsymbol{u}_{settle,n}$, that is defined in equation (2.12). Thus, $\boldsymbol{u}_{s,n}$ is evaluated using

$$\boldsymbol{u}_{s,n} = \overline{\boldsymbol{u}} + \boldsymbol{u}_{settle,n} c_{s,n} \tag{2.16}$$

where $\overline{\boldsymbol{u}}$ is the bulk velocity of the fluid-sediment mixture:

$$\overline{\boldsymbol{u}} = \sum_{m=1}^{N} c_{s,m}\, \boldsymbol{u}_{s,m} + \left(1 - c_{s,tot}\right)\boldsymbol{u}_f \tag{2.17}$$

$\overline{\boldsymbol{u}}$ is obtained by solving the continuity and Navier-Stokes equations with a turbulence closure model (equations in A2.1)

A.2.3 List of symbols to understand A.2.1 and A.2.2

The n subscript denotes that this parameter applies to a specific sediment species.

$A_{x,y,z}$	fractional area
C_{mass}	suspended sediment mass-concentration
C_{vol}	suspended sediment volume concentration
$C_{\varepsilon 1,\varepsilon 2}$	dimensionless parameter
D	diffusion coefficient
D_K	turbulent kinetic energy diffusion term
D_ε	diffusion of dissipation of turbulence term
d	grainsize
d_*	dimensionless grain parameter
$f_{x,y,z}$	viscous accelerations
Fr	Froude number
g	gravitational acceleration
$G_{x,y,z}$	body accelerations
k_T	turbulent kinetic energy
P_T	turbulent kinetic energy production term
q_b	bed-load transport rate
$\mathbf{u_s}$	velocity of the suspended sediment
$\bar{\boldsymbol{u}}$	mean velocity of water-sediment mixture, obtained via Navier-Stokes
$\mathbf{u_{lift}}$	lift velocity
$\mathbf{u_{bedload}}$	bed-load velocity
$\mathbf{u_{settle}}$	sediment settling mass-flux
α	entrainment coefficient
β	bed-load coefficient
δ	thickness bed-load layer
ε_T	turbulent dissipation
θ	local Shields number
θ_{cr}	critical Shields number
μ	dynamic viscosity
ν_f	kinematic viscosity of water
ρ_s	density of the sediment
ρ_f	density of the fluid

$\bar{\rho}$	mean density fluid-sediment mixture
τ	shear stress
τ_{cr}	critical shear stress
χ	angle slope of bed
ψ	angle between flow and upslope direction
ω	angle of repose

A.3

A.3.1 Squamish delta used to constrain boundary conditions

The Squamish Delta is located in the Howe Sound, a fjord in British Columbia, Canada. It is a sandy fjord-head system fed by the Squamish River. The subaqueous delta is host to three subaqueous channels. The channels are populated by crescent-shape bedforms that migrate upstream. The bedforms have wavelengths of tens of metres (~30m on average), and a wave-height of 2-3m (Hughes Clarke, 2016). Direct monitoring of the crescent-shape bedforms has shown that upstream migration beneath turbidity currents (Hughes Clarke, 2016). The channels have gradients of <10° near the delta-lip (most proximal) to 1.4° 2500m from the delta-lip, and 5° at the monitoring location of Hughes Clarke (2016). Turbidity currents observed in the Squamish submarine channels had flow velocities of 1.5-3 m/s, and a thickness of 3-7m. A good quantification of the sediment concentration in the observed turbidity currents is not available.

The flow data recorded in the Squamish submarine channels have provided the boundary conditions used in the simulations. As sediment concentration data is not provided we estimated sediment concentrations that would result in Froude-supercritical flow conditions (Fr_{50} ≈1-3), which were thought to be required to create upstream-migrating bedforms. The boundary conditions in appendix 1 reflect the inflow conditions (height, velocity and sediment concentration), which do not necessarily reflect the “steady state” flow heights, velocity and thickness. The flow thicknesses observed further downslope are variable 2-7m (Fig. 1), and flow velocity maxima are variable too but typically between 1.5-2.5 m/s.

A.3.2 Table of boundary conditions and results

simulation	boundary conditions				results				
#	flow velocity (m/s)	flow thickness (m)	sediment concentration (kg/m3)	slope	UMBs?	Fr50	Fr90	max Ri50	Θ90
1	3.3	1	75	4.5	Y	1.33	2.37	1	1.78
2	3.3	1	25	4.5	N	1.11	2.45	0.23	3.07
3	3.3	1	75	4.5	Y	1.48	2.58	0.93	1.32
4	3.3	1	100	4.5	Y	1.07	1.98	1.44	0
5	1.5	1	50	4.5	N	1.71	2.59	3.32	2.3
6	2.5	1	50	4.5	N	1.51	2.53	1.17	0
7	4.5	1	50	4.5	N	1.23	2.49	0.24	1.1
8	3.3	1	50	4.5	N	1.35	2.36	0.51	1.36
9	3.3	1	50	4.5	N	1.42	2.51	0.56	1.17
10	3.3	1	50	4.5	N	1.26	2.70	0.2	1.28
11	3.3	1	50	4.5	N	0.86	1.64	0.39	0.82
12	3.3	0.5	75	4.5	Y	1.04	2.01	1.58	4.28
13	3.3	2	50	4.5	N	1.71	2.58	1.77	0
14	3.3	0.5	50	4.5	N	1.03	1.74	1.35	3.07
15	3.3	1	65	4.5	N	1.41	2.54	0.7	0.61
16	3.3	1	85	4.5	Y	1.03	2.11	1.25	3.68
17	3	1	75	4.5	Y	1.11	2.18	1.55	3.07
18	3.6	1	75	4.5	Y	1.40	2.40	1	2.42
19	3.3	1	75	4.5	Y	1.13	2.03	1.46	0.46
20	3.3	1	75	4.5	N	1.10	2.66	0.13	4.14
22	3.3	1	50	6.1	Y	1.14	2.79	0.9	3.33
23	3.3	1	50	2.7	N	1.12	2.32	0.61	3.66

A.3.3 Equations to calculate densimetric Froude number, gradient Richardson number and Shields number

The integral method of Ellison and Turner, (1959) for calculating the Froude number

$$Uh = \int_0^\infty u\, dz \qquad (1)$$

$$U^2h = \int_0^\infty u^2\, dz \qquad (2)$$

$$UCh = \int_0^\infty uc\, dz \qquad (3)$$

$$Fr_d = \frac{U}{\sqrt{(C\rho_s)(1-C\rho_w)gH}} \qquad (4)$$

In which: $U = \frac{Uh}{U^2h}$,$C = \frac{UCh}{Uh}$,$h = \frac{UCh}{UC}$,

Calculating the gradient Richardson number

$$Ri_{gr} = \frac{\partial\rho/\partial z\, g}{(\partial U/\partial z)^2} \qquad (5)$$

Calculating the Shields number

$$\theta = \frac{\tau}{(\rho_s-\rho_w)gD} \qquad (6)$$

List of variables:

C = sediment concentration

D = particle diameter

Fr_d = densimetric Froude number

g = acceleration due to gravity

H = flow height

U = flow velocity in flow-parallel (x-direction)

z = vertical distance

Θ = Shields parameter

ρ = macroscopic density of flow

ρ_s = density of sediment

ρ_w = density of water

τ = shear stress

A.3.4 Gradient Richardson profile

Below a figure of the gradient Richardson number of two simulations: one mixed and one stratified current. The lines are the 50th percentile. On the Y-axis there is a normalised height above the bed (z/h), where h is obtained through the integral relationship of the Froude number (appendix 3). On the X-axis is the gradient Richardson number. The turbidity current is considered unstratified (mixed) when the 50th percentile (bold red line) is larger than 0.25 anywhere in the profile. If the 50th percentile is lower than 0.25 for the entire profile, the turbidity current is considered stratified.

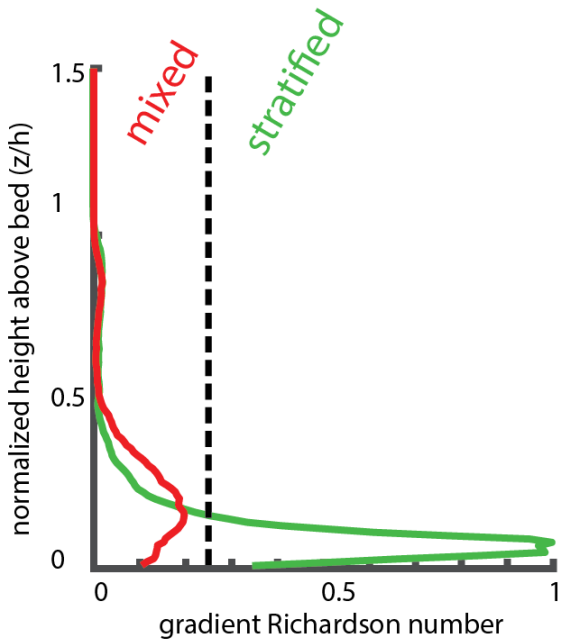

A.3.5 Flow statistics

Cross-correlation analysis is done on several flow parameters of the modelled turbidity currents. Cross-correlation functions (CCF) show the measure of similarity between two variables. A strong positive relationship is observed between discharge of the lower internally-stratified layer and the height of the velocity maximum above the bed (CCF=0.39; $p<0.05$). Cross-correlation between the height of the velocity maximum and the shear stress exerted at bed reveals a

strong inverse relationship (CCF= -0.45: p<0.05).

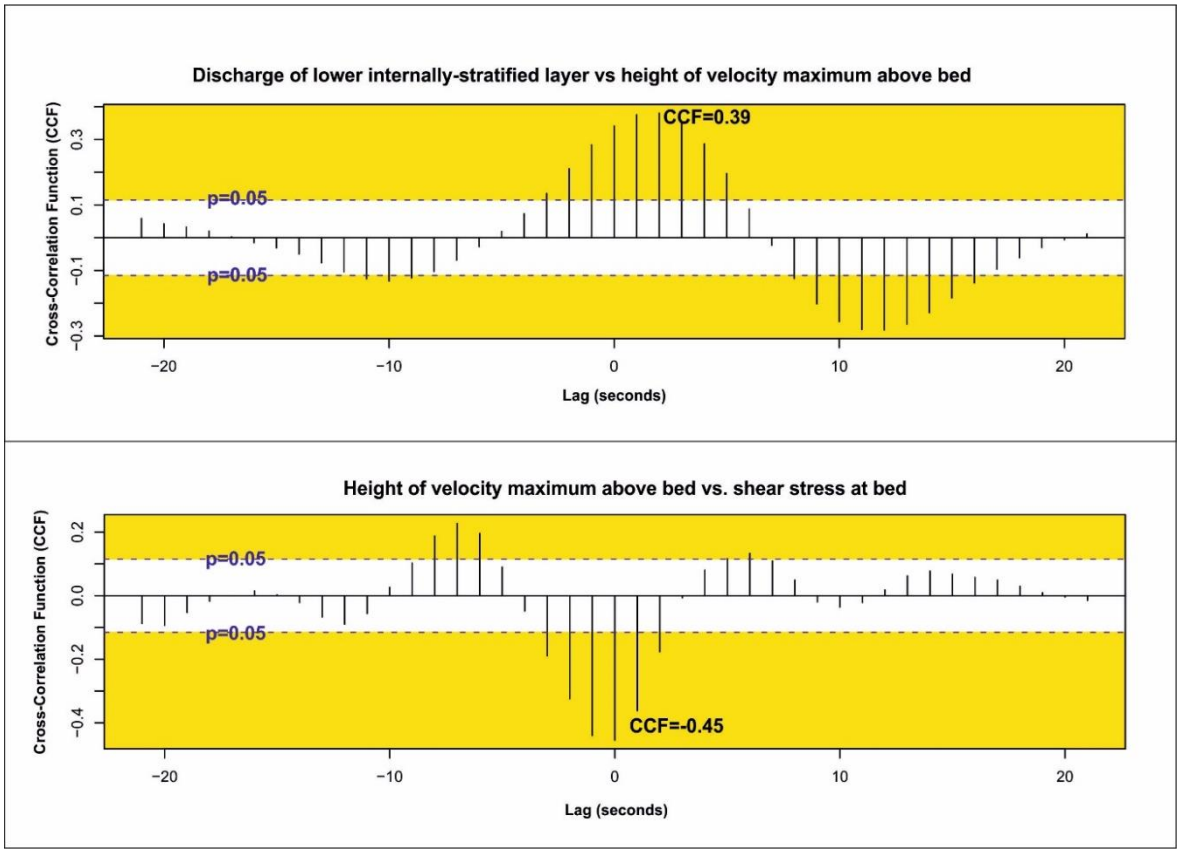

A.4

A.4.1 Map overview of the experimental area

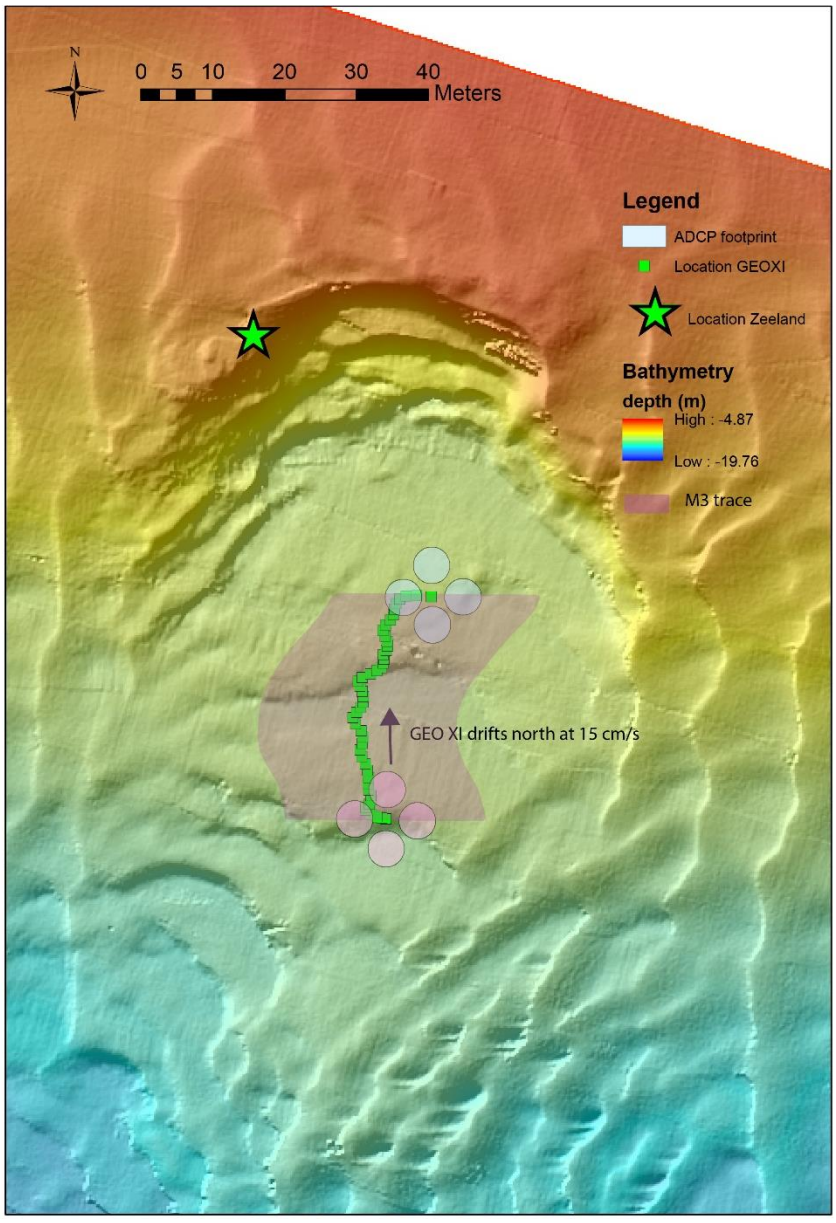

An overview map of the location of the different vessels during the event. The green star is the location where Zeeland discharged of its sediment. The green squares are the path of the GeoSurveyor XI over the time of the event, drifting north about 35m. The green line is the transect of the M3 sonar, this is the transect at one point in time, in reality it has this orientation and drifts north with the vessel. The four circles are the ADCP footprints of the four beams at one point in time, these beam footprints also drift south-to-north with the drifting vessel.

A.4.2 Morphological changes in the study area

The sloping sediment bed was covered in the tidal dunes that can be found all over the estuary and around the study site before the dredger started discharging of sediment in the study area. The tidal dunes are north-south oriented linear features of <10m in wavelength and <50cm in amplitude. The tidal dunes migrate west (appendix 4.4), this is a background signal for the turbidity currents and their associated morphological features.

Discharging sediment has created a scour-hole with a ~60m diameter and a maximum depth of ~3m. This scour hole is created by multiple unmonitored sediment discharges of the dredger. Two main pathways for the turbidity currents form as the currents flow downslope, an eastern and a western pathway (appendix 4.1). Bedforms that are crescent-shape in plan-view formed in the two turbidity current pathways, and are especially well-developed in the western pathway. These crescent-shape bedforms appear to migrate upslope as a turbidity current passes by, as seen on the difference map (appendix 4.4). In turbidity current 1 and 2 there is 25-30cm of vertical erosion on the lee-sides of the bedforms, and 5cm of vertical deposition on the stoss-sides, causing the bedform to migrate upslope. A composite cross-sectional transect trough all bathymetric data at the western turbidity current path shows the internal structure of the observed crescent-shape bedforms (appendix 4.4). The internal architecture of the crescent-shape bedforms confirms their upslope-migrating nature. Deposits are emplaced on the stoss-sides and erosion is present on the lee-side.

A.4.3 Timeline of events

DATE	TIME (UTC)	Event
28/09/2014	19:07	MBES (multibeam echosounder) survey
01/10/2014	12:59	MBES survey
	13:40	Zeeland discharges sediment
	14:04	MBES survey
	14:30	Low tide
	14:30	Zeeland discharges sediment

	16:30	Zeeland discharges sediment
	16:42	MBES survey
	19:20	Zeeland discharges sediment
	19:39	MBES survey
	19:50	Zeeland discharges sediment
	20:30	High tide
	23:24	Zeeland discharges sediment
	23:48	MBES survey
02/10/2014	00:32	Zeeland discharges 325m3 sediment (monitored Turbidity current)
	00:32-00:37	Turbidity current visible in GEOXI measurements
	01:03	MBES survey
	02:30	Low tide (approx.)
	11:57	MBES survey

A.4.4 Bathymetric difference map

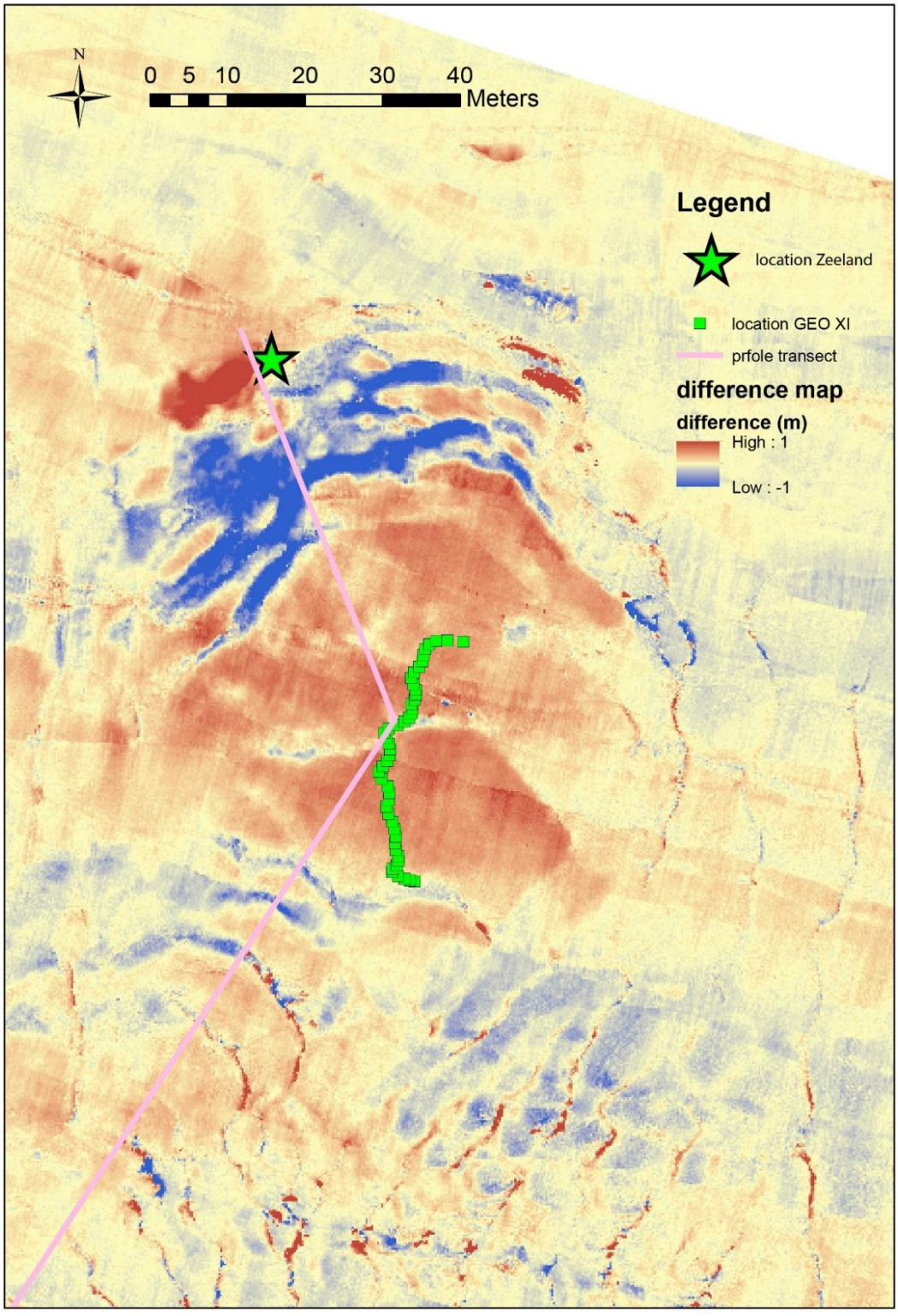

A difference map of made of the bathymetric image before and after the monitored turbidity current. The pink line is the location of the bathymetric transect image in appendix 4.5.

A.4.5 Bathymetric cross section

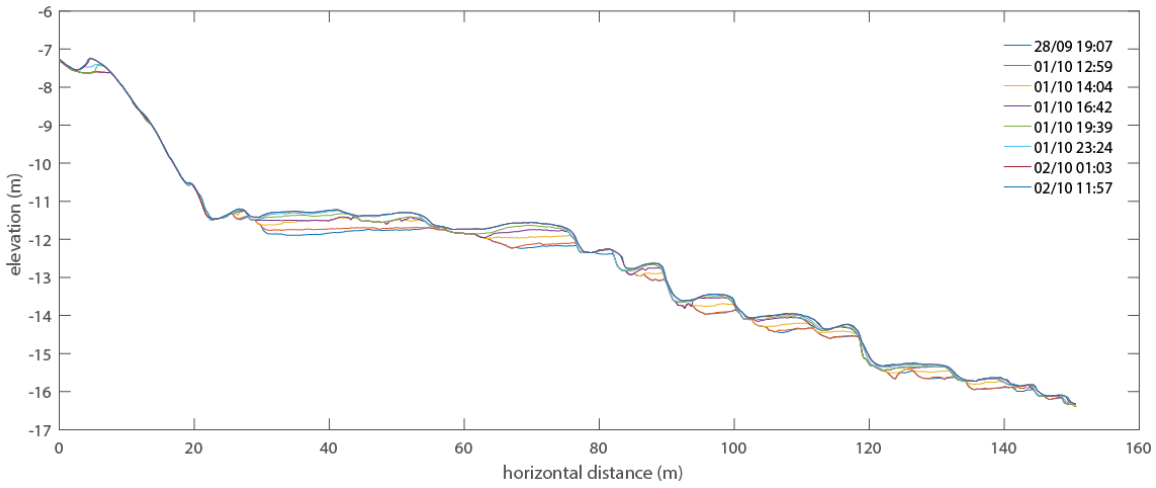

An in-profile cross-section of the deposited stratigraphy, based on all bathymetric images, at the location of the pink line in appendix 4.4.

A.4.6 ADCP analysis of the flow velocities

Constructing a flow-parallel velocity

$$V_{par} = V_{east} * \cos(\theta) + V_{north} * \sin(\theta) \qquad (4.1)$$

V_{par} is the flow-parallel velocity in the mean flow direction, V_{east} is the east velocity, V_{north} is the north-velocity, θ is the mean direction of the turbidity current

Correcting the flow-parallel velocity for background signal

$$V_{par\_corr} = V_{par} - V_{background} \qquad (4.2)$$

A.4.7 Acoustic inversion of ADCP backscatter data

The overall process of acoustic inversion is based on an implicit iterative approach and is governed by equations 4.3 and 4.4. Where *M* is the sediment concentration and α_s the attenuation due to the sediment in the water. Once the iterative process for which $\alpha_{n=0} = \alpha_w$ reaches a convergent state a value for *M* is obtained. First all other parameters need to be specified, which is done is the various sections that follow below.

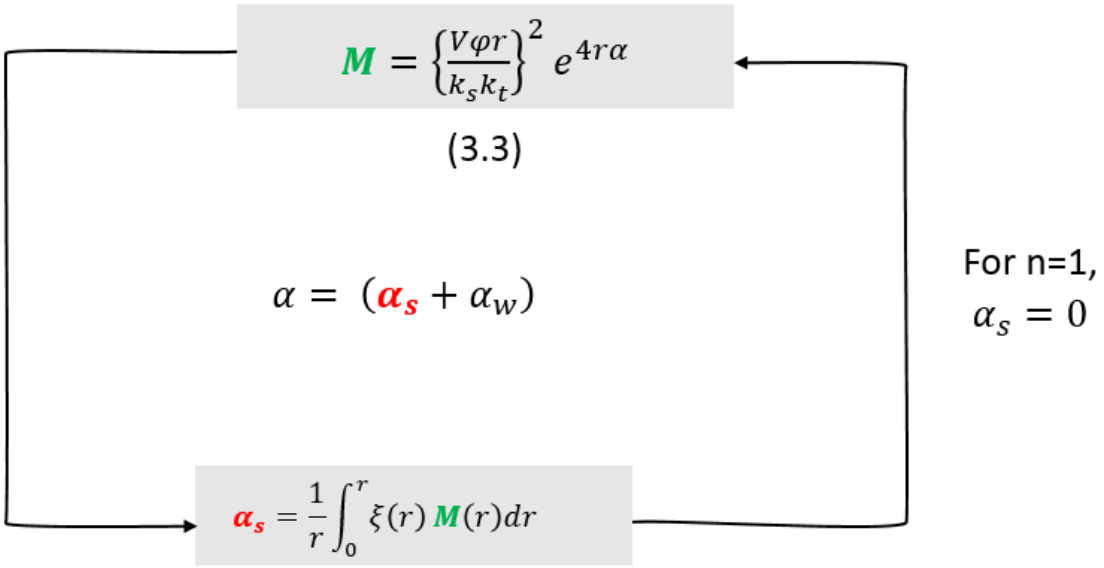

1. **V – the voltage resulting from backscatter –**

   Echo count is converted to a voltage (Deines, 1999)

   $$V = 10^{\frac{K_c(E-E_r)}{10}} \quad (4.5)$$

   E is the Echo count, E_r is the noise level, set at a value of 40, and K_c an instrument-specific parameter set at 0.4241.

2. **r – the range to the transceiver**

   As the beams are slanted at a 20° angle to the normal, the distance to the transceiver from the middle of each ADCP bin (cell) ought to be corrected

   $$r = \frac{(r_1 + n * binsize)}{\cos(20^{\pi}/_{180})} \quad (4.6)$$

   Where r is the distance of the middle of each to the transceiver, and r_1 is the mean distance of the first bin to the transceiver.

3. **φ – near field correction factor**

   There is non-spherical spreading in the near-field of the transducer that is corrected for using the method as described by Downing et al., (1995).

   $$\lambda = c/f \quad (4.7)$$

   λ is the wavelength of the sound, c is the speed of sound and f the frequency

   $$r_n = \frac{\pi * a_t^2}{\lambda} \quad (4.8)$$

   $$z = \frac{r}{r_n} \quad (4.9)$$

   Z is the normalised range dependence

$$\varphi = \frac{1+1.35z+(2.5z)^{3.2}}{1.35z+(2.5z)^{3.2}} \quad (4.10)$$

4. k_s – the backscatter properties of sediment

k_s is the backscattering property of the suspended sediment as a function of sediment grain-size and distribution.

4.1. A normalised frequency distribution of grain-size diameter is computed (f), based on the d50 and the standard deviation of samples.

$$DevAbs = DevRel * d50 \quad (4.11)$$

The absolute standard deviation *DevAbs* based on the relative standard deviation *DevRel* and *d50*.

$$Dp = d_{min} + (d_{max} - d_{min}) \quad (4.12)$$

Dp are the assigned particle diameters based on the minimum and maximum grain-size.

The following equations are to create a log-normal distribution of grain-sizes:

$$\omega = \sqrt{\log(DevRel^2 + 1)} \quad (4.13)$$

$$m_o = \sqrt{\log(\frac{d50^2}{d50^2+DevAbs^2})} \quad (4.14)$$

$$dNd = \sqrt{\frac{1}{Dp*(2\pi\omega)}\, e^{-\log(Dp-M_0)^2/2\omega^2}} \quad (4.15)$$

$$f = dNd/\sum dNd \quad (4.16)$$

f is a normalised frequency distribution of a grain with diameter *Dp*

4.2. A form function and scattering cross-section for all grain-sizes (*ffa*) is made.

$$ffa = \frac{\sum(f*a)\ \sum(f*a^2*ff^2)}{\sum(f*a^3)}^{0.5} \quad (4.17)$$

ffa is the scattering cross-section for all grain sizes (Moate and Thorne, 2012) where *a* is the grain radius

$$ff = \frac{(1-d1e^{\frac{x-d2}{d3}^2})(1+d4e^{\frac{x-d5}{d6}^2})(1+d7e^{\frac{x-d8}{d9}^2})\,x^2}{d10+d11\,x^2} \quad (4.18)$$

ff is the form function (Moate and Thorne, 2012), where *d1* to *d11* are specific to each sand mineral estimated in Moate & Thorne (2012), and $x = \frac{2\pi}{\lambda}a$.

5. K_t – a instrument-specific constant

The K_t value is a calibration constant that is instrument specific and set at $7.7080*10^5$

6. α_w – the attenuation of sound due to water

$$\alpha_w = \frac{A_1 f_1 fr^2}{f_1^2+fr^2} + \frac{A_2 P_2 f_2 fr^2}{f_2^2+fr^2} + A_3 P_3 fr^2 \quad (4.19)$$

With:

$$A_1 = 1.03 * 10^{-8} + 2.36 * 10^{-10} T - 5.22 * 10^{-12} T^2 = 1.11 * 10^{-8} \quad (4.19A)$$

$$A_2 = 5.62 * 10^{-8} + 7.52 * 10^{-10} T = 5.90 * 10^{-8} \quad (4.18B)$$

$$A_3 = (55.9 - 2.37\,T + 4.77 * 10^{-2} T^2 - 3.48 * 10^{-4} T^3) * 10^{-15} = 4.77 * 10^{-14}$$

(3.19C)

$$f_1 = 1.32 * 10^3 (T + 273.1) e^{\left[\frac{-1700}{T+273.1}\right]} = 787 \quad (4.19D)$$

$$f_2 = 1.55 * 10^7 (T + 273.1) e^{\left[\frac{-3052}{T+273.1}\right]} = 7.00 * 10^4 \quad (4.19E)$$

$$P_2 = 1 - 10.3 * 10^{-4} P + 3.7 * 10^{-7} P^2 = 0.82 \quad (4.19F)$$

$$P_3 = 1 - 3.84 * 10^{-4} P + 7.57 * 10^{-8} P^2 = 0.93 \quad (4.18G)$$

Where *T* is the water temperature, *P* is the water pressure, and *fr* is the instrument frequency (Francois and Garrison, 1982).

7. ξ – the attenuation-constant to compute α_s

ξ is a sum of the viscous absorption of the sound wave by the sediment $\xi_{viscous}$ and the scattering $\xi_{scatter}$ $\xi = \xi_{viscous} + \xi_{scatter}$

6.1 $\xi_{viscous}$

Is calculated based on equations found in (Urick, 1948)

$$\xi_{viscous} = \sum \left[\frac{k_\alpha (\sigma-1)^2}{2\rho s} * \frac{s}{s^2+(\sigma+\tau)^2} \right] \quad (4.20)$$

Where:

$$s = \frac{9}{4}\left(\frac{1}{\beta a}\right)\left(1 + \frac{1}{\beta a}\right); \quad (4.21)$$

$k_\alpha = 0.18$

$$\tau = \frac{1}{2} + \frac{9}{4}\left(\frac{1}{\beta a}\right) \quad (4.22)$$

$$\beta = \sqrt{\pi * \frac{fr}{1.52*10^{-6}}} \quad (4.23)$$

6.2 ξ scatter

$$\xi_{sactter} = \frac{3\chi}{4a\rho_s} \tag{4.24}$$

Where:

$$\chi = \frac{\sum(f*a)\ \sum(f*a^2*xx)}{\sum(f*a^3)} \tag{4.25}$$

$$xx = \frac{\rho_{sed}*0.09*x^4}{1380+560x^2+150x^4} \tag{4.26}$$

In which f is the fraction of grain-particles and ρ_s is the density of the sediment

Bibliography

Alexander, J., 2008, Bedforms in Froude-supercritical flow, *in* Marine and River Dune Dynamics Proceedings, p. 1–5.

Alexander, J., Bridge, J.S., Cheela, R.J., and Leclair, S.F., 2001, Bedforms and associated sedimentary structures formed undersupercritical waterfows over aggrading sand beds.: *Sedimentology*, v. **48**, p. 133–152.

Allen, J.R.L., 1985, Loose-boundary hydraulics and fluid mechanics; selected advances since 1961.: *Geological Society of America Bulletin*, v. **18**, p. 7–28.

Altinakar, M.S., Graf, W.H., and Hopfinger, E.J., 1996, Flow structure in turbidity currents.: *Journal of Hydraulic Research*, v. **34**, p. 713–718.

Armenio, V., and Sarkar, S., 2002, An investigation of stably stratified turbulent channel flow using large-eddy simulation.: *Journal of Fluid Mechanics*, v. **459**, p. 1–42.

Azpiroz-Zabala, M., Cartigny, M.J.B., Talling, P.J., Parsons, D.R., Sumner, E.J., Clare, M.A., Simmons, S.M., Cooper, C., and Pope, E.L., 2017, Newly recognized turbidity current structure can explain prolonged flushing of submarine canyons.:

Baas, J.H., and Best, J.L., 2008, The dynamics of turbulent, transitional and laminar clay-laden flow over a fixed current ripple.: *Sedimentology*, v. **55**, p. 635–666.

Baas, J.H., Best, J.L., and Peakall, J., 2016, Comparing the transitional behaviour of kaolinite and bentonite suspension flows.: *Earth Surface Processes and Landforms*, v. **41**, p. 1991–1921.

Babonneau, N., Delacourt, C., Cancourt, R., Sisavath, E., Bachelery, P., Mazuel, A., Jorry, S.J., Deschamps, A., Ammann, J., and Villeneuve, N., 2013, Direct sediment transfer from land to deep-sea: Insights into shallow multibeam bathymetry at La Reunion Island.: *Marine Geology*, v. **346**, p. 47–57.

Bagnold, R.A.A., 1954, Experiments on a gravity-free dispersion of large solid spheres in a Newtonian fluid under shear.: *Proceedings of the Royal Society of Londen. Series A, Mathematical and Physical Sciences*, v. **225**, p. 49–63.

Balmforth, N.J., and Mandre, S., 2004, Dynamics of roll waves.: *Journal of Fluid*

Mechanics, v. **514**, p. 1–33.

Balmforth, N.J., and Vakil, A., 2012, Cyclic steps and roll waves in shallow water flow over an erodible bed.: *Journal of Fluid Mechanics*, v. **695**, p. 35–62.

Barley, B., 1999, Deepwater problems around the world.: *Leading Edge*, v. **18**, p. 488–494.

Basani, R., Janocko, M., Cartigny, M.J.B., Hansen, W.M., and Eggenhuisen, J.T., 2014, MassFLOW-3D TM as a simulation tool for turbidity currents : some preliminary results.: *IAS Speical Publication*, v. **46**, p. 587–608.

Van den Berg, J.H., and Van Gelder, A., 1993, A new bedform stability diagram, with emphasis on the transition of ripples to plane bed in flows over fine sand and silt.: *Special Publication of the International Association of Sedimentologists*, v. **17**, p. 11–21.

Best, J., 2005, The fluid dynamics of river dunes: A review and some future research directions.: *Journal of Geophysical Research*, v. **110**, p. 1–21.

Bouma, A.H., 1962, Sedimentology of Some Flysch Deposits: A Graphic Approach to Facies Interpretation: Amsterdam/New York.

Branney, M.J., and Kokelaar, P., 2002, Pyroclastic density currents and the sedimentation of ignimbrites: London.

Breard, E.C.P.P., Lube, G., Jones, J.R., Dufek, J., Cronin, S.J., Valentine, G.A., and Moebis, A., 2016, Coupling of turbulent and non-turbulent flow regimes within pyroclastic density currents.: *Nature Geoscience*, v. **1**, p. 767–771.

Brierley, G.J., and Fryirs, K.A., 2013, Geomorphology and river management: applications of the river styles framework: John Wiley & Sons, London.

Bruschi, R., Bughi, S., and al., et, 2006a, Impact of debris flows and turbidity currents on seafloorstructures.: , p. 317–336.

Bruschi, R., Bughi, S., al., et, Spinazze, M., Torselletti, E., and Vitali, L., 2006b, Impact of debris flows and turbidily currents on seafloor structures.: *NORSK …*,, p. 317–336.

Carter, L., Burnett, D., Drew, S., Hagadorn, L., Marle, G., and Bartlett-McNeil, D., 2009, Submarine Cables and the Oceans: Connecting the World.:

Cartigny, M.J.B., Eggenhuisen, J.T., Hansen, E.W.M., and Postma, G., 2013,

Concentration-Dependent Flow Stratification In Experimental High-Density Turbidity Currents and Their Relevance To Turbidite Facies Models.: *Journal of Sedimentary Research*, v. **83**, p. 1046–1064.

Cartigny, M.J.B., Postma, G., van den Berg, J.H., and Mastbergen, D.R., 2011, A comparative study of sediment waves and cyclic steps based on geometries, internal structures and numerical modeling.: *Marine Geology*, v. **280**, p. 40–56.

Cartigny, M.J.B., Ventra, D., Postma, G., and van Den Berg, J.H., 2014, Morphodynamics and sedimentary structures of bedforms under supercritical-flow conditions: New insights from flume experiments. (J. Venditti, Ed.): *Sedimentology*, v. **61**, p. 712–748.

Chough, S.K., and Hesse, R., 1980, The Northwest Atlantic Mid-Ocean Channel of the Labrador Sea; III, Head spill vs. body spill deposits from turbidity currents on natural levees.: *Journal of Sedimentary Research*, v. **50**, p. 227–234.

Clare, M.A., Cartigny, M.J.B., Talling, P.J., North, L.J., Hizzett, J.L., Sumner, E.J., Clarke, J.E.H., and Spinewine, B., 2015a, Quantification of Near-bed Dense Layers and Implications for Seafloor Structures : New Insights into the Most Hazardous Aspects of Turbidity Currents, *in* Offshore Technology Conference, p. 1–9.

Clare, M.A., Thomas, S., Cartigny, M., and Mansour, M., 2015b, Turbidity current hazard assessment for field layout planning, *in* Frontiers in Offshore Geotechnics III, p. 978–1.

Cole, P.D., 1991, Migration direction of sand-wave structures in pyroclastic-surge deposits: implications for depositional processes.: *Geology*, v. **19**, p. 1108–1111.

Cornish, V., 1934, Ocean waves and kindred geophysical phenomena: Cambridge University Press, Cambridge.

Covault, J.A., Kostic, S., Paull, C.K., Ryan, H.F., and Fildani, A., 2014, Submarine channel initiation, filling and maintenance from sea-floor geomorphology and morphodynamic modelling of cyclic steps. (P. Talling, Ed.): *Sedimentology*, v. **61**, p. 1031–1054.

Covault, J.A., Kostic, S., Paull, C.K., Sylvester, Z., and Fildani, A., 2016, Cyclic steps and related supercritical bedforms: Building blocks of deep-water

depositional systems, western North America.: *Marine Geology*, v. **in press**, p. xxx–xxx.

Covault, J.A., Kostic, S., Paull, C.K., Sylvester, Z., and Fildani, A., 2017, Cyclic steps and related supercritical bedforms: Building blocks of deep-water depositional systems, western North America.: *Marine Geology*, v. **393**, p. 4–20.

Dade, W.B., and Huppert, H.E., 1996, Emplacement of the Taupo ignimbrite by a dilute turbulent flow.: *Nature*, v. **381**, p. 509–512.

Damuth, J.E., Kolla, V., Flood, R.D., Kowsmann, R.O., Monteiro, M.O., Gorini, M. a, Palma, J.J.C., Belderson, R.H., Obs, L.G., and States, U., 1983, Distributary channel meandering and bifurcation patterns on the Amazon deep-sea fan as revealed by long-range side-scan sonar.: *Geology*, v. **11**, p. 94–98.

Deines, K.L., 1999, Backscatter estimation using broadband acoustic Doppler Current profilers, *in* Current measurement: proceedings of the IEEE sixth working conference, p. 249–253.

Dietrich, P., Ghienne, J.-F., Normandeau, A., and Lajeunesse, P., 2016, Upslope-Migrating Bedforms In A Proglacial Sandur Delta: Cyclic Steps From River-Derived Underflows?: *Journal of Sedimentary Research*, v. **86**, p. 113–123.

Dorrell, R.M., Peakall, J., Sumner, E.J., Parsons, D.R., Darby, S.E., Wynn, R.B., Özsoy, E., and Tezcan, D., 2016, Flow dynamics and mixing processes in hydraulic jump arrays: Implications for channel-lobe transition zones.: *Marine Geology*, v. **381**, p. 181–193.

Downing, A., Thorne, P.D., and Vincent, C.E., 1995, Backscattering from a suspension in the near field of a piston transducer.: *The Journal of the Acoustical Society of America*, v. **97**, p. 1614–1620.

Duarte, J.C., Terrinha, P., Rosas, F.M., Valadares, V., Pinheiro, L.M., Matias, L., Magalhães, V., and Roque, C., 2010, Crescent-shaped morphotectonic features in the Gulf of Cadiz (offshore SW Iberia).: *Marine Geology*, v. **271**, p. 236–249.

Duller, R.A., Mountney, N.P., Russell, A.J., and Cassidy, N.C., 2008, Architectural analysis of a volcaniclastic jökulhlaup deposit, southern Iceland: sedimentary evidence for supercritical flow.: *Sedimentology*, v. **55**, p. 939–964.

Dzulynski, S., and Sanders, J.E., 1962, Current Marks on Firm Mud Bottoms.: *Transactions of the Conneticut Academy of Arts and Sciences*, v. **42**, p. 57–96.

Ellison, T.H., and Turner, J.S., 1959, Turbulent entrainment in stratified flows.: *Journal of Fluid Mechanics*, v. **6**, p. 423.

Fagherazzi, S., and Sun, T., 2003, Numerical simulations of transportational cyclic steps.: *Computers & Geosciences*, v. **29**, p. 1143–1154.

Fick, C., Boffo, C.H., Schreiner Moraes, M.A., Manica, R., and De Oliveira Borges, A.L., 2015, Mechanisms of transport and deposition of high-concentrated density currents: A detailed approach to hydrodynamic and depositional features.: *Abstracts of 31st IAS Meeting of Sedimentology held in Krakow on 22nd –25th of June 2015. Polish Geological Society*,, p. 176.

Fielding, C.R., 2006, Upper flow regime sheets, lenses and scour fills: Extending the range of architectural elements for fluvial sediment bodies.: *Sedimentary Geology*, v. **190**, p. 227–240.

Fielding, C.R., Allen, J.P., Alexander, J., and Gibling, M.R., 2009, Facies model for fluvial systems in the seasonal tropics and subtropics.: *Geology*, v. **37**, p. 623–626.

Fildani, A., Normark, W.R., Kostic, S., and Parker, G., 2006, Channel formation by flow stripping: large-scale scour features along the Monterey East Channel and their relation to sediment waves.: *Sedimentology*, v. **53**, p. 1265–1287.

Flood, R.D., Hiscott, R.N., and Aksu, A.E., 2009, Morphology and evolution of an anastomosed channel network where saline underflow enters the Black Sea.: *Sedimentology*, v. **56**, p. 807–839.

Flow Science, 2014, FLOW-3D Documentation release 11.0.0.: , p. 967.

Foley, M.G., 1977, a Quantitative Hydrodynamic Indicator I.: *Journal of sedimentary petrology*, v. **47**, p. 738–746.

Francois, R.E., and Garrison, G.R., 1982, Sound absorption based on ocean measurements: Part I:Pure water and magnesium sulfate contributions.: *Journal of the Acoustical Society of America*, v. **72**, p. 896–907.

Fricke, A.T., Sheets, B.A., Nittrouer, C.A., Allison, M.A., and Ogston, A.S., 2015, An examination of Froude-supercritical flows and cyclic steps on a subaqeous

lacustrine delta, Lake Chelan, Washington, U.S.A.: *Journal of Sedimentary Research*, v. **85**, p. 754–767.

Froude, W., 1872, Experiments on the surface-friction experienced by a plane moving through water, *in* British Association for the advancement of Science 42nd meeting,.

Froude, M.J., Alexander, J., Barclay, J., and Cole, P., 2017, Interpreting flash flood palaeoflow parameters from antidunes and gravel lenses: An example from Montserrat, West Indies.: *Sedimentology*,.

Gauer, P., Issler, D., Lied, K., Kristensen, K., and Sandersen, F., 2008, On Snow Avalanche Flow Regimes: Inferences from Observations and Measurements.: *Proceedings Whistler 2008 International Snow Science Workshop, September 21-27 2008*,, p. 717–723.

Ge, Z., Nemec, W., Gawthorpe, R.L., and Hansen, E.W.M., 2017, Response of unconfined turbidity current to normal-fault topography.: *Sedimentology*, v. **64**, p. 1–28.

Ghienne, J.-F., Girard, F., Moreau, J., and Rubino, J.-L., 2010, Late Ordovician climbing-dune cross-stratification: a signature of outburst floods in proglacial outwash environments?: *Sedimentology*, v. **57**, p. 1175–1198.

Gilbert, R., and Crookshanks, S., 2009, Sediment waves in a modern high-energy glacilacustrine environment.: *Sedimentology*, v. **56**, p. 645–659.

Gladstone, C., Phillips, J.C., and Sparks, R.S.J., 1998, Experiments on bidisperse, constant volume gravity currents: propagation and sediment deposition.: *Sedimentology*,.

Guo, J., 2002, Hunter Rouse and Shields diagram.: *Advances in Hydraulic and Water Engineering*, v. **2**, p. 1096–1098.

Hage, S., Cartigny, M.J.B., Clare, M.A., Sumner, E.J., Vendettuoli, D., Clarke, J.E.H., Hubbard, S.M., Talling, P.J., Lintern, D.G., Stacey, C.D., Englert, R.G., Vardy, M.E., Hunt, J.E., Yokokawa, M., et al., 2018, How to recognize crescentic bedforms formed by supercritical turbidity currents in the geologic record : Insights from active submarine channels.: , p. 563–566.

Hand, B.M., 1974, Supercritical flow in density currents.: *Journal of sedimentary petrology*, v. **44**, p. 637–648.

Hassan, F.A., 1997, The dynamics of a riverine civilization: A geoarchaeological perspective on the nile valley, egypt.: *World Archaeology*, v. **29**, p. 51–74.

Haughton, P., Davis, C., McCaffrey, W., and Barker, S., 2009, Hybrid sediment gravity flow deposits – Classification, origin and significance.: *Marine and Petroleum Geology*, v. **26**, p. 1900–1918.

Heezen, B.C., and Ewing, M., 1952, Turbidity Currents and Submarine Slumps, and the 1929 Grand Banks Earthquake.: *American Journal of Science*, v. **250**, p. 849–873.

Heezen, B.C., Menzies, R.J., Schneider, E.D., Ewing, W.M., and Granelli, N.C.I., 1964, Congo Submarine Canyon.: *AAPG Bulletin*, v. **48**, p. 1126–1149.

Heinio, P., and Davies, R.J., 2009, Trails of depressions and sediment waves along submarine channels on the continental margin of Espirito Santo Basin, Brazil.: *Geological Society of America Bulletin*, v. **121**, p. 698–711.

Hiscott, R.N., 1994a, Loss of capacity, not competence, as the fundamental process governing deposition from turbidity currents.: *Journal of Sedimentary Research*, v. **64**, p. 203–214.

Hiscott, R.N., 1994b, Traction-Carpet Stratification in Turbidites-Fact or Fiction?: *SEPM Journal of Sedimentary Research*, v. **64A**, p. 204–208.

Hopfinger, E.J., 1983, Snow Avalanche Motion and Related Phenomena.: *Annual Review of Fluid Mechanics*, v. **15**, p. 47–76.

Howard, L.N., 1961, Note on a paper of John W. Miles.: *Journal of Fluid Mechanics*, v. **10**, p. 509–512.

Hübl, J., Kienholz, H., and Editors, A.L., 2002, Documentation of Mountain Disasters, *in* State of Discussion in the European Mountain Areas, p. 202.

Hughes Clarke, J.E., 2016, First wide-angle view of channelized turbidity currents links migrating cyclic steps to flow characteristics.: *Nature Communications*, v. **7**, p. 1–13.

Hughes Clarke, J.E., Brucker, S., Muggah, J., Hamilton, T., Cartwright, D., Church, I., and Kuus, P., 2012, Temporal progression and spatial extent of mass wasting events on the Squamish prodelta slope, *in* Eberhardt ed., Landslides and Engineered Slopes: Protecting Society trhrough Improved Understanding, Taylor & Francis Group, London, p. 1091–1096.

Issler, D., 2003, Experimental information on the dynamics of dry-snow avalanches, *in* Dynamic Response of granular and porous materials under large and catastrophic deformations, Springer, Berlin, Heidelberg, p. 109–160.

Issler, D., 1998, Modelling of snow entrainment and deposition in powder-snow avalanches.: *Annals of Glaciology*, v. **26**, p. 253–258.

Izumi, N., Yokokawa, M., and Parker, G., 2017, Incisional cyclic steps of permanent form in mixed bedrock-alluvial rivers.: *Journal of Geophysical Research: Earth Surface*, v. **122**, p. 130–152.

Jobe, Z.R., Lowe, D.R., and Uchytil, S.J., 2011, Two fundamentally different types of submarine canyons along the continental margin of Equatorial Guinea.: *Marine and Petroleum Geology*, v. **28**, p. 843–860.

Jorritsma, 1973, Sluiting tijdelijke toegang Europoort - onderzoek naar de taludhellingen onder water aangebracht zand - verslag model onderzoek: Waterloopkundig Laboratorium.

Kennedy, J.F., 1969, The Formation of Sediment Ripples, Dunes, and Antidunes.: *Annual Review of Fluid Mechanics*, v. **1**, p. 147–168.

Khripounoff, A., Crassous, P., Lo Bue, N., Dennielou, B., and Silva Jacinto, R., 2012, Different types of sediment gravity flows detected in the Var submarine canyon (northwestern Mediterranean Sea).: *Progress in Oceanography*, v. **106**, p. 138–153.

Kleinhans, M.G., Bierkens, M.F.P.F.P., Perk, M. Van Der, and Van Der Perk, M., 2010, HESS Opinions On the use of laboratory experimentation: " Hydrologists, bring out shovels and garden hoses and hit the dirt ".: *Hydrol. Earth Syst. Sci*, v. **14**, p. 369–382.

Kneller, B.C., and Branney, M.J., 1995, Sustained high-density turbidity currents and the deposition.: *Sedimentology*, v. **42**, p. 607–616.

Kochel, R.C., 1988, Geomorphic impact of large floods: review and new perspectives on magnitude and frequency, *in* Flood Geomorphology, John Wiley & Sons, New York, p. 169–187.

Kohler, A., Mcelwaine, J.N., and Sovilla, B., 2018, GEODAR Data and the Flow Regimes of Snow Avalanches.: *Journal of Geophysical Research*, v. **in press**.

Komar, P.D., 1971, Hydraulic jumps in turbidity currents.: *Geological Society Of America Bulletin*, v. **82**, p. 101–110.

Kostic, S., 2011, Modeling of submarine cyclic steps: Controls on their formation, migration, and architecture.: *Geosphere*, v. **7**, p. 294–304.

Kostic, S., 2014, Upper flow regime bedforms on levees and continental slopes: Turbidity current flow dynamics in response to fine-grained sediment waves.: *Geosphere*, v. **10**, p. 1094–1103.

Kostic, S., and Parker, G., 2006, The response of turbidity currents to a canyon–fan transition: internal hydraulic jumps and depositional signatures.: *Journal of Hydraulic Research*, v. **44**, p. 631–653.

Kostic, S., Sequeiros, O., Spinewine, B., and Parker, G., 2010, Cyclic steps: A phenomenon of supercritical shallow flow from the high mountains to the bottom of the ocean.: *Journal of Hydro-environment Research*, v. **3**, p. 167–172.

Kuenen, P.H., and Migliorini, C.I., 1950, Turbidity currents as a cause of graded bedding.: *The Journal of Geology*, v. **58**, p. 91–127.

Lamb, M.P., Parsons, J.D., Mullenbach, B.L., Finlayson, D.P., Orange, D.L., and Nittrouer, C. a., 2008, Evidence for superelevation, channel incision, and formation of cyclic steps by turbidity currents in Eel Canyon, California.: *Geological Society of America Bulletin*, v. **120**, p. 463–475.

Lang, J., and Winsemann, J., 2013, Lateral and vertical facies relationships of bedforms deposited by aggrading supercritical flows: From cyclic steps to humpback dunes.: *Sedimentary Geology*, v. **296**, p. 36–54.

Lintern, D.G., Hill, P.R., and Stacey, C., 2016, Powerful unconfined turbidity current captured by cabled observatory on the Fraser River delta slope, British Columbia, Canada.: *Sedi*, v. **63**, p. 1041–1064.

Louge, M.Y., Carroll, C.S., and Turnbull, B., 2011, Role of pore pressure gradients in sustaining frontal particle entrainment in eruption currents: The case of powder snow avalanches.: *Journal of Geophysical Research: Earth Surface*, v. **116**, p. 1–13.

Lowe, D.R., 1976, Grain Flow and Grand Flow Deposits.: *Journal of sedimentary petrology*, v. **46**, p. 188–199.

Lowe, D.R., 1982, Lowe, D. R. (1982). Sediment gravity flows: II Depositional models with special reference to the deposits of high-density turbidity currents.: *Journal of Sedimentary Research*, v. **52**, p. 279–297.

Macdonald, R.G., Alexander, J., Bacon, J.C., and Cooker, M.J., 2013, Variations in the architecture of hydraulic-jump bar complexes on non-eroding beds. (S. Dey, Ed.): *Sedimentology*, v. **60**, p. 1291–1312.

Maier, K.L., Fildani, A., Paull, C.K., McHargue, T.R., Graham, S. a., and Caress, D.W., 2013, Deep-sea channel evolution and stratigraphic architecture from inception to abandonment from high-resolution Autonomous Underwater Vehicle surveys offshore central California.: *Sedimentology*, v. **60**, p. 935–960.

Mastbergen, D.R., 2015, Memo Korrelverdelingen bodem Westerschelde bij Plaat van Walsoorden (1220095-000-ZKS-0013).:

Mastbergen, D.R., and Van Den Berg, J.H., 2003, Breaching in fine sands and the generation of sustained turbidity currents in submarine canyons.: *Sedimentology*, v. **50**, p. 625–637.

Mastbergen, D.R., van den Ham, G., Cartigny, M.J.B., Koelewijn, A., de Kleine, M., Hizzett, J.L., Azpiroz, M., and Vellinga, A.J., 2016, Multiple flow slide experiment in the Westerschelde Estuary, The Netherlands Dick, *in* Submarine Mass Movements and their Consequences, p. 241–249.

McCave, I.N., 2017, Formation of sediment waves by turbidity currents and geostrophic flows: A discussion.: *Marine Geology*, v. **390**, p. 89–93.

Meiburg, E., McElwaine, J., and Kneller, B., 2012, Turbidity Currents and Powder Snow Avalanches.: *Handbook of Environmental Fluid Dynamics, Volume One*,, p. 557–571.

Meyer-Peter, E. and Müller, R., 1948, Formulas for Bed-Load Transport, *in* International Association for Hydraulic Structures Research, p. 38–64.

Micallef, A., and Mountjoy, J.J., 2011, A topographic signature of a hydrodynamic origin for submarine gullies.: *Geology*, v. **39**, p. 115–118.

Middleton, G. V, 1965, Antidune cross-bedding in a large flume.: *Journal of sedimentary petrology*, v. **35**, p. 922–927.

Middleton, G. V., 1993, Sediment deposition from turbidity currents.: *Annual*

Review of Earth and Planetary Sciences, v. **21**, p. 89–114.

Migeon, S., Mulder, T., Savoye, B., and Sage, F., 2006, The Var turbidite system (Ligurian Sea, northwestern Mediterranean)—morphology, sediment supply, construction of turbidite levee and sediment waves: implications for hydrocarbon reservoirs.: *Geo-Marine Letters*, v. **26**, p. 361–371.

Migeon, S., Savoye, B., and Faugeres, J.-C., 2000, Quaternary development of migrating sediment waves in the Var deep-sea fan: distribution, growth pattern, and implication for levee evolution.: *Sedimentary Geology*, v. **133**, p. 265–293.

Migeon, S., Savoye, B., Zanella, E., Mulder, T., Faugeres, J.C., and Weber, O., 2001, Detailed seismic-reflection and sedimentary study of turbidite sediment waves on the var sedimentary ridge (SE France): Significance for sediment transport and deposition and for the mechanisms of sediment-wave construction.: *Marine and Petroleum Geology*, v. **18**, p. 179–208.

Miles, J.W., 1961, On the Stability of Nonhomogeneous Shear Flows.: *Journal of Fluid Mechanics*, v. **4**, p. 496–508.

Milliman, J.D., and Syvitski, J.P.M., 1992, Geomorphic/Tectonic Control of Sediment Discharge to the Ocean: The Importance of Small Mountainous Rivers.: *The Journal of Geology*, v. **100**, p. 525–544.

Moate, B.D., and Thorne, P.D., 2012, Interpreting acoustic backscatter from suspended sediments of different and mixed mineralogical composition.: *Continental Shelf Research*, v. **46**, p. 67–82.

Moorhouse, B.L., and White, J.D.L., 2016, Interpreting ambiguous bedforms to distinguish subaerial base surge from subaqueous density current deposits.: *The Depositional Record*, v. **2**, p. 173–195.

Morozova, G.S., 2005, A review of Holocene avulsions of the Tigris and Euphrates Rivers and possible effects on the evolution of civilizations in lower Mesopotamia.: *Geoarchaeology*, v. **20**, p. 401–423.

Negretti, M.E., Flòr, J.-B., and Hopfinger, E.J., 2017, Development of gravity currents on rapidly changing slopes.: *Journal of Fluid Mechanics*, v. **833**, p. 70–97.

Nisbet, E.O., and Piper, D.J.W., 1998, Giant submarine landslides.: *Nature*, v.

392, p. 329–330.

Nordin, C.F., and Beverage, J.P., 1965, Sediment Transport in the Rio Grande New Mexico: US Government Printing Office, Washington.

Normandeau, A., Lajeunesse, P., G.Poiré, A., and Francus, P., 2016, Morphological expression of bedforms formed by supercritical sediment density flows in four fjord-lake deltas of the south-eastern Canadian Shield (Eastern Canada).: *Sedimentology*, v. **63**, p. 2106–2129.

Normark, W.R., Piper, D.J.W., Posamentier, H., Pirmez, C., and Migeon, S., 2002, Variability in form and growth of sediment waves on turbidite channel levees.: *Marine Geology*, v. **192**, p. 23–58.

Ohata, K., Naruse, H., Yokokawa, M., and Viparelli, E., 2017, New Bedform Phase Diagrams and Discriminant Functions for Formative Conditions of Bedforms in Open-Channel Flows.: *Journal of Geophysical Research: Earth Surface*, v. **122**, p. 2139–2158.

Parker, G., 2008, Cyclic steps: A phenomenon of supercritical shallow flow from the high mountains to the bottom of the ocean, *in* 2nd International symosium on shallow flows,.

Parker, G., 1996, Some Speculations on the Relation Between Channel Morphology and Channel-scale Flow Structures, *in* Ashworth, P.J., Bennett, S.J., Best, J.L., and McLelland, S.J. eds., Coherent flow structures in open channels, John Wiley and Sons Ltd., London, p. 424–458.

Parker, G., and Izumi, N., 2000, Purely erosional cyclic and solitary steps created by flow over a cohesive bed.: *Journal of Fluid Mechanics*, v. **419**, p. 203–238.

Parsons, D.R., and Best, J., 2013, Bedforms: views and new perspectives from the third international workshop on Marine and River Dune Dynamics (MARID3).: *Earth Surface Processes and Landforms*, v. **38**, p. 319–329.

Paull, C.K., Caress, D.W., III, W.U., Lundsten, E., and Meiner-johnson, M., 2011, High-resolution bathymetry of the axial channels within Monterey and Soquel submarine canyons , offshore central California.: *Geosphere*, v. **7**, p. 1077–1101.

Paull, C.K., Ussler III, W., Caress, D.W., Lundsten, E., Covault, J. a., Maier, K.L., Xu, J., and Augenstein, S., 2010, Origins of large crescent-shaped bedforms

within the axial channel of Monterey Canyon, offshore California.: *Geosphere*, v. **6**, p. 755–774.

Pettingill, H.S., and Weimer, P., 2002, Worlwide deepwater exploration and production: Past, present, and future.: *The Leading Edge*, v. **21**, p. 371–376.

Ponce, J.J., and Carmona, N., 2011, Coarse-grained sediment waves in hyperpycnal clinoform systems, Miocene of the Austral foreland basin, Argentina.: *Geology*, v. **39**, p. 763–766.

Postma, G., and Cartigny, M.J.B., 2014, Super- and subcritical turbidity currents and their deposits – a synthesis.: *Geology*, v. **16**, p. 3830.

Postma, G., Cartigny, M., and Kleverlaan, K., 2009, Structureless, coarse-tail graded Bouma Ta formed by internal hydraulic jump of the turbidity current?: *Sedimentary Geology*, v. **219**, p. 1–6.

Postma, G., Kleverlaan, K., Cartigny, M.J.B., Manuscript, O., and Oceanography, N., 2014, Recognition of cyclic steps in sandy and gravelly turbidite sequences, and consequences for the Bouma facies model.: *Sedimentology*, v. **61**, p. 2268–2290.

Postma, G., Nemec, W., and Kleinspehn, K.L., 1988, Large floating clasts in turbidites: a mechanism for their emplacement.: *Sedimentary Geology*, v. **58**, p. 47–61.

Puig, P., Palanques, A., and Martín, J., 2014, Contemporary sediment-transport processes in submarine canyons.: *Annual review of marine science*, v. **6**, p. 53–77.

Pyrcz, M., Sech, R., Covault, J., Sun, T., Willis, B., and Sylvester, Z., 2014, Process-mimicking Modeling Considerations, *in* Closing the gap II: advances in applied geomodelling for hydrocarbon reservoirs, p. 1–16.

Reech, F., 1852, Cours de mécanique d'après la nature généralement flexible et élastique des corps ...: Carilian-Goeury et V Dalmont, Paris.

Rouse, H., 1936, Discharge Characteristics of the Free Overfall: Use of Crest Section as a Control Provides Easy Means of Measuring Discharge.: *Civil Engineering*, v. **6**, p. 257–260.

Sequeiros, O.E., Spinewine, B., Garcia, M.H., Beaubouef, R.T., Sun, T., Savoye, B., and Parker, G., 2009, Experiments on Wedge-Shaped Deep Sea Sedimentary

Deposits in Minibasins and/or on Channel Levees Emplaced by Turbidity Currents. Part I. Documentation of the flow.: *Journal of Sedimentary Research*, v. **79**, p. 593–607.

Shanmugam, G., 2000, Shanmugam, Ganapathy. 50 years of the turbidite paradigm (1950s—1990s): deep-water processes and facies models—a critical perspective.: *Marine and Petroleum Geology*, v. **17**, p. 285–342.

Simmons, S.M., Parsons, D.R., Best, J.L., Oberg, K.A., Czuba, J.A., and Keevil, G.M., 2017, An evaluation of the use of a multibeam echo-sounder for observations of suspended sediment.: *Applied Acoustics*, v. **126**, p. 81–90.

Simpson, J.E., 1999, Gravity currents in the Environment and the Laboratory: Wiley, New York.

Simpson, J.E., 1982, Gravity Currents in the Laboratory, Atmosphere, and Ocean.: *Annual Review of Fluid Mechanics*, v. **14**, p. 213–234.

Slootman, A., Cartigny, M.J.B., Moscariello, A., Chiaradia, M., and de Boer, P.L., 2016, Quantification of tsunami-induced flows on a Mediterranean carbonate ramp reveals catastrophic evolution.: *Earth and Planetary Science Letters*, v. **444**, p. 192–204.

Smith, I.B., Holt, J.W., Spiga, A., Howard, A.D., and Parker, G., 2013, The spiral troughs of Mars as cyclic steps.: *Journal of Geophysical Research: Planets*, v. **118**, p. 1835–1857.

Sohn, Y.K., and Hiscott, R.N., 1995, Traction-carpet stratification in turbidites; fact or fiction?; discussion and reply.: *Journal of Sedimentary Research*, v. **65**, p. 703–705.

Soulsby, R., 1997, Dynamics of marine sands: a manual for practical applications: Thomas Telford, London.

Sovilla, B., McElwaine, J.N., and Louge, M.Y., 2015, The structure of powder snow avalanches.: *Comptes Rendus Physique*, v. **16**, p. 97–104.

Spinewine, B., Sequeiros, O.E., Garcia, M.H., Beaubouef, R.T., Sun, T., Savoye, B., and Parker, G., 2009, Experiments on wedge-shaped deep sea sedimentary deposits in minibasins and/or on chennel levees emplaced by turbidty currents. Part II.: *Journal of Sedimentary Research*, v. **79**, p. 608–628.

Stow, D. a. ., and Johansson, M., 2000, Deep-water massive sands: nature, origin

and hydrocarbon implications.: *Marine and Petroleum Geology*, v. **17**, p. 145–174.

Sumner, E.J., Amy, L.A., and Talling, P.J., 2008, Deposit Structure and Processes of Sand Deposition from Decelerating Sediment Suspensions.: *Journal of Sedimentary Research*, v. **78**, p. 529–547.

Sumner, E.J., and Paull, C.K., 2014, Swept away by a turbidity current in Mendocino submarine canyon, California.: *Geophysical Research Letters*, v. **41**, p. 7611–7618.

Sun, T., and Parker, G., 2005, Transportational cyclic steps created by flow over an erodible bed. Part 2. Theory and numerical simulation.: *Journal of Hydraulic Research*, v. **43**, p. 502–514.

Symons, W.O., Sumner, E.J., Paull, C.K., Cartigny, M.J.B., Xu, J.P.P., Maier, K.L., Lorenson, T.D., and Talling, P.J., 2017, A new model for turbidity current behavior based on integration of flow monitoring and precision coring in a submarine canyon.: *Geology*, v. **45**, p. 367–370.

Symons, W.O., Sumner, E.J., Talling, P.J., Cartigny, M.J.B., and Clare, M.A., 2016, Large-scale sediment waves and scours on the modern seafloor and their implications for the prevalence of supercritical flows.: *Marine Geology*, v. **371**, p. 130–148.

Taki, K., and Parker, G., 2005, Transportational cyclic steps created by flow over an erodible.: *Journal of Hydraulic Research*, v. **43**, p. 488–501.

Talling, P.J., Allin, J., Armitage, D. a, Arnott, R.W.C., Cartigny, M.J.B., Clare, M. a, Felletti, F., Covault, J. a, Girardclos, S., Hansen, E., Hill, P.R., Hiscott, R.N., Hogg, A.J., Clarke, J.H., et al., 2015, Key Future Directions for Research on Turbidity Currents and Their Deposits.: *Journal of Sedimentary Research*, v. **85**, p. 153–169.

Talling, P.J., Masson, D.G., Sumner, E.J., and Malgesini, G., 2012, Subaqueous sediment density flows: Depositional processes and deposit types.: *Sedimentology*, v. **59**, p. 1937–2003.

Tilston, M., Arnott, R.W.C., Rennie, C.D., and Long, B., 2015, The influence of grain size on the velocity and sediment concentration profiles and depositional record of turbidity currents.: *Geology*, v. **43**, p. 839–842.

Tubau, X., Paull, C.K., Lastras, G., Caress, D.W., Canals, M., Lundsten, E., Anderson, K., Gwiazda, R., and Amblas, D., 2015, Submarine canyons of Santa Monica Bay , Southern California : Variability in morphology and sedimentary processes.: *Marine Geology*, v. **365**, p. 61–79.

Turnbull, B., and McElwaine, J.N., 2007, A Comparison of Powder Snow Avalanches at Vallée de la Sionne with Plume Theories.: *Journal of Glaciology*, v. **53**, p. 11.

Urick, R.J., 1948, The Absorption of Sound in Suspensions of Irregular Particles.: *The Journal of the Acoustical Society of America*, v. **20**, p. 283–289.

Vellinga, A.J., Cartigny, M.J.B., Eggenhuisen, J.T., and Hansen, E.W.M., 2018, Morphodynamics and depositional signature of low-aggradation cyclic steps: New insights from a depth-resolved numerical model.: *Sedimentology*, v. **65**, p. 540–560.

Vellinga, A.J., Cartigny, M.J.B., Hansen, E.W.M., Tallinga, P.J., Clare, M.A., Sumner, E.J., and Eggenhuisen, J.T., 2016, Process-based Modelling of Turbidity Currents - From Computational Fluid-dynamics to Depositional Signature, *in* Second Conference on Forward Modelling of Sedimentary Systems, Trondheim.

Ventra, D., Cartigny, M.J.B., Bijkerk, J.F., and Acikalin, S., 2015, Supercritical-flow structures on a Late Carboniferous delta front: Sedimentologic and paleoclimatic significance.: *Geology*, v. **43**, p. 731–734.

Voellmy, A., 1955a, Uber die Zerstorungkraft von Lawinen (On the desctructive forces of avalanches).: *Bauzeitung*, v. **73**, p. 212–217.

Voellmy, A., 1955b, Über die Zerstörungskraft von Lawinen.: *Schweizerische Bauzeitung*, v. **73**, p. 159–165.

Winterwerp, J.C., de Groot, M.B., Masebrgens, D.R., and Verwoert, H., 1992, Hyperconcentrated sand-water mixutre flows over erodible bed.: *Journal of Hydraulic Engineering*, v. **118**, p. 1508–1525.

Wohletz, K.H., and Sheridan, 1979, A Model of Pyroclastic Surge.: *Geological Society of America Special Paper*, v. **180**, p. 177–193.

Wong, M., and Parker, G., 2006, Reanalysis and Correction of Bed-Load Relation of Meyer-Peter and Müller Using Their Own Database.: *Journal of Hydraulic*

Engineering, v. **132**, p. 1159–1168.

Wynn, R.B., and Stow, D.A. V, 2002, Classification and characterisation of deep-water sediment waves.: *Marine Geology*, v. **192**, p. 7–22.

Xu, J.P., 2011, Measuring currents in submarine canyons: Technological and scientific progress in the past 30 years.: *Geosphere*, v. **7**, p. 868–876.

Xu, J.P., Barry, J.P., and Paull, C.K., 2012, Small-scale turbidity currents in a big submarine canyon.: *Geology*, v. **41**, p. 143–146.

Xu, J.P., Noble, M. a., and Rosenfeld, L.K., 2004, In-situ measurements of velocity structure within turbidity currents.: *Geophysical Research Letters*, v. **31**.

Xu, J.P., Sequeiros, O.E., and Noble, M.A., 2014, Sediment concentrations, flow conditions, and downstream evolution of two turbidity currents, Monterey Canyon, USA.: *Deep-Sea Research Part I: Oceanographic Research Papers*, v. **89**, p. 11–34.

Yagishita, K., and Taira, A., 1989, Grain fabric of a laboratory antidune.: *Sedimentology*, v. **36**, p. 1001–1005.

Yokokawa, M., Okuno, K., Nakamura, A., Muto, T., Miyata, Y., and Naruse, H., 2009, Aggradational cyclic steps: Sedimentary structures found in flume experiments.: *Proceedings 33rd IAHR Congress, Vancouver*, v. **81**, p. 5547–5554.

Zhong, G., Cartigny, M.J.B., Kuang, Z., and Wang, L., 2015, Cyclic steps along the South Taiwan Shoal and West Penghu submarine canyons on the northeastern continental slope of the South China Sea.: *Geological Society of America Bulletin*, v. **127**, p. 804–824.